Thank you for making me so wonderfully complex!
Your workmanship is marvelous–
and how well I know it.

— David, c. 1048 B.C.

University of Alberta

MEASURING THE DYNAMIC IMPEDANCE
OF THE HUMAN ARM

by

MATTHEW DAVID DYCK

A thesis submitted to the Faculty of Graduate Studies and Research
in partial fulfilment of the requirements for the degree of

MASTER OF SCIENCE

in

CONTROL SYSTEMS

Department of Electrical and Computer Engineering

To my parents

ABSTRACT

This thesis presents techniques to measure the human arm's mechanical impedance using a rehabilitation robot, drawing applications to telerehabilitation and patient motor function assessment.

Conventional teleoperation system stability analysis and control assumes the human operator remains passive and injects no net energy into the system. The validity of this assumption is evaluated by mathematically analyzing the passivity of empirical arm impedance models. The results show that the arm is passive when relaxed but may become active when participants rigidly hold their arm in place. This non-passive behaviour originates from the central nervous system's position control response.

A novel, cost-effective impedance measurement technique is also presented, in which an expensive commercial force sensor is replaced by a virtual sensor incorporating a model of the robot's dynamics and kinematics. The technique is validated on a mass-spring system of known impedance and applied to the human arm.

ACKNOWLEDGMENTS

CONTENTS

LIST OF TABLES

LIST OF FIGURES

ACRONYMS

ADL Activity of daily living

AMAT Arm Motor Ability Test

DOF Degree of freedom

CNS Central nervous system

CMSA Chedoke-McMaster Stroke Assessment

EOP Excess of passivity

EMG Electromyography

FAS Functional Ability Scale

FIM Functional Independence Measure

FMA Fugl-Meyer Assessment

ICC Intraclass correlation coefficient

LTI Linear time-invariant

MAS Modified Ashworth Scale

MIMO Multiple-input multiple-output

MP Motor Power

PEM Prediction Error Method

RBS Random binary sequence

RMS Root mean square

RT Robotic therapy

SISO Single-input single-output

SRIV Simplified Refined Instrumental Variable

SOP Shortage of passivity

VAF Variance accounted for

WMFT Wolf Motor Function Test

INTRODUCTION

Ageing populations are causing a growing demand for movement rehabilitation therapy following stroke, joint injury, or other health complications resulting in motor impairment. Rehabilitation robots are a promising solution to address this mounting need and enable patients' motor abilities to improve further and faster than what is achievable by conventional therapy alone. As robots can produce precise and repetitive motions to train patients' movements, numerous robotic solutions to rehabilitate the arm, wrist, fingers, and gait have been developed over the past two decades. These technologies have been shown to yield therapeutic benefits comparable to those obtained in traditional physiotherapy programs. The robots can also readily collect precise force and position data while interacting with the patient, offering a promising paradigm to supplement traditional clinical motor performance scales based on human observation with highly reproducible, objective, and quantitative measures of patient motor performance to assist clinicians in designing optimal therapy interventions.

Rehabilitation robots are useful in both therapy and motor function assessment

This thesis develops techniques to accurately measure the *mechanical impedance* of the human arm from force and movement data collected by a rehabilitation robot. Mechanical impedance is the dynamic relationship between force and motion, encompassing the familiar concepts of inertia, viscosity, and stiffness. Impedance may be calculated by using a robot to apply force or position perturbations to the arm, measuring the resulting motions and interaction forces, and fitting an impedance model to this force-position data through system identification procedures. Knowledge of the arm's impedance is important to design therapeutic human-robot interaction systems and track motor function recovery.

Mechanical impedance is the dynamic relationship between force and motion

1.1 OUTLINE

Chapter 1 provides a brief overview of the field of rehabilitation robotics. Conventional clinical motor ability assessments are contrasted against robotic assessments common in the literature. The need for accurate human arm impedance measurement is established and a summary of previous work is provided.

Rehabilitation robots can enable a therapist and patient to collaboratively perform therapy exercises over a distance through a *tele-rehabilitation* system. Conventional approaches to analyze the stability of robotic teleoperation systems assume that a human always behaves passively during his interactions with the robot, injecting no net mechanical energy into the system. Chapter 3 tests the validity of this assumption by identifying models of the human arm's endpoint impedance during a relaxed grasping task and mathematically assessing the models for passivity. Our results agree with previous findings that the *relaxed human arm is passive* and extend this conclusion to the case where a dynamic, second-order representation of arm impedance is considered in lieu of a simple static model.

Chapter 4 investigates whether the passivity assumption also holds for a rigid grasping (i.e., posture maintenance) task. The data shows that the *rigid arm can generate energy and be active*. We demonstrate how this non-passive behaviour originates from the position-control dynamics of the central nervous system (CNS) and discuss the challenges that these dynamics introduce into the arm impedance modelling problem. Finally, we outline how Llewellyn's absolute stability criterion—a teleoperation design approach that traditionally assumes human operator passivity—may be reformulated to account for a non-passive (or overly-passive) human operator.

Accurate robotic measurements of limb impedance can offer clinicians detailed insight into the neuromusculoskeletal properties of a patient's arm. Unfortunately, the high cost of the robotic systems and their associated sensors presents a financial barrier to this technique being used in the clinic. Therefore, Chapter 5 introduces a novel arm impedance measurement technique in which human-robot interaction forces are measured by a *virtual sensor* incorporating a model of the robot's kinematics and dynamics in lieu of an expensive commercial force sensor. The technique is validated on a mass-spring system of known impedance and subsequently applied to the human arm.

Finally, Chapter 6 summarizes the research findings and suggests future directions.

1.2 PUBLICATIONS

A condensed version of   Chapters 3 and 4 was published in the 2013 IEEE World Haptics Conference, Daejeon, South Korea [1]. A

second paper at the same conference featured a version of the energy integral passivity analysis in these chapters to motivate additional research beyond the scope of this thesis [2]. An adaptation of Chapter 5 was published at the 2013 IEEE International Conference on Rehabilitation Robotics, Seattle, WA, USA [3].

1.3 CONTRIBUTIONS OF THIS THESIS

This thesis makes several new contributions to the field of human arm impedance measurement and human operator passivity analysis:

1. USE OF SAVITKZY-GOLAY FILTERS IN IMPEDANCE IDENTIFICATION. Identifying a dynamic arm impedance model requires effective techniques for noise-filtering and differentiation of measured signals. To our knowledge, we are the first to use Savtizky-Golay filters for this task. These filters are noise-robust and can obtain optimal performance with minimal tuning.

2. HUMAN ARM DYNAMICS MODELLING. Chapter 4 features diagrams of the coupled human-robot dynamics during a relaxed and rigid grasping task. We consider how the position control response of the CNS influences total impedance of the human arm in a rigid grasping task, which has often been neglected in previous studies (e.g., [4] and [5]).

3. PASSIVITY ANALYSIS WITH A TWO-DIMENSIONAL DYNAMIC MODEL. Previous work in analyzing human arm passivity has modelled the arm as a static stiffness and only considered the case when the arm is relaxed [6]. We capture the arm's impedance by a dynamic second-order model and analyze passivity for both the cases when the subject relaxes his arm and when he rigidly holds it in a fixed position. We derive analytical conditions with straightforward physical interpretations that the model parameters must satisfy for passivity.

4. EMPIRICAL DEMONSTRATION OF NON-PASSIVE BEHAVIOUR. We, to our knowledge, are the first to use a mathematically rigorous passivity-based framework to empirically demonstrate that the human operator can inject energy into a teleoperation system. This demonstrates a need to develop new approaches to teleoperation system design and stability analysis that do not assume human operator passivity.

5. THE EFFECT OF TASK INSTRUCTION AND PERTURBATION SIGNAL DESIGN ON HUMAN ARM PASSIVITY. By analyzing the time history of the arm's energy absorption, we demonstrate that non-passive behaviour can be traced to the position-control dynamics of the CNS. Using this information, we discuss how the nature of the task a human executes and the perturbation signals applied to identify arm impedance can elicit passive or active behaviour.

6. DEVELOPMENT OF A VIRTUAL FORCE SENSOR. The virtual sensing technique of Chapter 5 represents, to our knowledge, the first time dynamic arm impedance identification has been performed without a physical force sensor. The virtual sensing technique presented in this chapter can readily be adapted to other fields requiring an economical approach to measuring human-robot interaction forces.

BACKGROUND AND MOTIVATION

This chapter motivates our research in arm impedance measurement by providing an overview of prior successes and challenges in the field of rehabilitation robotics. Section 2.1 introduces the distinction of assistive versus therapeutic robotics. Section 2.2 discusses the motivation for robotic therapy (RT), with an emphasis on robotic assessment of patients' motor abilities. The state of the art clinical motor function assessment scales are reviewed in Section 2.3, followed by proposed robotic assessment methodologies in Section 2.4. Robotic measurement of mechanical impedance is highlighted in Section 2.5.

2.1 CLASSIFICATION OF REHABILITATION ROBOTS

Modern robotic rehabilitation technologies can be divided into two broad categories [7]:

1. *Assistive robots* help impaired individuals perform activities of daily living (ADLs). These devices can be subclassified as *manipulation aids* such as robotic arms mounted to a wheelchair or desk to assist in reaching for objects, *mobility aids* including smart wheelchairs with navigation assistance or mobile robots to run errands around the home, and *cognitive aids* such as robots that provide visual and verbal cues to coach individuals with dementia through daily activities.

   Assistive vs. therapeutic robotics

2. While assistive robots help individuals cope with impairment, *therapeutic robotics* address the underlying cause of motor dysfunction by administering physical or cognitive therapy exercises. These devices may also be used to diagnose disorders or monitor recovery and will therefore be the primary focus of this literature review.

Rehabilitation robotics emerged from the design of robotic orthotics and prostheses, so the earliest work in the field emphasized the development of assistive robots. Researchers first began to investigate robotics as a therapy tool in the late 1980s. In 1988, Khalili and Zomlefer developed a robotic system to flex and extend the knee for movement rehabilitation [8]. Three years later, Dijkers et al.

Historical origin of therapeutic rehabilitation robotics

introduced robotic free-reaching movement therapy for the upper limb using a Universal Machine Intelligence RTX robot to position a button at various locations for patients to touch [9]. The early 1990s saw the development of several robots for upper-limb therapy, including the influential MIT-MANUS [10–12], MIME [13, 14], and ARM Guide robots [14, 15]. The 2000s brought a proliferation of rehabilitation robotic systems, including exoskeletons for gait training [16], devices to retrain ankle movement [17], and therapeutic robots for the hand and fingers [18, 19]. Robots have also found application in cognitive therapy, including robotic vehicles to conduct therapy with autistic children [20] and robotic pets designed to have a positive emotional effect on patients [21].

2.2 MOTIVATIONS FOR THERAPEUTIC ROBOTICS

The development of therapeutic robotics has been motivated by three main factors: therapy assistance, telerehabilitation, and motor function assessment.

2.2.1 *Therapy Assistance*

Incidences of stroke are rising as the population ages. Stroke is the leading cause of disability in Canada, with over 300,000 people (1% of the population) coping with impairment as a result [22]. This mounting demand for rehabilitation therapy, coupled with pressures for cost-containment in the health-care system, has lead to patients being discharged from a rehabilitation hospital prior to attaining their full motor recovery potential [23].

Therapeutic robotic technologies have therefore been developed to complement traditional physiotherapy programs for enhanced motor recovery. The precise impact of RT on motor recovery remains unclear, as large-scale randomized clinical trials comparing different rehabilitation therapies are expensive and difficult to control [7, 24]. However, it is clear that RT is at least as effective as conventional therapies for improving function in the specific movements targeted by the therapy [7, 14, 24, 25]. Furthermore, adverse side effects from RT are rare, and the introduction of robots has not met with negative reactions from patients or increased their likelihood to withdraw from therapy programs [12, 24, 26]. Researchers often note that patients enjoy the novelty of RT tasks when asked for feedback during therapy trials.

Robots help meet a growing demand for rehabilitation therapy

RT has also proven beneficial to assist in interventions that would otherwise be physically taxing on the therapist, with gait training being a prime example of a therapy that can now be readily administered by a single clinician working with a robot rather than a team of therapists executing physically-demanding tasks [7, 25]. RT can also facilitate higher therapy intensities—patients may work with a rehabilitation robot outside of the hours when therapists are available, and robots can perform many more exercise repetitions in a single therapy session than is possible by conventional human-administered therapy. This is especially significant for stroke survivors as the brain appears to be "primed" for motor relearning during the acute and subacute phases after stroke[1] [22], and failure to deliver intense therapy during this period may permanently limit recovery. Finally, robots can deliver new modes of therapy that cannot be performed without robotic assistance. In error-augmentation therapy, for instance, a patient's movement errors are amplified by a robotic force field as a means of training the CNS to correct abnormal movement patterns [27].

Robots aid conventional therapies and enable new interventions

2.2.2 *Telerehabilitation*

Telerehabilitation enables a therapist and patient to cooperatively perform rehabilitation exercises when they are separated by a distance. The simplest telerehabilitation systems incorporate motion capture and videoconferencing technologies to allow a therapist to coach a patient through rehabilitation exercises [28], but the addition of actuated robotic devices enables force feedback for customized kinaesthetic training.

Robotic telerehabilitation systems can be divided into two types [29]:

1. In *unilateral* telerehabilitation, only the patient interacts with a robot. The therapist uses a computer interface to remotely assign therapy protocols on the robot's control computer and receive data on the patient's performance. Two salient examples include the web-based JavaTherapy system developed by Reinkensmeyer et al. [30] and a hand and fingers rehabilitation system developed by Burdea et al. with the Rutgers Master force feedback glove [31].

Unilateral vs. bilateral telerehabilitation

---

1 Stroke survivors are classified into three stages: *acute* during the few hours immediately following the cerebrovascular accident, *subacute* until a few weeks after the incident, and *chronic* thereafter.

2. In *bilateral* telerehabilitation, the patient and therapist each use a robot to interact with each other through a shared virtual environment. As each user manipulates the handle of his robot, that motion is translated to an object that is commonly grasped in the virtual environment. The resulting interaction forces are calculated and fed back to each robot. In this manner, the patient and therapist can cooperatively perform a therapy task. This enables the therapist to naturally evaluate the patient's motor abilities through kinaesthetic feedback, akin to conventional hand-over-hand therapy in the clinic. Notable examples of this technology include the work of Carignan and Olsson, who used two InMotion2 rehabilitation robots to enable two individuals to cooperatively lift a plank [32]. These robots were connected via the Internet, but physically in the same location. Kim et al. [33] performed a similar collaborative lifting using a pair of PHANToM™ haptic devices linked between the USA and the UK.

Remote hand-over-hand therapy

Although robotic telerehabilitation is still in its infancy, it holds promise to substantially increase the quality of outpatient therapy programs. Telerehabilitation could allow outpatients who live in remote areas or who have limited transportation options to still receive personalized care from their therapist. Patient recovery is frequently hampered by a lack of motivation to continue therapy upon discharge from a rehabilitation hospital [34]. The opportunity to engage with a therapist (as opposed to performing a series of "homework" exercises without supervision) promises to increase patients' commitment to their therapy regimens. Finally, therapists can remotely monitor patients' progress and adapt therapy interventions as necessary to maximize motor recovery.

Telerehabilitation enhances outpatient therapy

2.2.3 *Motor Function Assessment*

A final motivation for therapeutic robotics is objective and quantitative evaluation of patients' motor function. Physical therapy is a lengthy process that is guided by clinical evaluations of a patient's motor performance. Current techniques to evaluate the severity of impairment (discussed in more detail in Section 2.3) rely on a human expert scoring a patient's function on an established ordinal ranking system. Since these assessments rely on observation, their accuracy and consistency may vary across clinicians. Furthermore, the evaluations are time-consuming to administer, can be insensitive to small but important changes in performance, and offer little

Conventional motor function assessments have several shortcomings

insight into the root causes of motor dysfunction. This creates a need for development of more sensitive methods to consistently and objectively evaluate patient recovery.

As a patient interacts with a rehabilitation robot, the device can readily collect data including positions, velocities, and forces, offering a promising paradigm to supplement traditional clinical assessments of human arm stiffness with highly sensitive, reproducible, and objective measures. Balasubramanian et al. [35] observe that robots are more sensitive to small improvements in motor performance than traditional clinical measures, and feedback on these incremental gains can increase patient motivation. Furthermore, these devices can easily track recovery over time, are amenable to providing feedback both as knowledge of results and knowledge of performance,[2] and can provide insights into mechanisms of motor function by combining movement data with electromyography (EMG) signals. Casadio et al. [36] further note that robotic assessment can provide immediate online feedback during a training session and does not suffer from the floor and ceiling effects (in which the patient's motor performance exceeds or falls short of the range distinguishable by the assessment) of clinical scales that rely on coarse rankings of motor performance. Robots are also capable of collecting substantial amounts of movement data in a shorter period of time than possible with traditional assessments [11].

Robots accurately quantify motor function with high sensitivity

As will be illustrated in subsequent chapters, the arm impedance measurement techniques developed in this thesis find application both in telerehabilitation and motor function assessment. The latter is discussed in more detail in the following two sections.

2.3 CLINICAL ASSESSMENTS OF MOTOR FUNCTION AFTER STROKE

Although robots promise to offer improved motor function assessment techniques, clinical scales relying on a trained human observer are still the only widely-accepted motor performance assessment tools. A brief introduction of several of the most common clinical measures of motor function following stroke is provided below. Where available, Pearson's or Spearman's r coefficients and intraclass correlation coefficients (ICCs) are provided as a measure of the scale's reliability. These three statistical values measure the strength of correlation or agreement between two datasets, with a

---

2 *Knowledge of results* provides feedback on how effectively a patient completed a task, such as how quickly and smoothly she retrieved an item from a shelf. In contrast, *knowledge of performance* provides feedback on the individual movements performed during the task, such as joint velocities and displacements.

value of one indicating perfect positive correlation and values near zero indicating poor correlation.

2.3.1 *Fugl-Meyer Assessment*

The Fugl-Meyer Assessment (FMA) was developed in 1975 as a tool to evaluate motor function, balance, sensation, and joint pain in hemiplegic[3] patients. Today, it remains one of the most useful and popular assessments of motor function following stroke.

The FMA prescribes a detailed series of joint movements the patient must perform, as well as reflex and sensation tests that are administered with therapist assistance. Each task is scored on a three-point system ranging from zero (minimum) to two (maximum). The FMA contains subsections devoted to the upper extremity, the lower extremity, balance, sensation, position sense, range of motion, and joint pain [37].

This assessment has demonstrated strong interrater reliability ($r = 0.86 - 0.99$) [38] and test-retest reliability (ICC $= 0.81 - 0.97$) [39] and moderate responsiveness to change in motor function [40]. Perceived shortcomings of the scale include its susceptibility to floor and ceiling effects, and its limited emphasis on fine motor control of the hand and fingers [40, 41].

2.3.2 *Chedoke-McMaster Stroke Assessment*

The Chedoke-McMaster Stroke Assessment (CMSA) was developed to assist in classifying individuals into various stages of motor recovery, to predict rehabilitation outcomes, and to measure clinically important changes in physical function [42]. The assessment consists of two portions: an *impairment inventory* that evaluates the presence and severity of common physical impairments and the *activity inventory* that assesses the client's functional ability, with emphasis on gross motor function and walking. This assessment was found to have excellent intrarater, interrater, and test-retest reliability (ICC $= 0.97 - 0.99$) [42].

2.3.3 *Motor Assessment Scale*

While the FMA and CMSA evaluate patients' abilities to perform isolated movements, the Motor Assessment Scale was developed as a

---

3 *Hemiplegia* refers to paralysis on one side of the body. The less severe diagnosis, *hemiparesis*, describes a marked weakness on one side of the body.

task-oriented scale to assess patients' abilities to perform functional tasks such as balanced sitting, transferring out of bed, walking, and hand motion [43]. It has been found to have high interrater correlation ($r = 0.95$) and test-retest correlation ($r = 0.98$) [43], but certain items on the test have proved challenging to score accurately. Research also suggests that the FMA is superior to the Motor Assessment Scale at discriminating between levels of motor recovery in early stages of recovery and among more severely disabled patients [44].

2.3.4   *Wolf Motor Function Test*

The Wolf Motor Function Test (WMFT) also evaluates functional task performance. The patient is asked to perform common tasks as quickly as possible (e.g., turning a key in a lock, picking up a paper clip, or placing their hand on a box), and scores are assigned based on completion time [45]. The test was later modified to include a qualitative six-point Functional Ability Scale (FAS) to evaluate not only how quickly the task is executed but also the quality of coordination and movement fluidity. Both the WMFT and the FAS have been shown to have high overall interrater reliability ($r = 0.97$), although the test-retest reliability for particular tasks was found to be low [46].

2.3.5   *Arm Motor Ability Test*

Not all of the assessments in the WMFT are actual functional tasks—several of them simply require the patient to reach in a certain direction or position his arm at a particular location. As a patient's ability to execute gross movements does not necessarily correlate to an ability to perform ADLs, the Arm Motor Ability Test (AMAT) was developed to exclusively measure ADL performance [47]. Subjects are asked to execute activities such as putting on a sweater, combing their hair, or using a telephone and are assigned scores for functional ability and quality of movement on six-point scales. While the AMAT has been shown to have good interrater reliability ($r = 0.97 - 0.99$) and test-retest reliability ($r = 0.93 - 0.99$) [48], it is more difficult to administer and less sensitive to change compared to the WMFT [46].

2.3.6 *Functional Independence Measure*

Of the clinical scales that assess ADL performance, the Functional Independence Measure (FIM) is one of the most popular and thoroughly researched [49]. The FIM ranks patients on a seven-point scale as they perform tasks such as eating, dressing, grooming, and navigating stairs. The test also evaluates patients' ability to transfer themselves to bed, to a chair, into a bathtub, etc., considers their sphincter control, and evaluates their communication and social cognition [41]. The FIM excels at classifying the level of care that patients require and is also used to evaluate outcomes in rehabilitation. However, it is less effective at tracking changes in an individual patient's performance over time [49] and does not assess ADL performance in community environments [41]. Some researchers assert it is susceptible to influence by a patient's personality, depression, or attitudes of dependence [12].

2.3.7 *Modified Ashworth Scale*

The Modified Ashworth Scale (MAS) is the most widely used clinical measure of muscle tone and spasticity. *Muscle tone* refers to a muscle's resistance to stretch due to a continuous partial activation of the muscle, even when it is at rest. *Hypertonia*, a common disorder in stroke survivors, is an increased resistance to passive[4] movement and may or may not be accompanied by spasticity. *Spasticity* is generally defined as a muscle disorder which causes velocity-dependent increase in the stretch reflex, but the precise nature of spasticity is debated [50], with some clinicians using the terms "tone" and "spasticity" interchangeably [51].

Tone, hypertonia, and spasticity

The MAS ranks patients on a six-point scale (Table 2.1) to quantify resistance as the joint is passively moved through its range of motion at various speeds [11]. While some consider the MAS to have moderate to good reliability for isolated muscle groups [52,53], others contend that the scale has doubtful reliability and cannot be used to assess individuals with low muscle tone, creating a need for development of more accurate means of assessing a limb's resistance to movement [11,54].

The reliability of the MAS is doubted

---

4 In a clinical context, *passive movement* of a patient's joint refers to movement that is externally-imposed rather than initiated by the patient. This is distinct from the mathematical concept of passivity defined for a teleoperation system in Chapter 3.

Table 2.1: Grading for the Modified Ashworth Scale (reproduced from [53]).

GRADE	DESCRIPTION
0	No increase in muscle tone
1	Slight increase in muscle tone, manifested by a catch and release or by minimal resistance at the end of the range of motion when the affected part(s) is moved in flexion or extension
1+	Slight increase in muscle tone, manifested by a catch, followed by minimal resistance throughout the remainder (less than half) of the range of motion
2	More marked increase in muscle tone through most of the range of motion, but affected part(s) easily moved
3	Considerable increase in muscle tone, passive movement difficult
4	Affected part(s) rigid in flexion or extension

2.4 ROBOTIC ASSESSMENT OF MOTOR FUNCTION

With the exception of the MAS, the clinical assessment scales discussed in the previous section generally demonstrate good reliability, with correlation coefficients often exceeding 0.9. As Bosecker et al. observe, clinical assessment scales are still the "gold standard" for rehabilitation assessment [7], and robotic engineers must demonstrate that quantitative robotic tests of physical performance not only match, but also exceed the performance of traditional clinical assessments to justify the additional cost outlay, training investment, and perceived safety risks.

Part of the reason why traditional scales are typically found to yield reproducible assessments is that they generally involve coarse ordinal rankings to facilitate straightforward classification of a patient's motor abilities. While there may not be a marked need for more *reliable* assessment techniques, robotics could offer increased assessment *resolution*, accurately detecting smaller improvements in performance. Furthermore, some clinical scales can take close to an hour to administer and may require a team of trained professionals, whereas robots can potentially perform assessments much more rapidly. This opens the door to conducting "online" assessments and allowing patients' therapy programs to be optimally modified based on rapid and immediate feedback of their performance.

Most clinical scales are reliable, but robotic assessment is more sensitive

There is a plethora of robotic metrics used to quantitatively assess patient motor performance in the literature. Lacking standard-

ized protocols, experimenters have developed measures uniquely suited to their particular robotic system and topic of investigation. As a result, the literature shows great variability in the complexity of motor performance metrics and in the insightfulness of the data they generate. This variability has caused some researchers to cite the need for the development of universal assessment protocols [7], while others assert that training and assessment procedures must be customized to a given task and robotic system to yield meaningful data, making the development of universal protocols impractical [36].

A wide variety of robotic assessment techniques exist

Regardless of one's perspective on the matter, there are common themes in the performance metrics used to assess performance of reaching tasks in the literature. A sample of the most popular classes of motor performance metrics is given below.

2.4.1 *Movement Smoothness*

Measurements of movement smoothness are based on the understanding that large-scale human reaching motions are composed of a series of smaller submovements that blend together to achieve the desired trajectory, speed, and accuracy. While this idea was proposed over a century ago, the velocity profiles of submovements were first quantitatively observed by Krebs et al. using the MIT-MANUS [55]. They subsequently demonstrated that as stroke patients recovered, their submovements grew larger (requiring fewer submovements to complete a given reaching task) and blended together more smoothly [56]. While the researchers found that different mathematical submovement models would give slightly different smoothness measurements for the same set of motion data, they also found that *changes* in movement smoothness as the patient progressed were robust to selection of different models.

Several methods of assessing movement smoothness exist in the literature. Krebs et al. analyzed the peaks and curvature of the velocity profile [12], and in subsequent studies mathematically fit dilated and scaled versions of a constant submovement velocity profile to the velocity data [55]. Casadio et al. [36] simply counted the number of peaks in the velocity profile of a reaching motion. Balasubramanian et al. [35] assessed the frequency composition of the motion (with less energy in the high frequencies corresponding to a smoother movement), Daly et al. [57] analyzed the correlation between the subject's velocity profile and an idealized minimum-jerk

velocity profile, while Finley et al. [58] assessed smoothness via the mean to peak speed ratio.

2.4.2 *Movement Accuracy*

The accuracy with which patients can position the robot's end effector is another common measure of motor performance. This may include measuring the patient's distance from a desired target [57] or assessing the deviation of the patient's reaching trajectory from an ideal straight-line path [36, 58–60]. The latter metric may be fundamentally flawed for large reaching motions, however, as there is evidence that healthy individuals used curved trajectories to reach for distant targets [61].

2.4.3 *Movement Velocity*

Measurement of mean and peak velocities in a reaching task is also a popular performance metric [15, 35, 58, 59] since healthy individuals generally perform reaching tasks more quickly than those with impairment. Kahn et al. [14] observed that maximum reaching velocity is a particularly useful metric as it is simple to measure, functionally relevant, and sensitive to change across a broad spectrum of impairment levels.

2.4.4 *Movement Synergy*

Movement synergy refers to coordinating the motion of multiple joints through simultaneous activation of various muscles in order to achieve smooth motor control. Movement synergy is readily assessed by means of an exoskeleton [62] or visual imaging system [60] that can record the motions of multiple joints simultaneously. Finley et al. [58] analyzed how smoothly a subject's shoulder and elbow angles were coordinated during reaching tasks by collecting hand position data with a planar robot and using a simple two-link model of the human arm to solve the inverse kinematics. Others use deviation from an ideal straight trajectory as a measure of movement synergy under the assumption that less coordinated muscle activation patterns will give rise to more circuitous trajectories [35].

2.4.5 *Amount of Robotic Assistance*

A patient's motor control can also be assessed by comparing the portion of a reaching task he can perform independently with the portion he requires assistance forces from the robot to complete. This may be done by measuring the mechanical work done by the robot [36] or by discretizing the reaching trajectory and tallying which segments were performed independently versus with robotic assistance [59].

2.4.6 *Range of Active Motion*

A simple measure of motor recovery readily measured by a robot is the patient's range of independent motion. This measure is also frequently included in conventional, non-robotic assessments of motor function. Range of motion was a key performance metric in studies with the ARM guide [15].

2.4.7 *Force Control*

While kinematic measures are most commonly used to assess motor function, some researchers have analyzed dynamic force data as well. Colombo et al. compared the directions of the normalized forces patients applied during an unconstrained reaching task with those of healthy individuals using the MEMOS robot, but found that this measure improved during rehabilitation for only half of the patients in their study [59]. Lum et al. used the MIME robot to measure the average angle between the patient's force vector and their direction of motion, with smaller angles indicating better motor control [13]. Bosecker et al. measured shoulder strength using the force sensor on a rehabilitation robot and successfully used the results to estimate the subject's score on the Motor Power (MP) scale [11].

2.5 MECHANICAL IMPEDANCE MEASUREMENT

A final important application of robotic motor peformance assessment is measuring the mechanical impedance of various joints and limbs in the human body. Robotic measurement of limb impedance was initially conceived as a means to investigate how the CNS controls movement by developing models of the human arm incorporating CNS position control components [63–65]. Other studies

focused on impedance measurement as a means of characterizing arm dynamics to design human-robot interaction systems [6, 66].

As previously mentioned, abnormal muscle tone and spasticity are common problems encountered in the rehabilitation clinic. Since both tone and spasticity describe a limb resisting movement imposed by an external force, they are directly related to the concept of mechanical impedance.

This thesis focuses on impedance measurement for the following reasons:

Motivation for impedance measurement

1. UNRELIABILITY OF THE MODIFIED ASHWORTH SCALE. Of all the clinical scales previously discussed, the reliability of the MAS for measuring muscle tone and spasticity is most heavily doubted. Robots hold promise as a means to accurately measure impedance in order to monitor the effectiveness of therapies intended to restore normal tone and reduce spasticity.

2. INSIGHTS INTO MOTOR CONTROL. Developing accurate models of the impedance of the arm can provide insight into how the CNS controls movement, laying the foundation for a better understanding of motor dysfunction.

3. APPLICATION TO TELEREHABILITATION. In a telerehabilitation system, empirical investigations into impedance of the therapist and patient's limbs can provide data useful in improving system performance.

4. STRAIGHTFORWARD ROBOTIC IMPLEMENTATION. Many clinical assessments of motor function focus on measuring ADL performance, but the development of a robot capable of simulating a sizeable variety of complex ADLs with multiple degrees of freedom (DOFs) is fraught with mechanical and economic challenges. Impedance measurement, however, can be implemented with any backdrivable robot capable of force and position sensing with minimal additional costs.

2.5.1 *Biomechanical Origins of Impedance*

On a basic level, the arm's neuromusculoskeletal structure may be compared to a robot. Biological receptors akin to joint encoders or force sensors receive data on the arm's position, velocity, and forces. They relay this data through wiring known as *afferent neurons* to the CNS, which acts as the arm's control system. The CNS processes

Comparing the arm's structure to a robot

this data and issues motor commands via *efferent neuron* wiring to the muscles, which serve as the arm's actuators. The muscles apply torques to the joints of the skeletal system, causing the arm to follow the control signal from the CNS.

The arm's mechanical impedance arises from two sources:

Two sources of arm impedance

1. INTRINSIC PHYSICAL PROPERTIES. This refers to the stiffness, viscosity, and inertia inherent to the arm's tissues and skeletal structure.

2. INVOLUNTARY REFLEX RESPONSES. A *reflex* is an immediate and involuntary motor response to a specific stimulus. In the *stretch reflex* for instance, when the CNS detects that a relaxed muscle has been suddenly stretched (e.g., by a robot applying a perturbation force to the arm), it causes the muscle to contract and oppose the applied stretch. This process occurs automatically, without any cognitive intervention from the human. See [67] for examples of additional reflex types.

The CNS is also responsible for impedance modulation, which is essential to maintaining posture, achieving stability, and rejecting disturbances as humans interact with their environment [68]. Humans are able to vary their mechanical impedance by two primary mechanisms [69,70]:

Two mechanisms for impedance modulation

1. ARM CONFIGURATION. Impedance depends on skeletal geometry. For example, the arm has high impedance along the forearm's axis when the elbow is rigidly extended, and this value decreases as the elbow is flexed. The total impedance the arm presents at its endpoint may therefore be modulated by adjusting the configuration of the arm.

2. MUSCULAR COCONTRACTION. Since muscles can only pull and not push on a joint, they operate in *agonist* and *antagonist* pairs (Fig. 2.1). Contraction of the agonist muscles causes the joint to rotate in one direction whereas contraction of the antagonist muscles causes rotation in the opposition direction. If both groups are *cocontracted* simultaneously, they will tend to stabilize the joint and increase the overall limb impedance.

The complexity of the musculoskeletal system makes modelling the human arm for impedance measurement a particularly challenging task. As represented in Fig. 2.1, the arm contains both monoarticular muscles which act on a single joint and biarticular muscles that span multiple joints. Biarticular muscles couple

The human arm presents modelling challenges
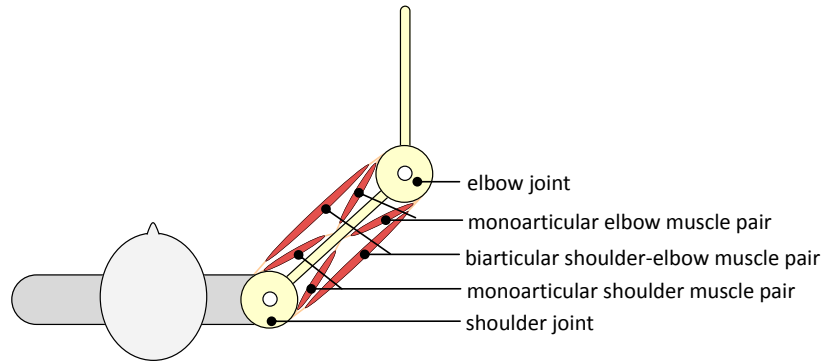
Figure 2.1: Schematic of biarticular vs. monoarticular arm muscles adapted from [66]. The muscles appear in agonist-antagonist pairs.

the motions of various joints together, making it challenging to isolate impedance contributions from individual joints or muscle groups [68]. While it is common to model joints as independent hinges, this is a stark oversimplification [71]—the shoulder, for instance, is a complex of multiple joints with several degrees of freedom. Furthermore, since impedance varies with position and muscle contraction level, it is challenging to measure in a repeatable manner. In addition, the mechanical complexities of the human hand and arm can cause the response to an applied perturbation to include force components that are not directly opposed to the applied displacement, requiring the use of matrices rather than scalars to fully describe impedance.

2.5.2 *Measurement Approaches*

Mechanical impedance is typically measured via system identification methods in which experimenters apply position or force perturbations to the joint or limb under investigation and observe the resulting force and motion response. Subjects are typically asked to completely relax their muscles or exert a constant force while the measurement is performed. A variety of approaches are taken to prevent the subjects from voluntarily varying their impedance during the measurement procedure, including simply instructing the subject to relax [72], surprising the subject by applying the perturbation at an unexpected time [73], performing very short measurements during which the subject has no time to voluntarily modulate their impedance [74], or applying a series of perturbations with randomly-oriented directions [68,75].

Arm impedance should not vary during measurement

The pioneering work in robotic impedance measurement for the upper limb was performed by Mussa-Ivaldi et al. [63], who used a planar robot to impose step position perturbations on a human subject's hand, allowing the static endpoint impedance (i.e., stiffness) of the arm to be calculated in two Cartesian dimensions. McIntyre et al. [76] adapted this technique to measure changes in stiffness in response to external loading forces. Gomi et al. [64], Dolan et al. [66], and Tsuji et al. [77] extended the approach to identify a second-order impedance model encapsulating not only the arm's stiffness, but also the dynamic impedance components of inertia and viscosity. Burdet et al. [73] measured the stiffness of the arm in the presence of unstable force fields and found that the CNS stabilizes planar reaching motions by optimizing impedance. Bennet et al. [78] applied position perturbations to the elbow joint to measure its stiffness in the joint domain, and Lacquanti et al. [79] applied pseudorandom torque to measure elbow and wrist stiffness during a catching task.

The use of second-order impedance models is still common in the literature. For instance, Kuchenbecker et al. [80] modelled the human wrist as a mass-spring-damper system and found that while grip force and wrist impedance are correlated with each other, the relationship was unique for each test subject. Hajian and Howe [74] used a second-order model to investigate the impedance of the human finger. However, higher-order models have also been investigated in an attempt to achieve a more comprehensive representation of the human arm [81].

Second-order models are common in the literature

While this gray-box identification approach offers the appealing simplicity of mapping parameters of the human arm to a simple and well-understood mechanical model, this simplification comes at the cost of modelling accuracy. Summarizing the results of several studies, Perreault et al. [71] concede that second-order modeling approaches may be "reasonably accurate" for fixed postures and small perturbations, but they are unlikely to hold in more complex situations. For example, stiffness measurements have been found to vary with the amplitude of the applied perturbation, and nonlinear stiffness components have been observed when stretch reflexes are excited by the applied perturbations.

This has prompted several researchers to employ stochastic position or force perturbations to identify non-parametric models of arm impedance or admittance [68, 75]. These system identification approaches make no assumptions of model structure other than that the system responds linearly for small perturbations. Others have extended these techniques to analyze impedance in three di-

Non-parametric models have higher versatility

mensions [82,83]. Detailed models of the arm's neuromusculoskeletal structure have been identified to distinguish impedance contributions of the arm's intrinsic biomechanics from those caused by its involuntary reflex responses [4].

Customized mechatronic systems for arm impedance measurement have also been designed to deliver high-bandwidth perturbations in multiple measurement planes [68] and enable rapid online data collection by applying perturbations using a rotating cam mechanism [18].

Although impedance measurement has numerous technical challenges, the development of accurate measurement techniques can establish more effective patient monitoring and intervention assessment, enable insightful investigation of human motor control, and open the door to new rehabilitation robotic technologies. These applications will be explored in the following chapters.

3

RELAXED ARM IMPEDANCE MEASUREMENT AND PASSIVITY ANALYSIS

3.1 INTRODUCTION

Stability is the most crucial performance characteristic of a tele-rehabilitation system. The therapist's and patient's robots must never make sporadic movements or exert erroneous forces that could cause injury or compromise therapy effectiveness. Conventional approaches to analyzing the stability of a bilateral teleoperation system assume that the human operator does not inject energy into the system and behaves in a passive manner. Does this assumption hold for various tasks a therapist or patient may execute?

Conventional teleoperation system control and stability analysis assumes human operator passivity

To answer this question, this chapter presents identified models of the human arm's endpoint impedance during a relaxed grasping task. These models are assessed for passivity over the frequency range characteristic of human motion. Section 3.2 introduces the conventional human operator passivity assumption and explains why it should be questioned. Section 3.3 mathematically formalizes the concept of passivity and introduces the arm modelling approach. Section 3.4 describes the design of the arm impedance identification experiments and Section 3.5 presents the data analysis. The results, which appear in Section 3.6, confirm that the *relaxed* human arm behaves as a passive system. The implications of these results are discussed in Section 3.7, followed by concluding remarks in Section 3.8. The subsequent chapter investigates whether the passivity assumption is also valid for a *rigid grasping* (posture maintenance) task.

Combined versions of this chapter and the following chapter have been published: M. Dyck, A. Jazayeri, and M. Tavakoli, "Is the human operator in a teleoperation system passive?" in *IEEE World Haptics Conference*, Daejeon, Korea, 2013, pp. 683–688.
Another publication featured a version of the energy integral passivity analysis included in these two chapters to motivate teleoperation research beyond the scope of this thesis: A. Jazayeri, M. Dyck, and M. Tavakoli, "Stability analysis of teleoperation systems under strictly passive and non-passive operator," in *IEEE World Haptics Conference*, Daejeon, Korea, 2013, pp. 695–700.

3.2 BACKGROUND AND MOTIVATION

A teleoperation system consists of a human operator, a remote environment, and a *teleoperator* comprising the master and slave robots, their controllers, and a communication channel (Fig. 3.1). In bilateral teleoperation, the slave robot mimics the motions of the master robot held by the human operator, and the human operator receives haptic feedback of the contact forces between the slave and environment. In robotic telerehabilitation, the therapist (the human operator) uses a robotic interface (the master device) to control a home-based therapeutic robot (the slave device) in contact with the patient's impaired limb (the environment).

Structure of a teleoperation system

Teleoperation system

| Human operator: Therapist | ⇔ | Master robot: Therapist's device | ⇔ | Communication channel and robot control | ⇔ | Slave robot: Patient's device | ⇔ | Environment: Patient's impaired limb |
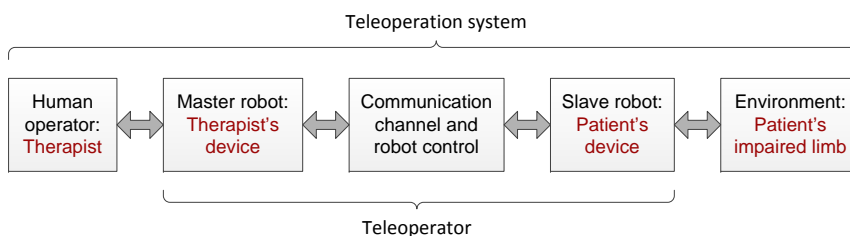
Teleoperator

Figure 3.1: Schematic of a teleoperation system in the context of telerehabilitation.

The stability of a bilateral teleoperation system may be investigated by applying the passivity (Raisbeck's or scattering-based) criterion or the absolute stability (Llewellyn's) criterion to the teleoperator [84, 85]. In both frameworks, *passivity of the teleoperator's terminations, i.e., the human operator and the environment, is assumed*. This is a convenient assumption that makes it possible to perform stability analysis of a teleoperation system without knowledge of the typically uncertain, time-varying and/or unknown dynamics of two of its subsystems—the human operator and environment.

The passivity assumption simplifies stability analysis

While it may be reasonable to assert that most physical environments do not contribute energy to the teleoperation system, is the same true for the human operator who deliberately manipulates the master robot? The human operator passivity assumption is conventionally justified by a paper published by Hogan [6]. The paper is based on the work of Mussa-Ivaldi et al. [63], who used a planar robot to impose step position perturbations on human subjects' hands and measure the resulting restoring forces. They used this data to calculate the static stiffness of the arm in two Cartesian dimensions. Subjects were instructed to relax their arm and avoid voluntarily intervening as the robot perturbed their hand. In his paper, Hogan extended this analysis by separating the measured

Hogan's analysis of arm stiffness has been used to justify the passivity assumption

stiffness into an active and a passive component. He found that the active component was negligibly small in comparison to the passive component, demonstrating that the relaxed human arm behaves as a passive system. While Hogan's finding has profoundly impacted teleoperation system stability analysis, several important questions remain unanswered:

- Hogan demonstrated that the human arm's *static* stiffness is indeed passive, but is passivity still maintained when a *dynamic* impedance model including inertia and viscosity is used for a more complete characterization of arm impedance?

- Is passivity maintained if the arm is not relaxed, but executes a motor control task instead?

- How does the experimental protocol used to identify the arm impedance influence the passivity analysis? Can different robot-applied perturbation signals elicit passive or non-passive behaviour from the human arm?

- Can we quantitatively measure how passive or active a human operator is and take advantage of this information to improve teleoperation system performance?

These questions will be the focus of both this chapter and the one to follow.

3.3 MATHEMATICAL PRELIMINARIES

3.3.1 *Passivity and Stability Analysis*

The concept of passivity of a system is formally defined below.

DEFINITION 3.1: *Consider the following inequality for a system with input signal $U(t) \doteq [u_1(t)\, u_2(t) \ldots u_n(t)]^T$ and output signal $Y(t) \doteq [y_1(t)\, y_2(t) \ldots y_n(t)]^T$:*

Mathematical definition of passivity

$$\int_0^t Y(\tau) \cdot U(\tau) d\tau \geq \beta + \delta \int_0^t U(\tau) \cdot U(\tau) d\tau, \tag{3.1}$$

1. *If there exists a constant β such that this inequality holds for all $t \geq 0$ with $\delta = 0$, the system is said to be* passive. *The constant β accounts for the system's initial energy at $t = 0$.*

2. *Furthermore, if the inequality holds for all $t \geq 0$ with a constant $\delta > 0$, the system is* input strictly passive *with excess of passivity (EOP) equal to δ [86].*

3. *If the inequality holds for all $t \geq 0$ with a constant $\delta < 0$, the system is* input non-passive[1] *with shortage of passivity (SOP) equal to $\lambda = -\delta$.*

The transfer matrix of any passive multiple-input multiple-output (MIMO) linear time-invariant (LTI) system is positive real as defined below.

DEFINITION 3.2: *[87, 88] An $n \times n$ rational transfer function matrix* $\mathbf{Z}(s)$ *is positive real if:*

Passivity of a transfer matrix

1. *all finite poles of all elements of $\mathbf{Z}(s)$ are in $\mathrm{Re}\{s\} \leq 0$,*

2. *any pure imaginary pole $j\omega_0$ of any element of $\mathbf{Z}(s)$ is a simple pole, and the residue matrix $\lim_{s \to j\omega_0}(s - j\omega_0)\mathbf{Z}(s)$ in the case that ω_0 is finite, and $\lim_{\omega \to \infty} B(j\omega)/j\omega$ in the case that ω_0 is infinite,[2] is positive semidefinite Hermitian, and*

3. *for all real positive frequencies ω for which $j\omega$ is not a pole of any element of $\mathbf{Z}(s)$, the matrix $\mathbf{H}(j\omega) \doteq \mathbf{Z}(j\omega) + \mathbf{Z}^T(-j\omega)$ is positive semidefinite.*

The concepts of EOP and SOP may also be related to a system's transfer matrix through the following theorem.

THEOREM 3.1: *[90] Consider a MIMO system with an $n \times n$ transfer matrix $\mathbf{Z}(s)$, where the poles of all elements have negative real parts. The system is input strictly passive with EOP of $\delta > 0$ if and only if $\mathbf{H}(j\omega) = \mathbf{Z}^T(-j\omega) + \mathbf{Z}(j\omega) \geq 2\delta\mathbf{I}$, where $\mathbf{I}$ is the identity matrix. Similarly, for an input non-passive system with SOP of $\lambda > 0$, $\mathbf{H}(j\omega) \geq -2\lambda\mathbf{I}$.*

EOP or SOP of a transfer matrix

Definitions 3.1 and 3.2 suggest two ways of assessing the arm's passivity:

INTEGRAL APPROACH   The first directly calculates the energy absorbed by the arm according to (3.1). For the human arm modelled as an impedance in a teleoperation system, the input and output signals are velocity and force, respectively. Therefore, the integral $\int_0^t F_h(\tau) \cdot \dot{X}(\tau)\, d\tau$ is numerically evaluated for the duration of a trial. Assuming $\beta = 0$, if this integral increases over time, energy is being absorbed by the arm indicating passive behaviour. If the integral decreases, the arm is generating energy and being active.

---

1 The term "input non-passive" will be shortened to "non-passive" or "active" in subsequent use.

2 Any improper element of $Z(s)$ is said to have at least one pole at the point at infinity and must satisfy this condition [89]. Unlike finite-valued complex poles, poles at the point at infinity need not occur in complex conjugate pairs.

While this approach provides clear insight into passivity or activity *for a specific set of force and velocity signals*, it cannot be used to draw incontrovertible conclusions about the arm's passivity. To rigorously prove that the arm is passive with this approach, one would need to evaluate the energy absorption integral for all possible input and output signals over all time.

IMPEDANCE MODEL APPROACH   The second approach uses Definition 3.2 to mathematically examine the passivity of an identified transfer matrix model of the arm's impedance. This allows the passivity analysis to be generalized to arbitrary inputs and outputs, but requires a model to be identified accurately.

3.3.2 *Arm Impedance Modelling*

The human arm's endpoint impedance may be represented in a Cartesian plane by the following model:

Cartesian model of human arm impedance

$$\mathbf{M}\ddot{X}(t) + \mathbf{B}\dot{X}(t) + \mathbf{K}\left(X(t) - X_0\right) = -F_h(t), \tag{3.2}$$

where $X(t) = [x(t)\ y(t)]^T$ is the hand position, $X_0 = [x_0\ y_0]^T$ is the hand's equilibrium position commanded by the CNS, and $F_h = [f_x(t)\ f_y(t)]^T$ is the force the hand exerts on the robot. These position and force vectors are measured in a Cartesian coordinate frame originating at the subject's shoulder, as shown in Fig. 3.3. The matrices

$$\mathbf{M} \doteq \begin{bmatrix} m_{xx} & m_{xy} \\ m_{yx} & m_{yy} \end{bmatrix}, \ \mathbf{B} \doteq \begin{bmatrix} b_{xx} & b_{xy} \\ b_{yx} & b_{yy} \end{bmatrix}, \ \text{and } \mathbf{K} \doteq \begin{bmatrix} k_{xx} & k_{xy} \\ k_{yx} & k_{yy} \end{bmatrix}, \tag{3.3}$$

which represent the hand inertia, damping, and stiffness, respectively, contain real-valued constants for the Cartesian plane of measurement. This planar model is sufficient to capture the relative contributions of the shoulder, elbow, and biarticular muscles to the overall limb impedance without necessitating the experimental complexity of a full three-dimensional measurement [91].

Equation 3.2 is derived from a simplified representation of the arm's neuromusculoskeletal structure as Dolan et al. detail in [66], but it may also be interpreted as a second-order Taylor-series linearization of an arbitrary nonlinear impedance model. Therefore, the model can accurately describe the lumped effects of impedance contributions from the arm's intrinsic physical properties and in-

voluntary reflex responses only for small perturbations about the constant equilibrium position X_0.

This second-order model was selected for three reasons. First, it has been previously shown to successfully capture the endpoint impedance of the relaxed arm (e.g., [66] and [77]). Second, this model is particularly amenable to assessing passivity as the parameters afford direct physical interpretation. Finally, it encompasses the stiffness model in Hogan's influential paper on human operator passivity, which may be obtained by setting the **M** and **B** matrices to zero [6].

For passivity analysis, the relation between the power-conjugate variables of force and velocity is required. Taking the Laplace transform of (3.2) and defining $F_h(s) \doteq \mathcal{L}\{F_h(t)\}$ and $V(s) \doteq \mathcal{L}\{\frac{d}{dt}(X(t) - X_0)\} = \mathcal{L}\{\frac{d}{dt}X(t)\}$ allow the impedance to be represented by a transfer matrix:

Transfer matrix model of human arm impedance

$$\mathbf{Z}(s) = \begin{bmatrix} \dfrac{m_{xx}s^2 + b_{xx}s + k_{xx}}{s} & \dfrac{m_{xy}s^2 + b_{xy}s + k_{xy}}{s} \\[2ex] \dfrac{m_{yx}s^2 + b_{yx}s + k_{yx}}{s} & \dfrac{m_{yy}s^2 + b_{yy}s + k_{yy}}{s} \end{bmatrix}, \qquad (3.4)$$

with $F_h(s) = \mathbf{Z}(s)V(s)$.

3.4 EXPERIMENTAL PROTOCOLS

3.4.1 *Experiment Setup*

Human arm impedance measurements were performed with a 2-DOF planar rehabilitation robot (Fig. 3.2) manufactured by Quanser, Inc. (Markham, Ontario, Canada). The robot's capstan drive mechanism makes it readily back-drivable with low friction and inertia. At its end-effector, the robot can exert forces in excess of 50 N throughout its semicircular workspace, and the motors' optical encoders provide a Cartesian resolution of better than 0.002 mm in position measurement. Position control was provided by a joint-domain proportional-derivative controller. Details of the robot's kinematics and dynamics are provided in Appendix A. A 6-DOF force/torque sensor (Gamma Net, ATI Industrial Automation, Apex, NC, USA) connected to the distal link measured human-robot interaction forces. All data logging and robot control actions occurred with a 1 kHz sampling frequency.

Robot specifications
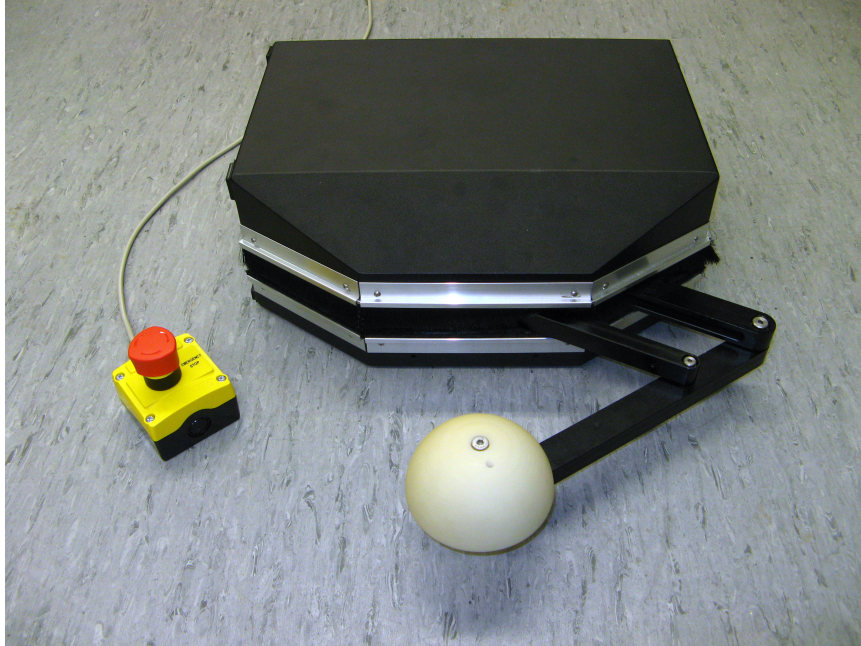
Figure 3.2: The upper-limb planar rehabilitation robot used in the experiments. The system's emergency stop button is shown at the left.

3.4.2 *Data Collection*

For arm impedance identification, data was collected from six participants[3] with no history of motor impairment, one of whom was left-handed and one of whom was female. Participants ranged in age from 23 to 38 years, with an average age of 28.2 years. All subjects provided informed consent to the experimental procedures, which were reviewed and approved by the University of Alberta Research Ethics Board (Study ID: Pro00033955). A copy of the Consent Form is included in Appendix B.

In each trial, the participant sat in front of the robot with his or her right forearm strapped to a support (Fig. 3.3). The participant's elbow was supported against gravity by a sling attached to a 2 m rope connected to the ceiling. All data was collected at a shoulder-height *test location* ($x = 0$ cm, $y = 52$ cm) in the coordinate frame aligned at the participant's shoulder joint. A belt restrained the participant's torso to prevent translation of the upper body, which

---

3 As will be discussed in more detail in Section 4.4, participants' activity or passivity depends on the task they perform. However, for a given task, *every* participant was found to show the same characteristics of passive or active behaviour. A sample size of six subjects was therefore sufficient to capture the salient characteristics of human operator passivity or activity in our experiments.
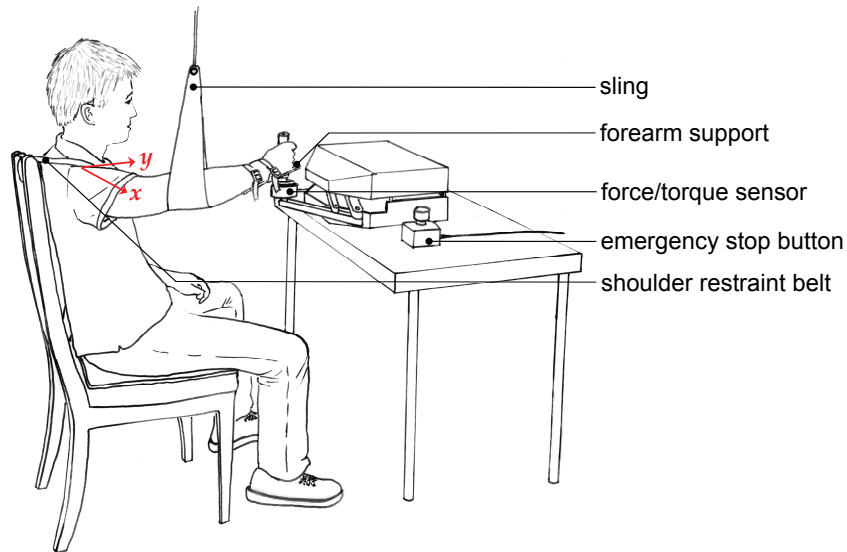
Figure 3.3: Experimental apparatus for impedance measurements on the relaxed arm. The origin of the Cartesian coordinate frame is shown at the subject's shoulder.

would have undermined the accuracy of the arm position measurements.

Each participant was instructed to relax his or her arm while the robot applied position perturbations to the hand, just as a human operator in a teleoperation system might relax his arm to enhance perception of force feedback from the environment. Position perturbations were used in lieu of force perturbations to ensure that the participant's hand did not drift away from the test location while data was collected, keeping X_0 in Equation 3.2 constant. The participants were instructed to rest their hand on the forearm support without voluntarily squeezing the robot's handle, since gripping can amplify the arm's impedance [64]. The following two types of perturbation signals were applied.

SINUSOIDAL PERTURBATIONS   Each of the robot's joints was set to track a reference position comprising the sum of ten sinusoids with frequencies from 0 to 3 Hz. This bandwidth was selected to avoid triggering instabilities in the robot's position controller or exciting resonances in the mass-spring system used to validate the impedance identification technique. Each joint moved through an angular range of $4°$, causing the robot's end-effector to remain

within a circular region 2 cm in diameter. Each trial was 50 s in duration.

UNDERDAMPED PERTURBATIONS   Inspired by the work of Dolan et al. [66], the robot applied step-like, rapidly-rising, underdamped position perturbations to the subject's hand. As in Dolan's work, these perturbations were generated by passing a 5 mm position step signal through the underdamped system

$$G(s) = \frac{\omega_n^2}{s^2 + 2\zeta\omega_n s + \omega_n^2} \tag{3.5}$$

with a damping ratio $\zeta = 0.1$ and natural frequency $\omega_n = 15 \text{ s}^{-1}$. Hand displacements of up to 11 mm were observed during the transient portion of the motion. Two perturbations were applied in each of 8 directions spaced evenly at 45° intervals around a circle, for a total of 16 perturbations per trial.[4] To reduce any subconscious intervention on the part of the participant, the 16 perturbations were applied in random order. For the same reason, each perturbation's duration (1.5–2.0 s) and onset time (2.0–7.0 s after the previous perturbation) were selected randomly. Following each perturbation, the robot's position controller gently moved the participant's hand back to the test location such that each subsequent perturbation was delivered from the same initial position.

A total of four sinusoidal perturbation trials were performed for each of the six participants. An additional four underdamped perturbation trials were collected from two participants. Segments of typical data are shown in Fig. 3.4.

3.5 ANALYSIS

3.5.1 *Data Preprocessing*

Identifying the arm impedance model of (3.2) requires accurate records of $\dot{X}(t)$ and $\ddot{X}(t)$. Finite-differencing and low-pass filtering of position data was found to be insufficiently noise-robust for this task, as the low-pass filter's cutoff frequency needed to be individually tuned for each dataset to obtain reasonable results. Therefore, the state-variable filter differentiation approach employed in

Finite-differencing and state-variable filtering failed to yield accurate derivatives

---

4 Additional experiments were performed with two underdamped perturbations evenly spaced in 16 directions about a circle, for a total of 32 perturbations per trial. However, doubling the number of perturbation directions was not found to change the identified impedance values.
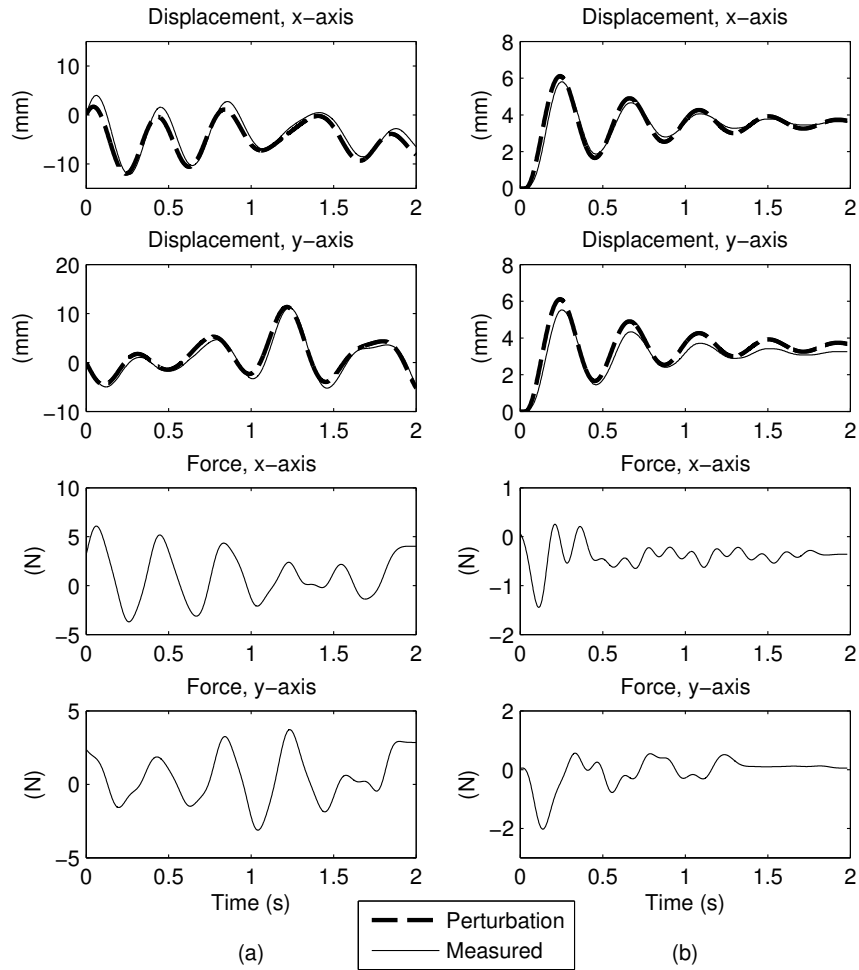
Figure 3.4: Typical force and position signals for the relaxed arm with (a) sinusoidal perturbations and (b) underdamped perturbations. The force sensor measures the force exerted *by the human on the robot*. Dashed lines indicate the position perturbation signals input to the robot's controller. Signals have been low-pass filtered for noise suppression.

the arm impedance identification experiments of Dolan et al. [66] was implemented. In this technique, an ideal differentiator is cascaded with a second-order transfer function whose parameters are selected to mirror the frequency-domain properties of the position data. Unfortunately, the identified impedance values were found to be very sensitive to the selection of these transfer function parameters, and the approach affords no straightforward means of identifying an "optimal" parameter set.

We developed a more robust differentiation approach that used a Savitzky-Golay filter [92] to remove noise from all measured signals and calculate their derivatives. To the best of our knowledge, this is the first time these filters have been employed in the context of human arm impedance identification. This non-causal filtering technique fits a smooth N^{th}-order polynomial to a window of W consecutive data points. By ensuring $W \gg N$, the least-squares fitting process smooths out any random fluctuations in the unfiltered signal. The polynomial is evaluated and differentiated at the center of the window to yield both the smoothed signal and its time derivatives at the corresponding time instant. The window is subsequently advanced forward by one sampling interval, and the algorithm is repeated until the entire signal has been processed by the filter. The filter's normalized 3 dB cutoff frequency can be estimated from the formula [93]

Derivatives were calculated with a Savitzky-Golay filter

$$f_c = \frac{\omega_c}{\pi} \cong \frac{N+1}{1.6W - 4.6} \text{ where } W \geq 51 \text{ and } N < \frac{W-1}{2}. \quad (3.6)$$

Through empirical evaluation, a filter with $N = 6$ and $W = 101$ was found to yield optimal results.

To enhance the noise-suppression characteristics of the Savitzky-Golay filter, its three outputs (i.e., the smoothed signal and its first and second derivatives) were passed through a zero-phase 5th-order Butterworth low-pass filter (MATLAB function `filtfilt`). The cutoff frequency was set at 5 Hz as the data collected in this study was found to have negligible content at higher frequencies. Fig. 3.5 shows the magnitude response of combined Savitzky-Golay smoothing and Butterworth low-pass filtering operations (herein referred to as the *"smoothing filter"*) and the combined Savitzky-Golay first and second derivative and Butterworth low-pass filtering operations (termed the *"first derivative filter"* and *"second derivative filter"*). The smoothing filter maintains a magnitude response near unity over the 5 Hz bandwidth of the movement data, but drops to zero at higher frequencies for noise suppression. Similarly, the dif-

A Butterworth low-pass filter was added for enhanced noise suppression

ferentiation filters closely match the ideal differentiator responses at low frequencies but decay to zero at higher frequencies.
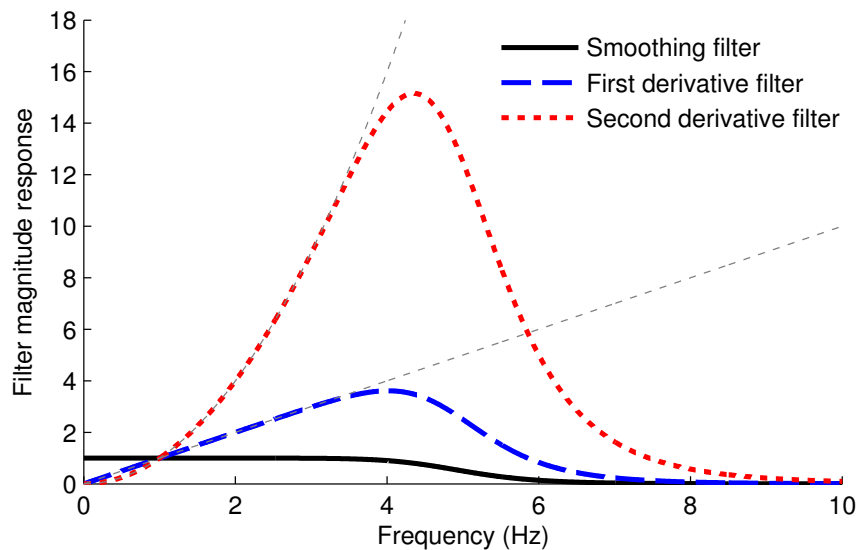
Figure 3.5: Combined frequency response magnitude for the smoothing filter and differentiation filters, each formed by a combination of Savitzky-Golay filtering and zero-phase Butterworth low-pass filtering. The ideal differentiator responses are depicted by thin dashed lines.

Fig. 3.6 validates these filters for a 10 s segment of x-axis position data. This Cartesian position signal is calculated from joint encoder data using the robot's forward kinematics. The top plot shows the position signal and the double-integrated (MATLAB function `cumtrapz`) acceleration from the second-derivative filter. The two signals agree exceptionally well. The middle plot demonstrates that the velocity signal from the first derivative filter likewise agrees with the integrated acceleration from the second-derivative filter. Finally, the bottom plot indicates that the acceleration signal from the second-derivative filter agrees with the acceleration measured by an accelerometer (ADXL-203, Analog Devices, Norwood, MA, USA).

The Savtikzy-Golay filter calculates derivatives with excellent accuracy.

3.5.2 *Impedance Identification*

The matrices **M**, **B**, and **K** and equilibrium position X_0 were identified by linear least-squares regression. Prior to identification, the force signal $F_h(t)$ and position signal $X(t)$ were passed through the smoothing filter for noise suppression. The velocity $\dot{X}(t)$ and ac-
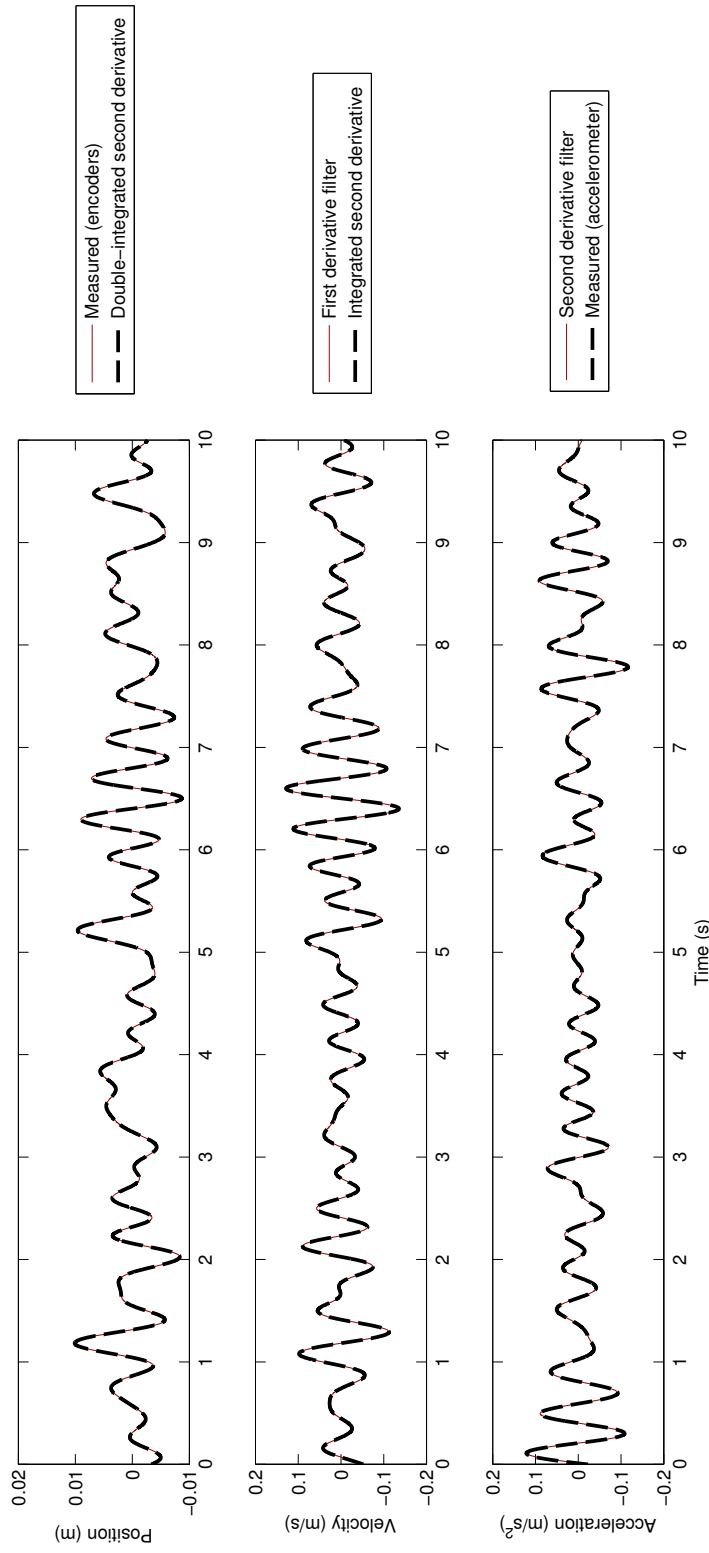
Figure 3.6: Validation of differentiation filters. *Top:* The robot's measured position agrees with the double-integrated acceleration from the second-derivative filter. *Middle:* The velocity from the first derivative filter agrees with the integrated acceleration from the second derivative filter. *Bottom:* The acceleration from the second derivative filter agrees with accelerometer measurements.

celeration $\ddot{X}(t)$ were obtained from the first and second derivative filters.

Inertial impedance contributions arose from both the inertia of the human arm and the inertia of the wrist support with mass $\Lambda = 194$ g. To remove the effects of the wrist support from the identified impedance, impedance was identified by applying the least-squares procedure to

The mass of the wrist support was removed from the identified inertia

$$(\mathbf{M} + \Lambda\mathbf{I})\,\ddot{X}(t) + \mathbf{B}\dot{X}(t) + \mathbf{K}(X(t) - X_0) = -F_h(t), \qquad (3.7)$$

where $\mathbf{I}$ is the 2×2 identity matrix.

Appendix C provides MATLAB code to preprocess the raw data and identify model parameters.

3.5.3 *Validation of Identification Technique*

The data collection and impedance measurement techniques were validated against the mechanical mass-spring system described in Appendix D. The robot's end-effector was connected to an inertial payload and a planar array of linear mechanical springs (Fig. 3.7). Since this system did not include mechanical dampers, the impedance model of (3.2) reduces to

The identification technique was validated against a mass-spring system of known impedance

$$\mathbf{M}\ddot{X}(t) + \mathbf{K}\,(X(t) - X_0) = -F_h(t), \qquad (3.8)$$

where X_0 is the equilibrium position of the spring configuration and $\mathbf{M}$ and $\mathbf{K}$ have the simplified structure

$$\mathbf{M} \doteq \begin{bmatrix} m & 0 \\ 0 & m \end{bmatrix}, \quad \mathbf{K} \doteq \begin{bmatrix} k_{xx} & k_s \\ k_s & k_{yy} \end{bmatrix}. \qquad (3.9)$$

Note that the inertia matrix is diagonal with equal elements and the stiffness matrix is symmetric.

The robot applied underdamped[5] position perturbations (5 mm steady-state amplitude) to the mass-spring system with six different impedance configurations. Although a two-dimensional spring array has a nonlinear stiffness field, the stiffness could be approximated by (3.8) – (3.9) for small perturbations. Table 3.1 lists the theoretical stiffness (comprising k_{xx}, k_{yy}, k_s, and X_0 values calculated from independent measurements of the spring constants as

---

5 Sinusoidal perturbations estimated the mass-spring system impedance with similar accuracy—these result are discussed in detail in Chapter 5.
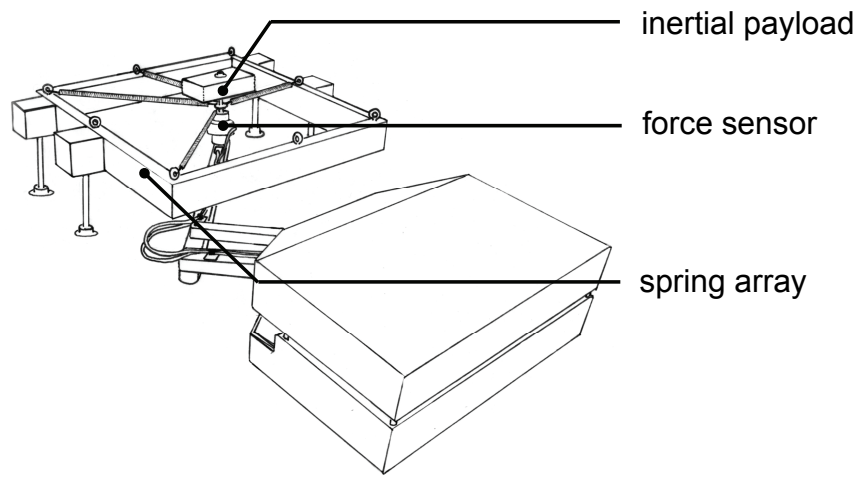
Figure 3.7: Measuring the impedance of a spring array and an inertial payload that simulate the human arm.

Table 3.1: Theoretical impedance values for the mass-spring system.

IMPEDANCE CONFIG.	STIFFNESS VALUES (N/m)			X_0 (mm)		INERTIA VALUE (kg)
	k_{xx}	k_{yy}	k_s	x_0	y_0	m
1	443.86	232.34	16.74	393	-55	0.293
2	427.08	273.83	37.87	407	35	0.539
3	310.43	306.69	-101.75	448	61	0.786
4	402.95	262.68	-69.14	418	-53	1.031
5	260.70	404.66	-73.49	343	29	1.279
6	233.32	464.70	-17.40	420	-8	1.527

discussed in Appendix D) and inertia (comprising m values measured by weighing the payloads) for each of the six configurations.

The identified X_0 values were always within 21 mm of the theoretical equilibrium positions. Fig. 3.8 demonstrates that the technique estimated the stiffness and inertia matrix elements with good accuracy. The fact that k_{yy} and m were always slightly overestimated indicates the presence of some systematic error, but this is anticipated due to unmodelled system dynamics such as friction and approximations inherent in calculating the theoretical stiffness value from empirically-determined spring constants.[6] Nevertheless, the identification technique generally captures the impedance of the mass-spring system well.
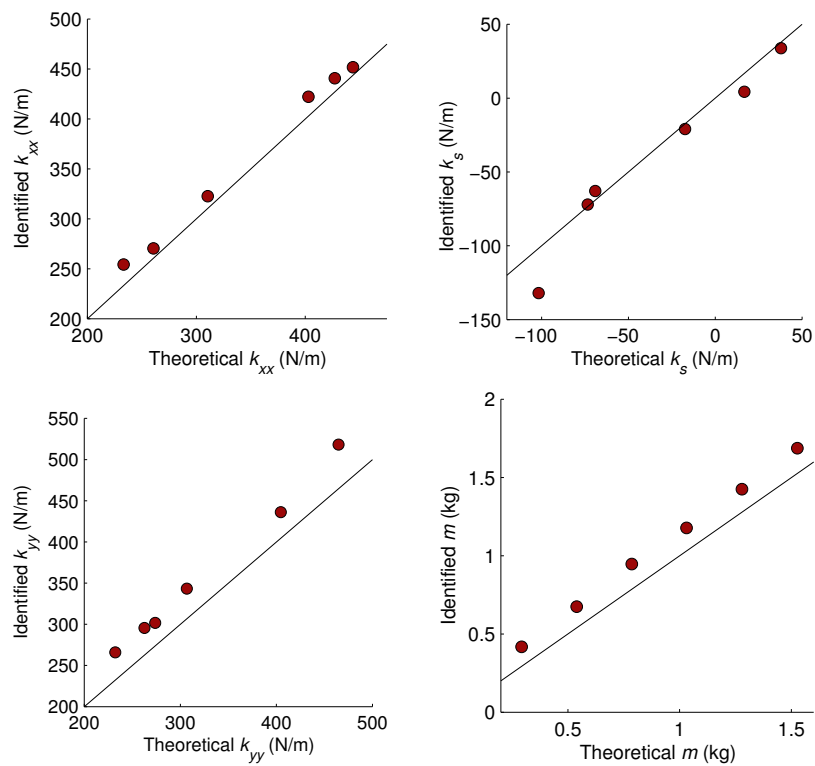
Figure 3.8: Comparison of identified and theoretical impedance parameters for the mass-spring system with underdamped perturbations. Standard error bars are smaller than the data points. Data points in perfect agreement with theoretical values would lie on the straight line.

---

6 A more detailed discussion of the sources of error in the mass-spring system impedance measurement is provided in Section 5.3.

3.5.4 *A Note on Sampling Interval*

In arm impedance identification literature, it is common to record data at sampling rates of 1 kHz or above [18, 80, 83, 94]. Since the arm's bandwidth is much smaller, this may raise concerns about oversampling. For instance, a sampling interval that is too small can over-emphasize noise in the identification signals and make model determination more sensitive [95]. Therefore, the identification was repeated with the signals downsampled to 100 Hz. This was found to have negligible impact on the identified impedance models, verifying that oversampling had not compromised the models' accuracy.

A high sampling rate did not compromise identification accuracy

3.6 RESULTS

In this section, the arm impedances identified with sinusoidal perturbations for the six participants are presented and used to plot *impedance ellipses* to compare our findings with previous studies. The data is subsequently analyzed for passivity and compared and contrasted against the impedances identified with underdamped perturbations for two of the subjects.

3.6.1 *Sinusoidal Perturbations*

Table 3.2 shows the impedance matrices for each subject identified with sinusoidal perturbations. The first 40 s of each data set was used for identification, while the final 10 s were used to validate the model through the variance accounted for (VAF) test statistic:

$$VAF = 100 \times \left(1 - \frac{\text{var}\left(f_h(t) - \hat{f}_h(t) \right)}{\text{var}\left(f_h(t) \right)} \right), \quad (3.10)$$

where $f_h(t)$ is the x or y component of $F_h(t)$ measured by the force sensor and $\hat{f}_h(t)$ is the corresponding external force component predicted by the identified impedance model. A VAF of 100% indicates that the model describes the data perfectly, while lower scores indicate a progressively poorer model fit. The fact that the VAF values were typically above 97% and never below 92% indicates that the second-order Cartesian model in (3.2) described the data very well. Standard errors were small in comparison to parameter magnitudes, indicating good reproducibility across trials. As expected

Table 3.2: Identified relaxed arm impedance with sinusoidal perturbations. Entries are averages and standard errors from four trials.

PARTICIPANT	INERTIA (kg)		DAMPING Ns/m		STIFFNESS Ns/m		X_0 (mm)	VAF	PASSIVE/ACTIVE
	m_{xx} m_{yx}	m_{xy} m_{yy}	b_{xx} b_{yx}	b_{xy} b_{yy}	k_{xx} k_{yx}	k_{xy} k_{yy}	x_0 y_0	VAF_x VAF_y	
P1	1.33 ± 0.014 -0.96 ± 0.005	-0.93 ± 0.015 1.89 ± 0.037	5.75 ± 0.242 -0.94 ± 0.169	-3.39 ± 0.197 10.60 ± 0.304	42.45 ± 1.469 -23.02 ± 2.585	-34.38 ± 1.698 125.43 ± 8.804	-3 ± 7 529 ± 9	98.7 96.2	P
P2	1.30 ± 0.021 -0.85 ± 0.010	-0.76 ± 0.008 1.36 ± 0.066	5.77 ± 0.282 -1.49 ± 0.094	-3.69 ± 0.152 9.12 ± 0.502	45.14 ± 4.250 -35.25 ± 5.820	-33.40 ± 2.835 112.49 ± 13.841	9 ± 12 537 ± 18	97.2 92.7	P
P3	1.53 ± 0.016 -0.99 ± 0.004	-0.91 ± 0.021 1.71 ± 0.054	6.02 ± 0.110 -2.40 ± 0.048	-4.27 ± 0.079 10.47 ± 0.304	39.52 ± 2.832 -26.10 ± 1.126	-30.34 ± 3.293 108.60 ± 6.496	-6 ± 3 522 ± 2	98.8 97.4	P
P4	1.42 ± 0.005 -1.05 ± 0.007	-1.01 ± 0.004 1.88 ± 0.006	4.75 ± 0.045 -2.59 ± 0.073	-3.81 ± 0.074 9.61 ± 0.245	36.61 ± 1.232 -42.97 ± 2.001	-43.45 ± 2.348 151.45 ± 4.971	-6 ± 4 529 ± 5	98.7 97.5	P
P5	1.27 ± 0.003 -0.98 ± 0.007	-0.91 ± 0.007 2.07 ± 0.013	4.81 ± 0.038 -1.83 ± 0.012	-3.19 ± 0.023 11.89 ± 0.107	38.98 ± 1.230 -31.46 ± 1.529	-25.03 ± 2.627 164.95 ± 3.965	-11 ± 3 522 ± 2	99.1 98.3	P
P6	1.11 ± 0.020 -0.81 ± 0.014	-0.74 ± 0.005 1.67 ± 0.027	3.16 ± 0.118 -0.67 ± 0.165	-1.96 ± 0.113 8.23 ± 0.142	22.64 ± 1.165 -30.26 ± 1.967	-17.28 ± 1.916 93.75 ± 6.956	-11 ± 14 518 ± 5	98.5 96.8	P

for the relaxed arm, the equilibrium positions X_0 coincided with the test location at $(x = 0 \text{ cm}, y = 52 \text{ cm})$.

3.6.1.1 *Impedance Ellipses*

To visualize the identified impedances, the **M**, **B**, and **K** matrices in (3.3) may be separated into a symmetric and an antisymmetric component as

$$\mathbf{K_s} = \begin{bmatrix} k_{xx} & \frac{k_{xy}+k_{yx}}{2} \\ \frac{k_{yx}+k_{xy}}{2} & k_{yy} \end{bmatrix}, \ \mathbf{K_a} = \begin{bmatrix} 0 & \frac{k_{xy}-k_{yx}}{2} \\ \frac{k_{yx}-k_{xy}}{2} & 0 \end{bmatrix}, \qquad (3.11)$$

such that $\mathbf{K} = \mathbf{K_s} + \mathbf{K_a}$ (and similar for **M** and **B**). The antisymmetric portion $\mathbf{K_a}$ is described by the magnitude of its off-diagonal elements. The symmetric portion $\mathbf{K_s}$ may be visualized by multiplying a rotating unit displacement

Symmetric and antisymmetric impedance

$$\begin{bmatrix} x \\ y \end{bmatrix} = \begin{bmatrix} \cos(t) \\ \sin(t) \end{bmatrix} \quad 0 < t \leq 2\pi \qquad (3.12)$$

(or one of its derivatives for damping and inertia) by the symmetric matrix component and plotting the resulting force vectors [63,66]. If these vectors are plotted so that their tips meet at the same location, their tails will lie on an ellipse as shown in Fig. 3.9.

Generation of an impedance ellipse

(a)   (b)
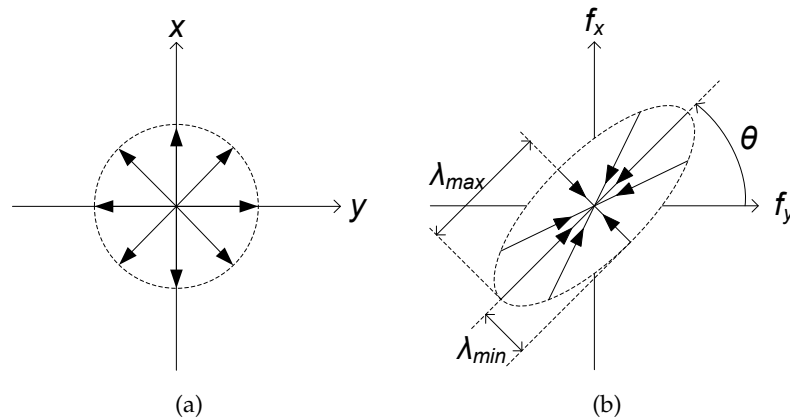
Figure 3.9: Generating an impedance ellipse: (a) a rotating unit vector is multiplied by the symmetric component of an impedance matrix to produce (b) restoring force vectors whose origins form an impedance ellipse. The forces are only collinear with displacements applied along the ellipses' major and minor axes.

The ellipse's major axis is the direction of highest impedance and its minor axis is the direction of lowest impedance. The restoring force vectors will only be collinear with perturbation applied along the ellipse's major or minor axes, which are called the *eigenvectors* of the symmetric inertia, damping, or stiffness matrix. The corresponding impedance values along these directions are known as the *eigenvalues* λ_{max} and λ_{min} of the matrix.

The ellipse is characterized by three parameters: its area, shape, and angle. The enclosed area A is proportional to the symmetric matrix's determinant and represents the overall magnitude of the symmetric impedance component. The shape R is the ratio of the ellipse's major and minor axes. Higher shape values indicate larger anisotropy in the force field. Finally, the orientation θ is the angle between the ellipse's major axis and the x-axis. For a symmetric impedance matrix

Three ellipse parameters

$$Z = \begin{bmatrix} z_{xx} & z_s \\ z_s & z_{yy} \end{bmatrix}, \tag{3.13}$$

these parameters may be calculated as follows [66]:

$$\lambda_{max,min} = \frac{1}{2}\left[z_{xx} + z_{yy} \pm \sqrt{(z_{xx} + z_{yy})^2 + 4(z_s^2 - z_{xx}z_{yy})} \right] \tag{3.14}$$

$$A = \pi \lambda_{min} \lambda_{max} \tag{3.15}$$

$$R = \frac{\lambda_{max}}{\lambda_{min}} \tag{3.16}$$

$$\theta = \text{atan}\left(\frac{\lambda_{max} - z_{xx}}{z_s} \right). \tag{3.17}$$

Fig. 3.10 shows the inertia, damping, and stiffness ellipses for Partipicant P1's data in Table 3.2 along with his arm configuration during the relaxed grasping task. Impedance ellipses for the remaining subjects are shown in Fig. 3.11. The corresponding ellipse parameters are listed in Table 3.3. The ellipse orientation and shape were quite consistent across subjects. However, as seen in previous studies, the size of the ellipses varied substantially from one participant to the next. In agreement with Tsuji et al. [77], the major axes of the inertia ellipse was roughly oriented along the forearm axis, while the major axis of the stiffness ellipse was generally oriented towards the shoulder. As Dolan et al. found [66], the damping ellipse angle was oriented between the stiffness and inertia ellipses in a majority of cases and, in agreement with Tsuji et al., was gener-

Ellipse characteristics agree with previous studies

ally oriented more closely to the stiffness ellipse. Thus, we can conclude that while the overall magnitude of arm impedance may vary between individuals, there are common patterns in its anisotropic properties across participants.
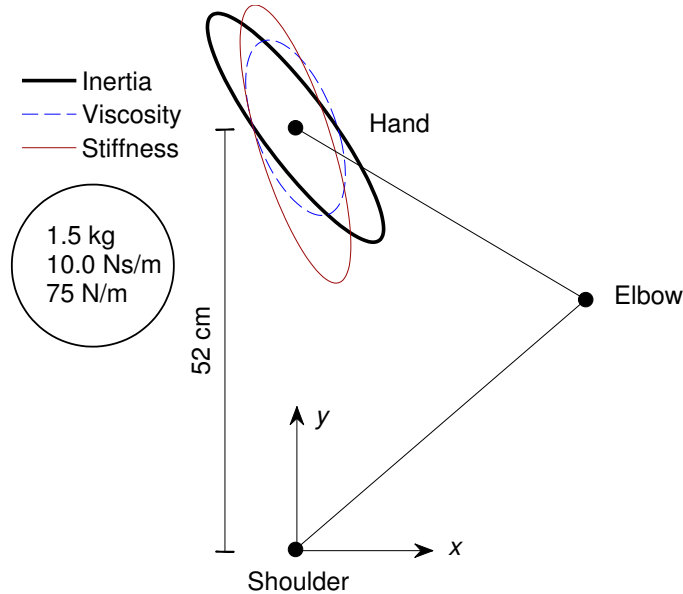
Figure 3.10: Impedance ellipses and arm configuration for Participant P1. For size comparison, the reference circle at left shows the ellipse that would be generated by an isotropic inertial, damping, or stiffness force field with the indicated impedance values along the *x* and *y* directions.

Table 3.3: Ellipse parameters from the data in Table 3.2 for the six participant's relaxed arms. Area *A* is in square-newtons, angle θ is in degrees, and shape *R* is dimensionless.

PARTICIPANT	INERTIA			DAMPING			STIFFNESS		
	A	*R*	θ	*A*	*R*	θ	*A*	*R*	θ
P1	5.1	4.1	126.7	176.8	2.3	110.9	14139.5	4.0	107.3
P2	3.5	4.1	134.0	144.3	2.4	118.6	12251.8	4.1	112.8
P3	5.4	3.9	132.3	162.9	2.9	118.1	10981.1	4.0	109.6
P4	5.1	4.5	128.6	111.3	3.5	116.4	11554.9	7.5	108.5
P5	5.5	4.2	123.5	159.8	3.2	107.7	17693.1	5.2	102.1
P6	3.9	3.9	125.1	76.2	3.0	103.7	4892.9	6.5	106.9
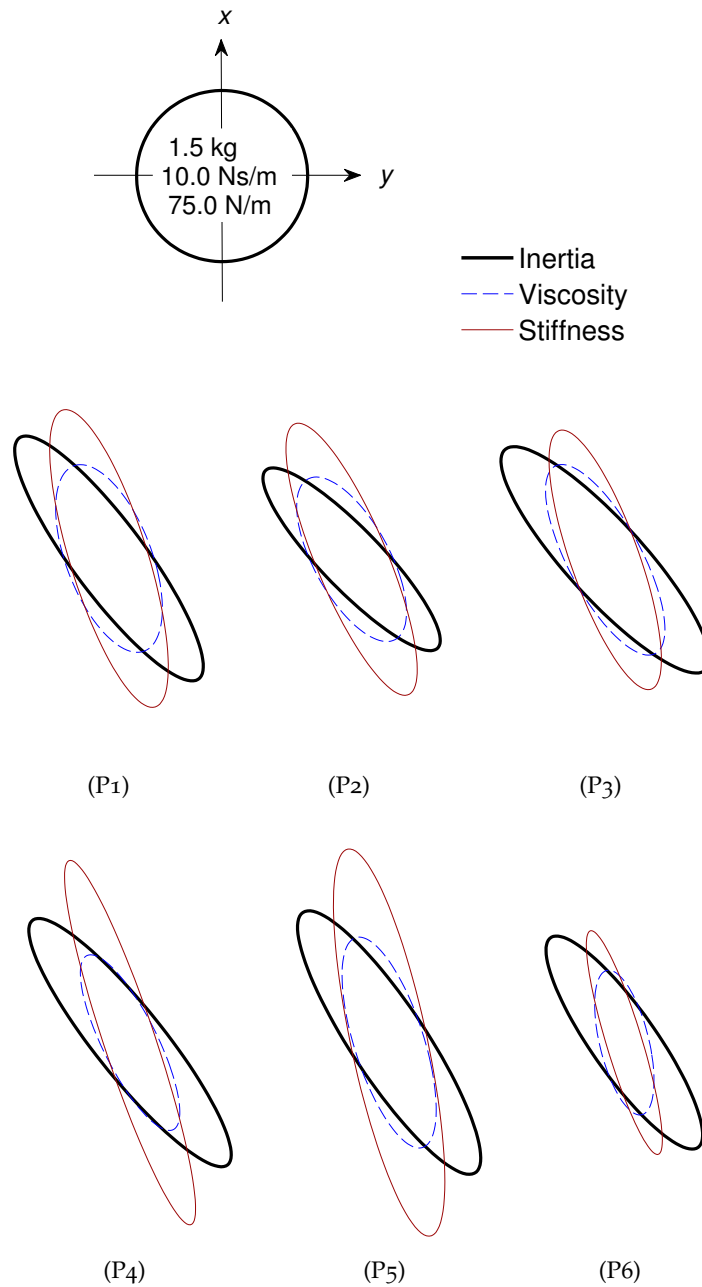
Figure 3.11: Impedance ellipses from the data in Table 3.2 for the six participant's relaxed arms. The reference circle at the top shows the ellipse that would be generated by an isotropic inertial, damping, or stiffness force field with the indicated impedance values along the x and y directions.

3.6.1.2 *Passivity Analysis*

As was discussed in Section 3.3.1, the arm's impedance may be analyzed through the model-based approach or the integral approach. For the model-based approach, we can determine whether the impedance is passive (i.e., whether the identified transfer matrix is positive-real) by applying the following theorem.

Analytical passivity conditions

THEOREM 3.2: *Consider transfer matrix* $\mathbf{Z}(s)$ *of the form in* (3.4). *Let* $k_a \doteq \frac{k_{xy} - k_{yx}}{2}$ *and* $m_a \doteq \frac{m_{xy} - m_{yx}}{2}$. *Then,* $\mathbf{Z}(s)$ *is positive real if and only if all of the following conditions are satisfied:*

$$k_a = 0 \tag{3.18}$$

$$k_{xx} \geq 0 \tag{3.19}$$

$$k_{xx}k_{yy} \geq k_{xy}k_{yx} \tag{3.20}$$

$$m_a = 0 \tag{3.21}$$

$$m_{xx} \geq 0 \tag{3.22}$$

$$m_{xx}m_{yy} \geq m_{xy}m_{yx} \tag{3.23}$$

$$b_{xx} \geq 0 \tag{3.24}$$

$$4b_{xx}b_{yy} \geq (b_{xy} + b_{yx})^2. \tag{3.25}$$

Proof. The transfer matrix $\mathbf{Z}(s)$ is positive real if and only if it satisfies the three parts of Definition 3.2.

1. *All finite poles of all elements of* $\mathbf{Z}(s)$ *are in* $\mathrm{Re}\{s\} \leq 0$.

   Since

   $$\mathbf{Z}(s) = \begin{bmatrix} \dfrac{m_{xx}s^2 + b_{xx}s + k_{xx}}{s} & \dfrac{m_{xy}s^2 + b_{xy}s + k_{xy}}{s} \\ \dfrac{m_{yx}s^2 + b_{yx}s + k_{yx}}{s} & \dfrac{m_{yy}s^2 + b_{yy}s + k_{yy}}{s} \end{bmatrix},$$

   each element has a finite pole at $s = 0$ and a pole at infinity. The pole at $s = 0$ has zero real part, so the first part of the definition is satisfied.

2. *Any pure imaginary pole* $j\omega_0$ *of any element of* $\mathbf{Z}(s)$ *is a simple pole, and the residue matrix* $\lim_{s \to j\omega_0}(s - j\omega_0)\mathbf{Z}(s)$ *in the case that* ω_0 *is finite, and* $\lim_{\omega \to \infty} B(j\omega)/j\omega$ *in the case that* ω_0 *is infinite, is positive semidefinite Hermitian.*

The poles of all elements are simple poles. The residue matrix for the pole at $s = 0$ is

$$\lim_{s \to 0}(s)\mathbf{Z}(s) = \lim_{s \to 0}\begin{bmatrix} m_{xx}s^2 + b_{xx}s + k_{xx} & m_{xy}s^2 + b_{xy}s + k_{xy} \\ m_{yx}s^2 + b_{yx}s + k_{yx} & m_{yy}s^2 + b_{yy}s + k_{yy} \end{bmatrix}$$

$$= \begin{bmatrix} k_{xx} & k_{xy} \\ k_{yx} & k_{yy} \end{bmatrix}.$$

To be Hermitian, we must have $k_{xy} = k_{yx}$, giving rise to condition (3.18):

$$k_a = 0.$$

Since this matrix is Hermitian if $k_a = 0$, being positive semidefinite is equivalent to having nonnegative leading principal minors. This yields conditions (3.19) and (3.20):

$$k_{xx} \geq 0, \quad \text{and}$$
$$k_{xx}k_{yy} - k_{xy}k_{yx} \geq 0 \Rightarrow k_{xx}k_{yy} \geq k_{xy}k_{yx}.$$

The residue matrix for the pole at infinity is

$$\lim_{\omega \to \infty} \frac{\mathbf{Z}(j\omega)}{j\omega} = \lim_{\omega \to \infty}\begin{bmatrix} m_{xx} + \dfrac{b_{xx}}{\omega} - \dfrac{k_{xx}}{\omega^2} & m_{xy} + \dfrac{b_{xy}}{\omega} - \dfrac{k_{xy}}{\omega^2} \\ m_{yx} + \dfrac{b_{yx}}{\omega} - \dfrac{k_{yx}}{\omega^2} & m_{yy} + \dfrac{b_{yy}}{\omega} - \dfrac{k_{yy}}{\omega^2} \end{bmatrix}$$

$$= \begin{bmatrix} m_{xx} & m_{xy} \\ m_{yx} & m_{yy} \end{bmatrix}.$$

Following the same reasoning as for the pole at $s = 0$, this leads to conditions (3.21) – (3.23):

$$m_a = 0,$$
$$m_{xx} \geq 0, \quad \text{and}$$
$$m_{xx}m_{yy} \geq m_{xy}m_{yx}.$$

3. *For all real positive frequencies ω for which $j\omega$ is not a pole of any element of $\mathbf{Z}(s)$, the matrix $\mathbf{H}(j\omega) \doteq \mathbf{Z}(j\omega) + \mathbf{Z}^T(-j\omega)$ is positive semidefinite.*

We find

$$\mathbf{H}(j\omega) = \mathbf{Z}(j\omega) + \mathbf{Z}^T(-j\omega)$$

$$= \begin{bmatrix} 2b_{xx} & 2m_a j\omega + b_{xy} + b_{yx} + \dfrac{2k_a}{j\omega} \\ -2m_a j\omega + b_{xy} + b_{yx} - \dfrac{2k_a}{j\omega} & 2b_{yy} \end{bmatrix}.$$

It is straightforward to show that $\mathbf{H}(j\omega)$ is Hermitian, so in order for the matrix to be positive semidefinite its leading principal minors must be nonnegative. The first principal minor yields condition (3.24):

$$2b_{xx} \geq 0 \Rightarrow b_{xx} \geq 0.$$

Taking advantage of the restriction that $k_a = 0$ and $m_a = 0$, the second principal minor simplifies to

$$4b_{xx}b_{yy} - (b_{xy} + b_{yx})(b_{xy} + b_{yx}).$$

For this expression to be nonnegative, it must satisfy condition (3.25):

$$4b_{xx}b_{yy} \geq (b_{xy} + b_{yx})^2.$$

□

Theorem 3.2 affords straightforward physical interpretation. The sets of conditions (3.18) − (3.20), (3.21) − (3.23), and (3.24) − (3.25), state that the diagonal elements of the stiffness, inertia, and damping matrices must be positive for passivity. This means that the forces generated by the arm's impedance should oppose imposed motion (i.e., dissipate mechanical energy, a passive behaviour) rather than amplify it (i.e., generate energy). Conditions (3.18) and (3.21) indicate that the stiffness and inertia matrices must have zero antisymmetry. It can be shown that the symmetric portions of the inertia and stiffness matrices may be associated with passive force fields that are conservative and have zero curl. The antisymmetric portions of these matrices, however, give rise to force contributions with non-zero curl, indicating that the hand could continuously generate power by following an appropriate closed-loop trajectory [6]. No antisymmetry condition is imposed on the damping matrix since damping forces are always dissipative and can never be associated with a conservative force field.

Physical meaning of passivity conditions

Hogan has argued that antisymmetry in the relaxed arm is the result of intermuscular feedback with unequal gains [91]. This phenomenon can occur in healthy subjects and could be especially pronounced in patients with motor control pathologies. However, in practice, random measurement and identification errors will *always* cause an identified stiffness and inertia to have antisymmetric components, even when data is collected from the mass-spring system which is known to be passive. Therefore, one must compare the relative magnitudes of the forces arising from the symmetric and antisymmetric components of stiffness and inertia to assess whether any antisymmetry in the identified matrices is an accurate reflection of the arm's biomechanics or merely the result of identification error. If the antisymmetric force contributions are sufficiently small, they may be attributed to random errors and neglected in the passivity analysis. Fig. 3.12 plots the magnitude of the symmetric and antisymmetric force components for Participant P1's stiffness matrix in Table 3.2. The plot clearly shows that the force contributions from the antisymmetric stiffness are negligibly small compared to the forces from the symmetric portion of the stiffness. The plot for the participant's inertia matrix (not shown) is similar.

Antisymmetric stiffness and inertia forces are negligibly small

50 N

(a)   (b)
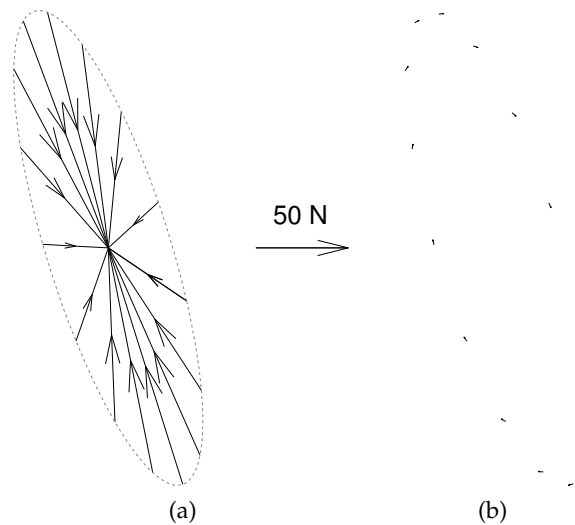
Figure 3.12: Force contributions from the (a) symmetric and (b) antisymmetric components of the stiffness matrix for Participant P1, whose antisymmetry was found from (3.26) to be 11.5%. The forces are plotted in response to 1 m unit displacements. The arrow shows the length of a 50 N force vector.

The relative contribution of the antisymmetric stiffness may be quantified by the ratio of the magnitude of the off-diagonal term

of the antisymmetric stiffness matrix $k_a = \frac{|k_{xy}-k_{yx}|}{2}$ to the maximum and minimum eigenvalues of the symmetric stiffness matrix $z_{min} \doteq k_a/\lambda_{max}$ and $z_{max} \doteq k_a/\lambda_{min}$. A single antisymmetry measure is then given by the geometric mean of these values [63, 66]:

$$z_{mean} = \sqrt{z_{min}z_{max}}. \tag{3.26}$$

The same approach may be used to quantify antisymmetry in the inertia matrix. Fig. 3.13 shows that z_{mean} values for the stiffness matrix were under 15% for all participants. In [6] and [63], which only considered stiffness and neglected higher-order dynamics, z_{mean} values of this size (Fig. 3.13b) were found to give rise to antisymmetric stiffness forces that were small in comparison to those originating from the symmetric stiffness term. This was confirmed in our study—Fig. 3.12 verified that Pariticipant P1's stiffness antisymmetry of 11.5% gave rise to small antisymmetric force contributions, and the corresponding stiffness force plots for other participants, although not shown, were similar. Fig. 3.14 demonstrates that antisymmetry in the inertia matrices was even smaller than the stiffness matrices. Therefore, only the symmetric components of stiffness and inertia were considered in the passivity analysis throughout this thesis.
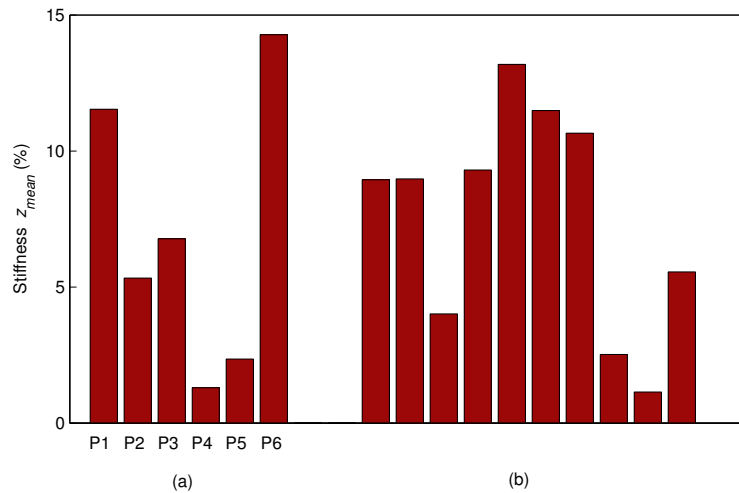
Figure 3.13: Percent antisymmetry in (a) the identified relaxed arm stiffness matrices of the six participants, and (b) the stiffness data of Mussa-Ivaldi et al. (Table II in [63]), which were considered sufficiently small to be neglected.

The arm was considered passive if the impedance $Z(s)$ in (3.4), comprising the identified $\mathbf{M_s}$, $\mathbf{B}$, and $\mathbf{K_s}$, satisfied the eight conditions in Theorem 3.2. The results of this passivity analysis are also recorded in Table 3.2. All of the data sets were found to be passive. This agrees with Hogan's analysis, and extends his results by establishing that a relaxed grasping task is passive when a full dynamic model of impedance is employed in lieu of static stiffness alone.

The impedance models and energy integrals for sinusoidal perturbations confirmed the relaxed arm is passive

This finding was confirmed by the integral approach. Fig. 3.15 shows a typical plot of the energy absorbed by each subject's arm over the course of a trial. The integral continually rises, demonstrating that the arm is absorbing rather than generating energy.
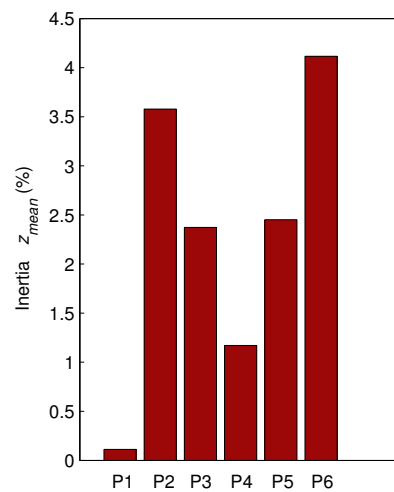
Figure 3.14: Percent antisymmetry in the identified relaxed arm inertia matrices of the six participants.
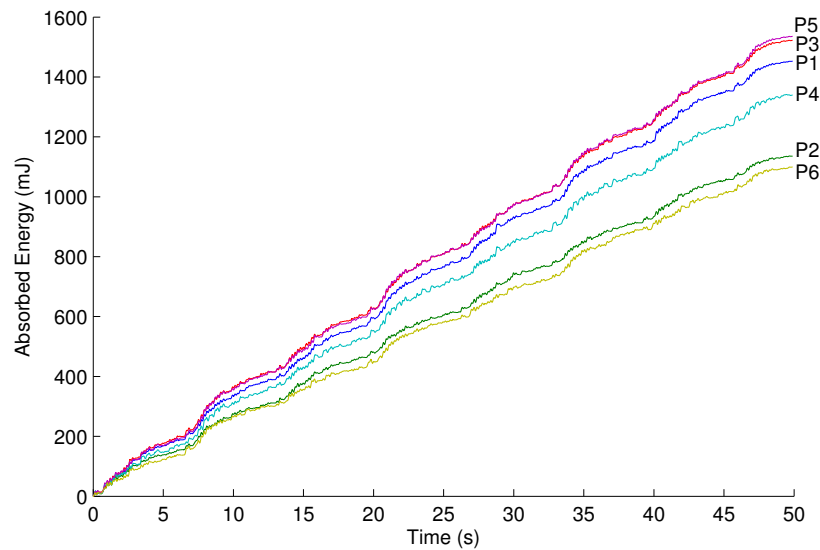
Figure 3.15: A plot of the energy absorbed by each participant's relaxed arm during a typical trial with sinusoidal perturbations.

3.6.2 *Underdamped Perturbations*

Table 3.4 shows the impedance matrices identified for two participants with underdamped perturbations. Recall that the underdamped trials applied two sets of eight perturbations evenly spaced around a circle, for a total of sixteen perturbations. To calculate VAF values, a model was identified using only the first eight perturbations and validated against the remaining eight perturbations. These VAF values were always above 88%, demonstrating that the identification procedure yielded models that described the data well.

The models were identified a second time using all sixteen perturbations to achieve even greater accuracy. The VAF values in Table 3.4 are those from the models identified with eight perturbations, while the impedance parameters are those of the models identified with sixteen perturbations.

The fact that the VAF values are slightly lower than obtained with sinusoidal perturbations reflects the fact that the underdamped perturbations yielded less data for the identification procedure, making it more difficult to identify an accurate impedance model. Since each perturbation lasted a maximum of 2 s, a maximum of 16 s of identification data was available when the model was identified with eight perturbations as opposed to 40 s in the sinusoidal per-

Underdamped perturbations yielded an acceptable, but slightly lower VAF

Table 3.4: Identified relaxed arm impedance with underdamped perturbations. Entries are averages and standard errors from four trials.

PARTICIPANT	INERTIA (kg)		DAMPING Ns/m		STIFFNESS Ns/m		X_0 (mm)	VAF	PASSIVE/ ACTIVE
	m_{xx}	m_{xy}	b_{xx}	b_{xy}	k_{xx}	k_{xy}	x_0	VAF_x	
	m_{yx}	m_{yy}	b_{yx}	b_{yy}	k_{yx}	k_{yy}	y_0	VAF_y	
P1	1.06 ± 0.025	-0.78 ± 0.005	8.80 ± 0.323	-3.77 ± 0.255	36.63 ± 3.206	-34.68 ± 4.579	-11 ± 1	87.9	P
	-1.07 ± 0.041	1.68 ± 0.038	1.56 ± 0.172	14.08 ± 0.897	-29.08 ± 5.798	140.94 ± 1.913	522 ± 2	92.2	
P4	1.43 ± 0.023	-0.88 ± 0.007	6.02 ± 0.067	-4.97 ± 0.091	45.58 ± 3.473	-45.78 ± 3.420	-17 ± 7	93.9	P
	-0.94 ± 0.055	1.38 ± 0.008	-2.24 ± 0.099	10.88 ± 0.475	-46.03 ± 13.126	123.01 ± 2.640	473 ± 2	88.6	

turbation case. Furthermore, the underdamped perturbations may have been less persistently exciting than a signal comprised of multiple sinusoids. Nonetheless, the VAF values are still sufficiently high to verify that the models did describe the arm well.

Fig. 3.16 shows the impedance ellipses for the underdamped perturbation data, with the corresponding ellipse parameters listed in Table 3.5. Comparing this table against Table 3.3, we see that the underdamped perturbations generally caused the damping magnitude to increase (indicated by a larger damping ellipse area), while the inertia and stiffness magnitudes decreased. The ellipses' shapes and orientations were not substantially affected by the different perturbation types.

Underdamped perturbations increased identified damping magnitude but did not affect ellipse shape or orientation

Most importantly, Table 3.4 confirms that the relaxed arm impedance was still found to be passive when underdamped perturbations were used. Passivity is confirmed by the energy integral plots in Fig. 3.17, which indicate that the arm absorbed energy over the course of each trial.

The impedance models and energy integrals confirmed the relaxed arm is passive
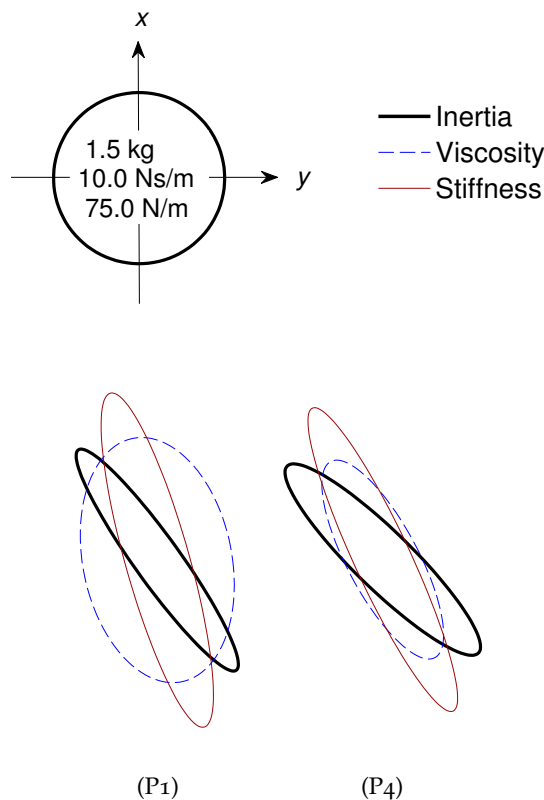
Figure 3.16: Impedance ellipses from the data in Table 3.4 for the two participant's relaxed arms.

Table 3.5: Ellipse parameters from the data in Table 3.4 for the two participants relaxed arms. Area A is in square-newtons, angle θ is in degrees, and shape R is dimensionless.

PARTICIPANT	INERTIA			DAMPING			STIFFNESS		
	A	R	θ	A	R	θ	A	R	θ
P1	2.9	5.9	125.6	385.7	1.7	101.4	13026.4	5.4	105.7
P4	3.6	4.6	135.7	165.0	3.1	118.0	10994.4	6.0	114.9
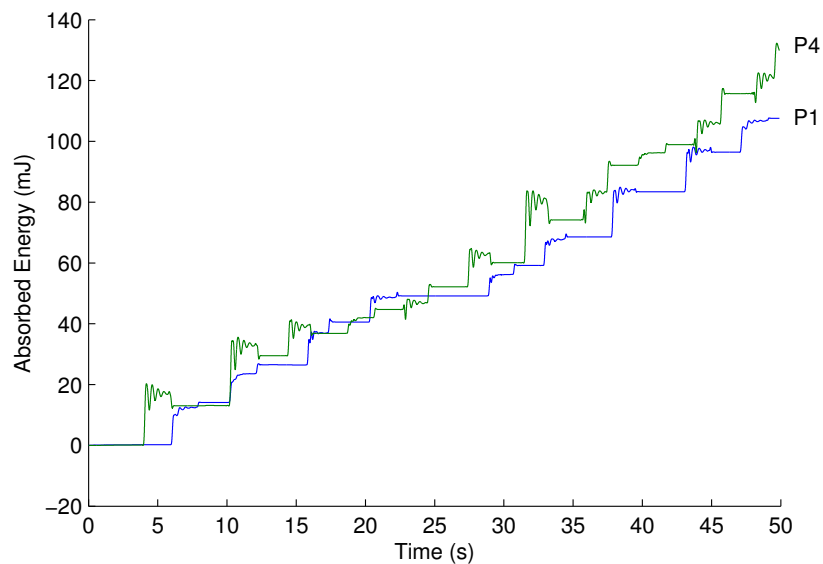
Figure 3.17: A plot of the energy absorbed by each participant's relaxed arm during a typical trial with underdamped perturbations.

3.6.3   *Excess of Passivity*

Knowing that the arm is indeed passive in a relaxed grasping task, does it also satisfy the more stringent requirement of being input strictly passive with an excess of passivity? To answer this question, we considered the impedance transfer function

$$
\mathbf{Z}(s) = \begin{bmatrix} \dfrac{m_{xx}s^2 + b_{xx}s + k_{xx}}{s} & \dfrac{m_s s^2 + b_{xy}s + k_s}{s} \\[2ex] \dfrac{m_s s^2 + b_{yx}s + k_s}{s} & \dfrac{m_{yy}s^2 + b_{yy}s + k_{yy}}{s} \end{bmatrix},
\tag{3.27}
$$

where $m_s \doteq \frac{m_{xy}+m_{yx}}{2}$ and $k_s \doteq \frac{k_{xy}+k_{yx}}{2}$. As justified in Section 3.6.1.2, this transfer matrix excludes stiffness and inertial antisymmetry from the passivity analysis. Theorem 3.1 states that this transfer matrix has an EOP of δ if and only if $\mathbf{H}(j\omega) \doteq \mathbf{Z}(j\omega) + \mathbf{Z}^T(j\omega) \geq 2\delta\mathbf{I}$. For a system that is merely passive with no EOP—such as the mass-spring model of (3.8)—this inequality can only be satisfied for $\delta = 0$.

Using the identified impedances in Table 3.2 and Table 3.4, the maximum value of δ was found such that the inequality held for all frequencies. As listed in Table 3.6, values ranging from 4.3 to 7.2 were obtained for different participants, indicating that the relaxed arm is not only passive, but also shows a sizeable EOP. Chapter 4 illustrates how this passivity excess may be exploited to improve the performance of a teleoperation system.

The relaxed arm has an excess of passivity

Table 3.6: EOP values for the relaxed arm.

PERTURBATION TYPE	PARTICIPANT	EOP (δ)
Sinusoidal	P1	5.7
	P2	5.3
	P3	6.1
	P4	5.6
	P5	6.3
	P6	4.3
Underdamped	P1	7.2
	P4	6.4

3.7 DISCUSSION

The results not only confirm Hogan's finding that the human arm behaves as a passive system during a relaxed grasping task, but also extend this result to the case where a second-order dynamic model of the arm's endpoint impedance is considered in lieu of static stiffness alone. Hogan's passivity analysis simply considered whether the identified stiffness matrices had non-neglible antisymmetric components. This chapter built upon this approach by providing a rigorous mathematical derivation of analytical conditions that the elements of a second-order mass-spring-damper impedance model must satisfy in order for it to be passive.

The results extend Hogan's findings to include a dynamic impedance model

Intuitively, it makes sense that the relaxed arm should behave as a passive system. When an individual completely relaxes his arm, it by and large acts as "dead weight" that resists any imposed motions—a passive behaviour. While it is true that the inherent spring-like properties of muscular tissues and involuntary reflex responses could cause the arm to momentarily generate energy even when it is relaxed (this can be seen in the small, momentary decreases in the energy integral plotted in Figs. 3.15 and 3.17), these energy contributions are evidently sufficiently small such that the relaxed arm's overall behaviour is passive.

The comparison of the sinusoidal and underdamped perturbations demonstrated that the design of perturbation signals can influence the magnitude of the identified impedance. Since both perturbation types had similar performance when estimating the impedance of the mechanical mass-spring system, these fluctuations are not the result of the perturbations introducing inaccuracies into the identification procedure. Rather, it seems that the apparent endpoint impedance of the arm actually does vary depending on how it is perturbed. It is reasonable to conclude that the abrupt, step-like underdamped perturbations could trigger higher levels of reflex activity compared to the slowly-varying sinusoidal perturbations, which likely accounts for the differences in the measured impedance.

Reflex activity may account for impedance variations with different perturbation types

3.8 SUMMARY

This chapter empirically confirmed previous work demonstrating that the relaxed human arm behaves as a passive system. This finding was extended to the case of a second-order dynamic impedance model and confirmed both through analysis of the impedance ma-

trices and direct calculation of the energy absorbed by the arm. While the the use of sinusoidal versus underdamped perturbations to excite the arm for identification was found to influence the magnitude of the identified stiffness, damping, and inertia, passivity was maintained regardless of the type of perturbation used.

Although these results seem to lend credence to the common assumption of human operator passivity in a teleoperation system, it is crucial to emphasize that the participants in this study simply *relaxed* their arm while it was in contact with a robot. In a practical telerehabilitation system, the human operator would be required to execute much more complex motor control tasks. For instance, a therapist might exert resistive forces against a patient to build muscle strength. The validity of the passivity assumption when the human operator resists motion will be investigated in the following chapter.

Does the passivity assumption also hold for more complex tasks?

RIGID ARM IMPEDANCE MEASUREMENT AND PASSIVITY ANALYSIS

The previous chapter established the need to revisit the conventional assumption of human operator passivity in teleoperation system control and stability analysis. We verified that the assumption holds when the operator relaxes his arm, but is it also valid for more complex tasks?

This chapter investigates the passivity assumption for the case of *rigid grasping*, in which the participants maintain their hands at a set location in the face of destabilizing force perturbations. In a telerehabilitation context for instance, a therapist may administer strength training [96] by rigidly grasping the master robot to resist motion as the patient pushes against the slave robot.

Section 4.1 presents the experimental protocols. Section 4.2 discusses the data analysis, with results shown in Section 4.3. The arm is found to be *active* during a rigid grasping task with underdamped force perturbations. The implications of these results are discussed in Section 4.4. Section 4.5 outlines how Llewllyn's absolute stability criterion may be reformulated to apply to a human operator with shortage of passivity. Concluding remarks are provided in Section 4.6.

4.1 EXPERIMENTAL PROTOCOLS

Data was collected from the same six participants of the previous chapter. As in the relaxed grasping experiments (see Section 3.4.1), each participant's arm was strapped to the robot's forearm support and supported by a sling. Perturbations were delivered at a test location 52 cm anterior to the shoulder. Unlike the relaxed grasping trials, a computer monitor displayed a circle representing the robot's handle position (i.e., the participant's hand position) and a circle corresponding to the test location. Using this visual feedback, each participant attempted to keep his or her hand centered at the test location while the robot exerted force perturbations. If the robot moved the hand away from the test location, the participant was to move his or her hand back to the test location as quickly as possible.

The participants consciously opposed movement away from a prescribed test location

Since the participants resisted the robot's motion, force perturbations were applied in lieu of position perturbations to prevent the interaction forces from exceeding safe levels. The perturbations were generated in open loop by translating the commanded Cartesian force into required motor torques through the robot's Jacobian transpose matrix. Two types of perturbations were applied:

UNDERDAMPED PERTURBATIONS   Similar to the underdamped position perturbations in the previous chapter, the robot applied a series of 16 underdamped force perturbations in directions equally spaced at 45° increments around a circle. The perturbations were applied in random order, with random duration (1.5–2.0 s) and onset time (2.0–7.0 s after the previous perturbation). These perturbations were generated by passing a 2 N force step signal through the underdamped system in (3.5). Peak interaction forces measured during the transient phase of motion were approximately 6 N.

SINUSOIDAL PERTURBATIONS   In parallel with the sinusoidal position perturbations in the previous chapter, the applied force signals in the x and y directions each comprised a sum of ten sinusoids with frequencies from 0 to 3 Hz and a peak amplitude of 6 N. Each trial was 50 s in duration.

Four underdamped peturbation trials were collected from each of the six participants, and additional sets of four sinusoidal perturbation trials were collected from three of the participants. A segment of typical data from each perturbation type is shown in Fig. 4.1.

4.2   ANALYSIS

The arm's impedance was estimated by fitting the data to the same second-order Cartesian model (3.7) that was used for the relaxed arm. There is an important distinction in the physical meaning of the identified values of **M**, **B**, **K**, and X_0 between the relaxed and rigid grasping tasks.

In both the relaxed and rigid grasping tasks, the data used to identify human arm impedance is collected from a closed-loop system (Fig. 4.2). The force sensor measures the total force the human exerts on the robot, $F_h = F_h^* - Z_h X$, where F_h^* is the human's voluntary force contribution, Z_h the human arm's impedance, and X the hand's displacement from the test location.
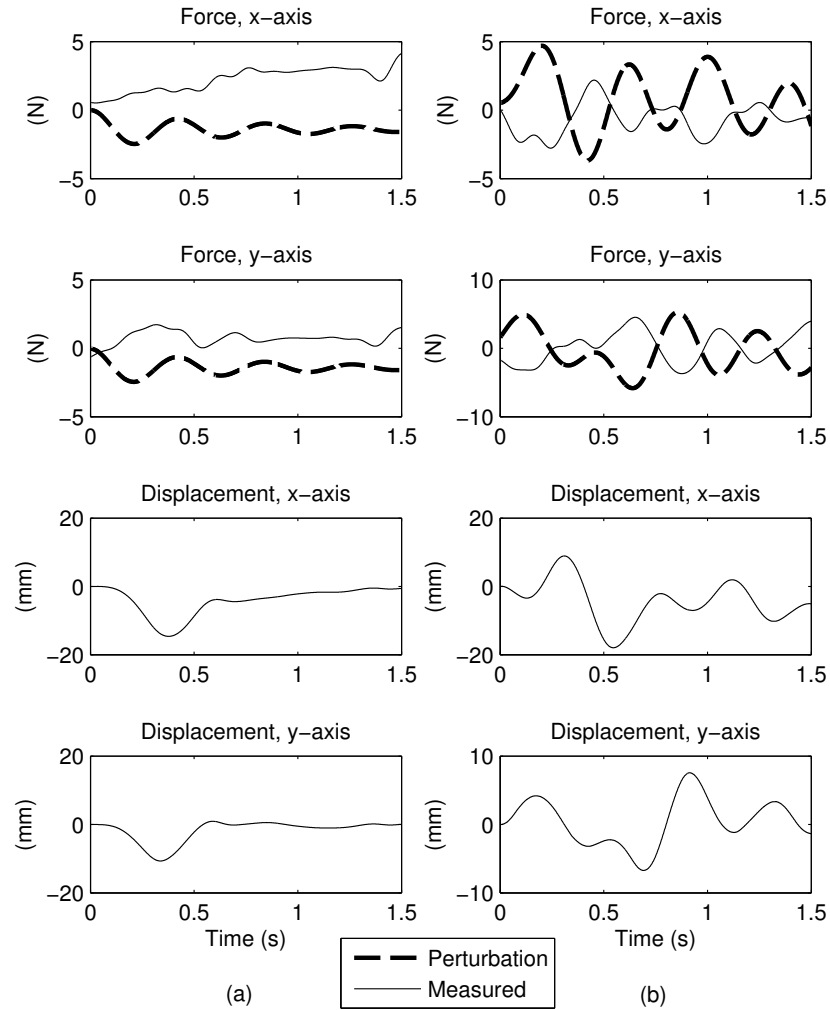
Figure 4.1: Typical force and position signals for the rigid arm with (a) underdamped perturbations and (b) sinusoidal perturbations. Dashed lines indicate the force perturbation signals the robot is commanded to exert on the human. The force sensor measures the force exerted *by the human on the robot*. The measured and perturbation force signals correspond to F_h and F_r^*, respectively, in Fig. 4.2b.
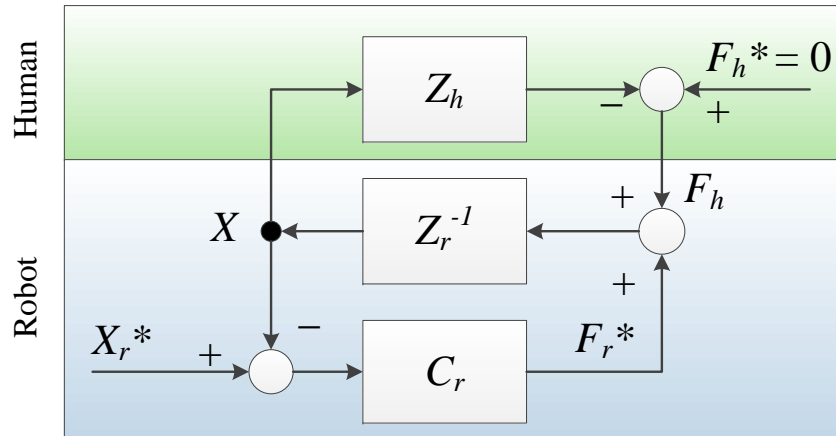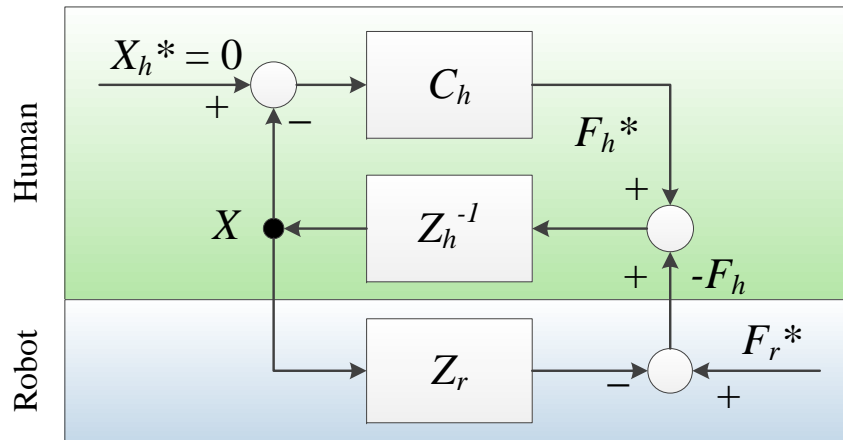
Figure 4.2: System dynamics diagram for (a) a relaxed grasping task with position perturbations (robot is closed-loop position controlled) and (b) a rigid grasping task with force perturbations (robot is open-loop force controlled). Human and robot impedances are Z_h and Z_r, respectively. The force sensor measures F_h.

During a relaxed grasping task as in Fig. 4.2a, the robot's position controller C_r tracks a reference perturbation signal X_r^*, causing the robot to apply a force F_r^* to its end-effector and move to position X. Since the human does not consciously intervene in a relaxed grasping task, his voluntary force contribution F_h^* is zero. We therefore have

When the arm is relaxed, we can directly identify Z_h

$$F_h = -Z_h X. \tag{4.1}$$

Since both F_h and X are measured, Z_h can be identified directly from the closed-loop data according to (3.7).

In the rigid grasping task, on the other hand (Fig. 4.2b), the human is instructed to minimize displacements ($X_h^* = 0$) in the face of robot-exerted force perturbations F_r^*. These forces act on the admittance of the human arm and move the hand away from the test location to a position X. Informed by visual feedback, the CNS (modeled by position controller C_h in Fig. 4.2b) responds by causing the human to consciously exert a force F_h^* to counteract this motion. A negative feedback loop from $-F_h$ to X thus exists, with Z_h^{-1} in the feedforward path and C_h in the negative feedback path, such that $\frac{X}{-F_h} = \frac{Z_h^{-1}}{1+Z_h^{-1}C_h}$. This expression simplifies to

When the arm is rigid, we can only identify the combined effects of Z_h and C_h

$$F_h = -(C_h + Z_h)X. \tag{4.2}$$

In other words, the identification results for a rigid grasping task are influenced by both the physical properties of the arm (Z_h, which arises from the arm's intrinsic mechanics and involuntary reflex responses) and additional dynamics introduced by the human's voluntary position control response (C_h). While the identified model may still be termed an "impedance" since it relates a position input to a force output, the position control dynamics of the CNS are subsumed into the identified impedance matrices.

As in the previous chapter, the raw data was passed through the smoothing filter to remove noise and derivatives were calculated from the first and second derivative filters (see Section 3.5). The values of **M**, **B**, **K**, and X_0 were identified by applying least squares regression to (3.7). Passivity was assessed through both the impedance model approach of Theorem 3.2 and the integral approach of (3.1). As justified in Section 3.6.1.2, antisymmetric components of the stiffness and inertia matrices were ignored when applying the impedance model approach.

4.3 RESULTS

4.3.1 *Underdamped Perturbations*

The impedance matrices identified with underdamped perturbations are shown in Table 4.1. The elements of the stiffness matrices were generally larger for rigid grasping compared to the relaxed grasping stiffness in Table 3.2, which was expected as arm stiffness increases with grip strength [77]. The arm equilibrium positions X_0 were very close to the test location.

These parameters were identified from the first eight perturbations of each dataset and used to calculate the VAF on data from the remaining eight perturbations. The VAF values never exceeded 50% and, in a few cases, fell below 10%. This demonstrates that the identified models did not accurately capture the dynamics of the rigid grasping task. The parameters also have larger standard errors compared to the relaxed grasping case, indicating a higher inter-trial variability. As will be discussed later, these modelling inaccuracies are due to complex—and possibly nonlinear and time-varying—dynamics introduced by the CNS position control response that cannot be fully captured by an LTI model.

VAF values were low for underdamped perturbations due to CNS position control dynamics

Fig. 4.3 shows typical plots of the energy absorbed by each participant's arm calculated over the the course of a single trial with underdamped perturbations. In stark contradiction with the conventional assumption of human operator passivity, the integral is clearly decreasing, indicating the arm is *generating energy* and behaving *actively*. The final column of Table 4.1 indicates that application of Theorem 3.2 likewise found the identified rigid arm models to be active. It is important to note that these rigid grasping impedance models were found to be active even though antisymmetric components of stiffness and inertia—which are potential sources of activity—were excluded from the passivity analysis. Caution should be exercised in drawing conclusions based on these rigid grasping impedance models, however, as the limited model validity makes it impossible to conclusively demonstrate passivity or activity through the impedance model approach.

Passivity analysis through the integral approach showed the arm was active for underdamped perturbations

Table 4.1: Identified rigid arm impedance with underdamped perturbations. Entries are averages and standard errors from four trials.

PARTICIPANT	INERTIA (kg)		DAMPING Ns/m		STIFFNESS Ns/m		X_0 (mm)	VAF	PASSIVE/ ACTIVE
	m_{xx}	m_{xy}	b_{xx}	b_{xy}	k_{xx}	k_{xy}	x_0	VAF_x	
	m_{yx}	m_{yy}	b_{yx}	b_{yy}	k_{yx}	k_{yy}	y_0	VAF_y	
P1	2.04 ± 0.171	-1.90 ± 0.252	-9.06 ± 0.832	1.09 ± 0.913	404.30 ± 38.525	-250.17 ± 45.749	-9 ± 1	35.2	A
	-1.16 ± 0.188	1.97 ± 0.119	2.34 ± 0.467	-0.82 ± 1.428	-125.00 ± 51.191	504.17 ± 22.153	520 ± 1	20.1	
P2	1.42 ± 0.163	-1.57 ± 0.291	-8.79 ± 0.661	2.70 ± 1.019	255.12 ± 30.239	-186.42 ± 58.642	-5 ± 13	47.4	A
	-0.47 ± 0.174	0.23 ± 0.340	0.23 ± 0.634	-2.07 ± 0.528	-16.34 ± 34.964	194.69 ± 50.100	525 ± 10	12.0	
P3	0.24 ± 0.264	-0.83 ± 0.067	-7.81 ± 0.252	1.14 ± 0.192	92.38 ± 33.254	-52.56 ± 12.085	-13 ± 17	18.0	A
	-0.37 ± 0.082	-0.16 ± 0.289	0.83 ± 0.358	-2.99 ± 0.507	-0.99 ± 13.361	87.96 ± 64.991	524 ± 7	8.6	
P4	1.45 ± 0.148	-1.52 ± 0.290	-4.71 ± 0.106	-0.83 ± 1.846	337.34 ± 24.147	-90.18 ± 84.049	-5 ± 1	38.5	A
	-0.56 ± 0.107	1.25 ± 0.587	-1.41 ± 0.480	-4.64 ± 1.813	-7.50 ± 14.368	677.19 ± 145.646	461 ± 1	27.3	
P5	1.47 ± 0.058	-1.60 ± 0.761	-11.18 ± 0.763	-8.38 ± 2.128	419.46 ± 6.657	3.70 ± 213.856	-11 ± 2	29.7	A
	0.14 ± 0.152	2.60 ± 0.278	-3.28 ± 1.249	-0.10 ± 2.327	236.26 ± 26.730	$1,056.63 \pm 89.038$	520 ± 1	20.9	
P6	1.13 ± 0.222	-0.950 ± 0.225	-9.06 ± 0.607	1.09 ± 0.882	82.95 ± 9.198	-27.43 ± 11.491	-3 ± 2	45.8	A
	-0.38 ± 0.196	0.58 ± 0.339	1.42 ± 0.775	-5.36 ± 0.706	-15.58 ± 10.442	180.03 ± 40.776	522 ± 5	6.9	
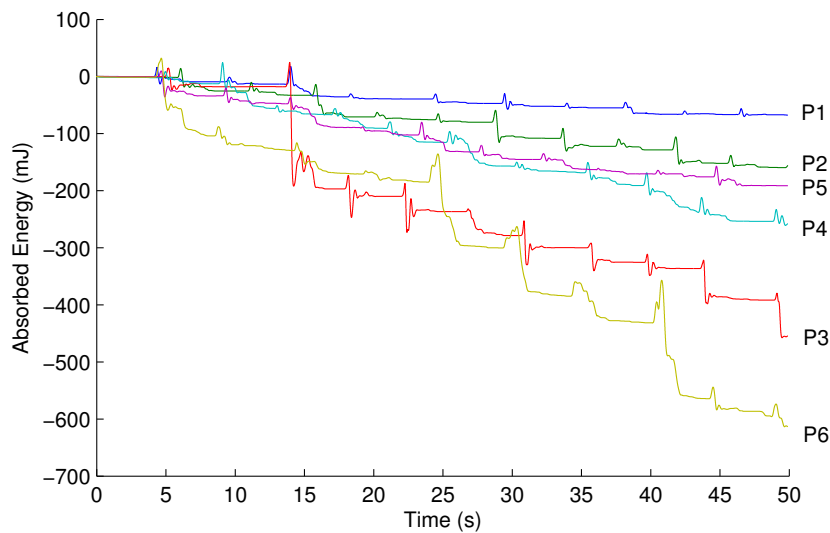
Figure 4.3: Plot of the energy absorbed by each participant's rigid arm during a typical trial with underdamped perturbations. Negative values indicate that energy is being *generated*.

4.3.2 *Sinusoidal Perturbations*

Table 4.2 shows the impedance values identified for the three participants who performed rigid grasping with sinusoidal perturbations. Again, the stiffness is larger than in the relaxed grasping case. More importantly, the VAF values for these trials are noticeably improved over the underdamped perturbation case, ranging from 62.9% to 80.4%. The standard errors are also smaller, indicating less inter-trial variability. This indicates that the models identified with the sinusoidal perturbations came closer to capturing the arm's dynamics than those identified with underdamped perturbations.

Models identified with sinusoidal perturbations showed higher VAF

Analyzing passivity through the integral approach in Fig. 4.4 clearly shows that the energy absorbed by each participant's arm over a typical trial steadily increased, demonstrating *passive* behaviour. In contrast, Table 4.2 indicates that the impedance model approach found these models to be *active*. Although the sinusoidal perturbation models achieved higher VAF scores than the underdamped perturbation models, this discrepancy indicates that they still did not fully describe the arm's dynamics. This model identification error caused the model-based passivity approach to yield inaccurate results that were not supported by the integral analysis.

Passivity analysis through the integral approach confirmed the arm was passive for sinusoidal perturbations

Table 4.2: Identified rigid arm impedance with sinusoidal perturbations. Entries are averages and standard errors from four trials.

PARTICIPANT	INERTIA (kg)		DAMPING Ns/m		STIFFNESS Ns/m		X_0 (mm)	VAF	PASSIVE/ACTIVE
	m_{xx}	m_{xy}	b_{xx}	b_{xy}	k_{xx}	k_{xy}	x_0	VAF_x	
	m_{yx}	m_{yy}	b_{yx}	b_{yy}	k_{yx}	k_{yy}	y_0	VAF_y	
P1	-0.10 ± 0.041	-0.35 ± 0.067	13.01 ± 0.413	-5.81 ± 0.617	195.97 ± 11.985	92.14 ± 20.836	-9 ± 2	73.6	A
	-0.90 ± 0.051	-0.26 ± 0.133	-2.93 ± 0.440	34.30 ± 1.171	20.81 ± 12.950	651.15 ± 24.637	520 ± 0	80.4	
P4	-0.03 ± 0.071	-0.53 ± 0.100	11.64 ± 0.793	-8.97 ± 0.758	155.98 ± 11.530	79.86 ± 21.805	-12 ± 3	74.1	A
	-0.93 ± 0.027	-0.57 ± 0.171	-6.37 ± 0.972	26.12 ± 1.295	43.86 ± 4.519	482.11 ± 57.284	520 ± 1	62.9	
P6	0.19 ± 0.033	-0.59 ± 0.045	5.06 ± 0.312	-1.52 ± 0.520	50.81 ± 3.091	3.98 ± 9.559	-6 ± 4	67.1	A
	-0.65 ± 0.030	-1.37 ± 0.254	-0.04 ± 0.066	31.28 ± 0.761	10.74 ± 4.588	214.47 ± 19.922	519 ± 2	73.8	
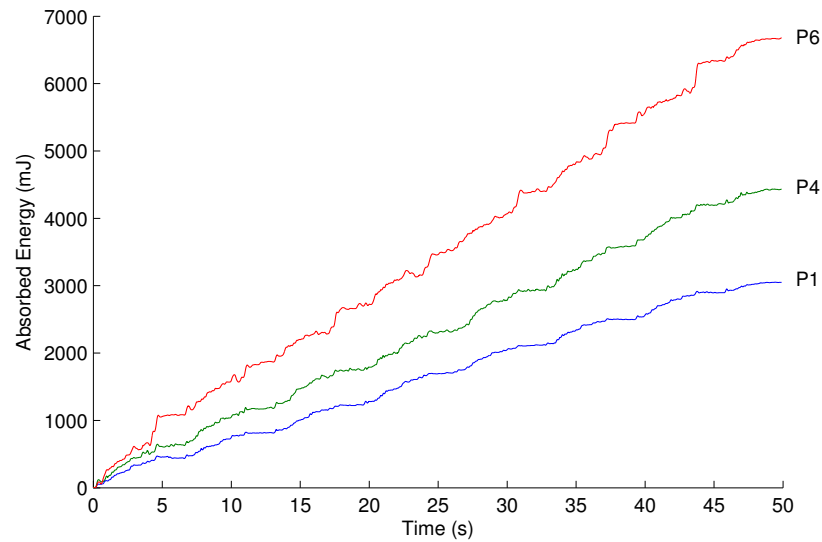
Figure 4.4: Plot of the energy absorbed by each participant's rigid arm during a typical trial with sinusoidal perturbations.

4.4 DISCUSSION

Table 4.3 summarizes the passivity analyses in the current and preceding chapters. The relaxed arm was found to be passive regardless of the type of perturbation used. For rigid grasping, energy integral analysis showed passive behaviour for sinusoidal perturbations and active behaviour for underdamped perturbations. The impedance model approach found the rigid arm to be active for both perturbation types, but these results are erroneous due to the limited model validity.

Table 4.3: Summary of passivity analysis for relaxed and rigid grasping tasks.

Task	Analysis Approach	Sinusoidal Perturbations	Underdamped Perturbations
Relaxed Grasping	Impedance Model	Passive	Passive
	Integral	Passive	Passive
Rigid Grasping	Impedance Model	Active (limited model validity)	Active (limited model validity)
	Integral	Passive	Active

4.4.1 *Energy Absorption Analysis*

Further insights into these results may be obtained by analyzing the arm's energy absorption over the course of a single underdamped perturbation. Fig. 4.5a shows a typical plot of the energy Participant P1's arm absorbed during a single underdamped perturbation in a relaxed grasping task. The distance of the hand from the test location (i.e., the magnitude of the two-dimensional displacement vector) is plotted on the right axis. We observe that when the arm is relaxed, its impedance causes it to resist motion away from equilibrium, absorbing energy when the position perturbation displaces it from the test location. When the perturbation's oscillations cause the hand to move back towards the test location, there is a small decrease in the arm's energy. This is the result of the spring-like component of the arm's stiffness releasing potential energy that was stored when the arm was initially perturbed away from the test location. Nonetheless, the total energy absorbed clearly increases over the duration of the perturbation, confirming that relaxed grasping is a passive task.

The relaxed arm resists motion and behaves passively

Fig. 4.5b shows the same plot for the rigid grasping task with the underdamped force perturbations with 2 N steady-state amplitude. As the participant cannot anticipate when the force perturbation will be applied, his reaction time (approximately 150 ms [97]) prevents him from voluntarily resisting motion immediately after a perturbation is applied. Therefore, his arm absorbs energy as it is involuntarily displaced away from the test location. Once the participant realizes that his hand has been perturbed from its target position, he consciously exerts force to overcome the robot's force and move his hand back to the test location as quickly as possible.[1] This movement requires the participant to generate energy, causing the stored energy to decrease substantially. For the remainder of the perturbation, the arm's energy undergoes smaller fluctuations while the participant consciously exerts the force required to maintain his hand at the test location.

The rigid arm absorbs energy when initially displaced from test location and generates energy during the return movement

Classifying the rigid grasping task as "active" or "passive" depends on whether the energy generated in the return to the test location outweighs the energy absorbed when the hand was initially displaced away from the test location. Fig. 4.5c shows the absorbed energy for an additional rigid grasping task with Participant P1, in which the steady-state amplitude of the force perturbation was

---

1 Recall that the participant was instructed to prevent his hand from deviating from the test location, and not merely to slow down any motion imposed upon his hand without regard for where his hand came to rest.

(a)

(b)

(c)
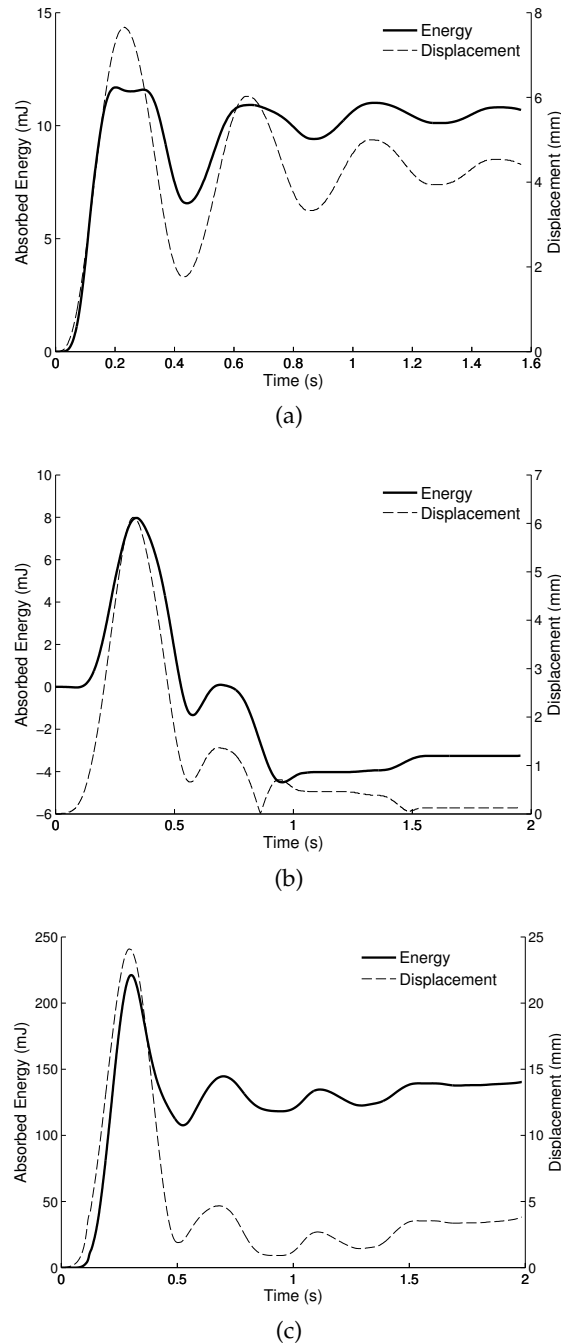
Figure 4.5: Typical plots of absorbed energy (solid line, left axis) and hand displacement from the test location (dashed line, right axis) for a single underdamped perturbation applied at $t = 0$ s in (a) relaxed grasping, (b) rigid grasping (2 N perturbation), and (c) rigid grasping (8 N perturbation). Plots show the magnitude of the two-dimensional displacement vector. Data was collected from Participant P1. The arm is assumed to have zero stored energy prior to the onset of the perturbation.

increased from 2 N to 8 N. In this case, the robot applies a large perturbation which moves the hand away from equilibrium at a high velocity. This causes the energy initially absorbed by the hand to be larger than the energy generated when the participant returns his hand to the target position, such that the overall task is passive. For the 2 N force perturbation case, however, the robot perturbs the hand away with less force, resulting in a slower movement velocity than the 8 N case. The energy absorbed by this process is less than the energy generated during the return movement, and the task is found to be active. This explains why Fig. 4.3 shows that Participants P3 and P6 generated more energy than the other participants. Table 4.1 indicates that these two participants had relatively lower impedances. Their hands were therefore displaced further from the test location when each perturbation was applied, requiring them to expend a larger amount of energy to overcome the perturbation and return their hands to the test location.

The arm's passivity or activity depends on the balance of energy absorption and generation for a given task

This reasoning also accounts for why the integral approach found the rigid arm to be active for underdamped perturbations but passive for sinusoidal perturbations. With underdamped force perturbations, the participant consciously initiates a movement in the opposite direction of each perturbation, requiring the arm to generate energy and behave actively. With sinusoidal perturbations, however, it is much more difficult for the participant to consciously oppose the force perturbations by executing a deliberate position control response. Unlike the discrete underdamped perturbations, the direction of the continuous sinusoidal perturbations is never constant. By the time the participant has detected the perturbation direction and determined the direction in which he must move his hand to overcome it, it is very likely that the direction of the perturbing force has already changed. Unable to initiate proper movements to overcome each unique segment of the perturbations, the participant will instead resort to minimizing displacements by simply increasing the overall impedance of his arm through muscular co-contraction. The CNS position controller therefore plays a relatively smaller role, causing the arm to behave more like a passive dead weight.

Sinusoidal perturbations diminish the CNS position control dynamics and suppress activity

According to (4.2), the identified impedance is the *total* of the arm's physical impedance and the dynamics contributed by the position control response of the CNS. The arm impedance model of (3.2) inherently assumes that the 2-dimensional position control dynamics of the CNS can be captured by an LTI second-order model. This is evidently not the case, as the rigid arm models identified with underdamped perturbations in Table 4.1 have high intertrial

The CNS dynamics are not accurately captured by the LTI second-order model structure

variability and low VAF. When sinusoidal perturbations are used in lieu of underdamped perturbations, the contributions of C_h in (4.2) to the total limb impedance are smaller than those of Z_h. As a result, the second-order model can come closer to describing the system dynamics, explaining the slightly improved VAF by the models in Table 4.2. These models are still invalid, however, since they describe an active system when the integral analysis plainly shows the rigid arm to behave passively with sinusoidal perturbations. Thus, even though the CNS dynamics are suppressed by sinusoidal perturbations, they are not completely eliminated.

4.4.2 *One-Dimensional Perturbations*

An additional experiment was therefore performed with Participant P2 in an effort to derive an arm impedance model that could accurately capture the CNS position control response. We simplified the perturbations to confine motion to a single direction, enabling us to employ more general model structures that may be able to capture the CNS position control dynamics. Underdamped perturbations were delivered along the y-axis in Fig. 3.3, centered at the same test location ($x = 0$ cm, $y = 52$ cm) used in in the 2-dimensional experiments. A high-gain proportional controller restricted the robot from moving off the y-axis. Underdamped force perturbation signals were generated by passing a ± 2 N random binary sequence (RBS) force signal through the underdamped system in (3.5). Five trials were performed, each lasting 50 s, with the first 40 s of data being used for identification and the final 10 s of data for model validation. Typical force and position data are shown in Fig. 4.6.

Can the CNS dynamics be succesfully modelled in one dimension?

The Prediction Error Method (PEM) (refer to [95] for details) was used to identify a variety of discrete-time transfer function models from the data, but all of the identified models performed poorly under validation tests. Improved results were obtained by directly identifying a continuous-time transfer function from the sampled data via the Simplified Refined Instrumental Variable (SRIV) method described in [98] and incorporated in the MATLAB function `tfest`. In brief, this approach involves assuming a transfer function structure with known orders in the numerator and denominator. The assumed model structure yields differential equations in which the measured input and output signals and their derivatives are related by unknown constant parameters. As numerical differentiation can be noise-prone, these equations are low-pass filtered by a *state vari-*
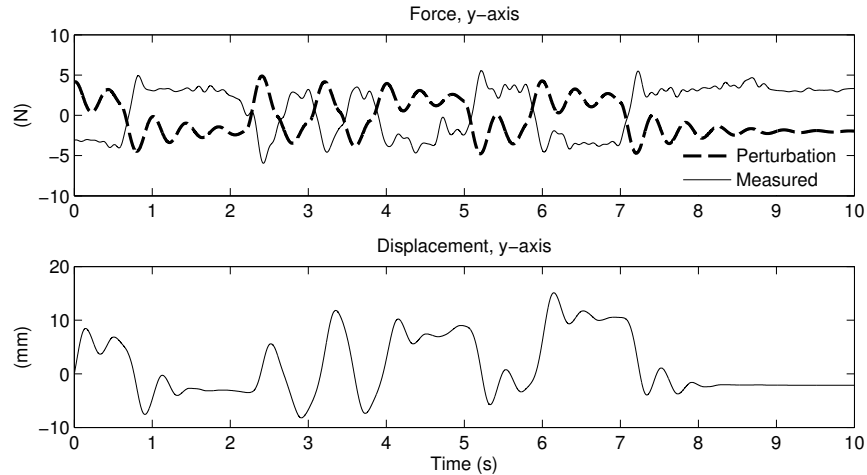
Figure 4.6: Typical force and position signals for the rigid arm with one-dimensional underdamped force perturbations. Dashed lines indicate the force signals the robot is commanded to exert.

able filter. The parameters that minimize the error between the measured output signal and the model's predicted output signal are subsequently calculated from the filtered equations by applying *instrumental variable* regression.

Through rigorous experimentation, a transfer function with four poles and three zeros was found to yield the best fit.[2] The VAF values listed in Table 4.4 indicate that the accuracy of the identified model varied widely from one trial to the next, but were generally too low for the identified models to be considered valid. This is confirmed by Fig. 4.7, which compares the measured force values from the final 10 s of Trial 1 with the forces predicted by the corresponding identified model. Although the model captures the general trends in the measured force signal, there are still large discrepancies between the measured and predicted signals.

The PEM and SRIV methods permit identification of very general LTI model structures, but both techniques failed to identify valid rigid grasping arm impedance models even when motion was restricted to one dimension. This indicates that the dynamic impedance contributions of the CNS cannot be accurately captured by an LTI model, making it extremely challenging to perform model-based passivity analysis.

Even in one dimension, the CNS position control dynamics are non-LTI

---

2 Note that `tfest` restricts the number of poles to be greater than or equal to the number of zeros.

Table 4.4: VAF by 1D rigid grasping impedance models.

TRIAL	VAF
1	43.6
2	69.1
3	-2.9
4	27.3
5	70.1
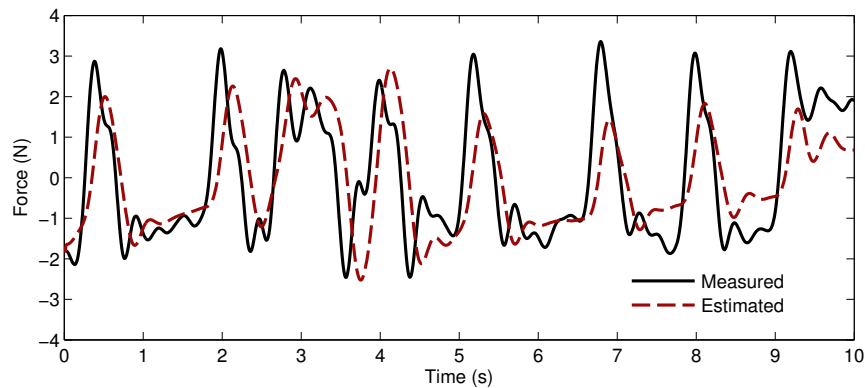
Figure 4.7: Comparison of measured and estimated force signals for the rigid arm with one-dimensional perturbations.

4.4.3 *The CNS Causes Activity*

In both the two- and one-dimensional cases, the rigid arm impedance models had low VAF values due to the CNS dynamics. This highlights a dilemma in evaluating the validity of the human operator passivity assumption. In order to rigorously demonstrate that the human arm may be active in certain tasks, we would ideally like to derive a valid human arm impedance model that shows activity. Due to the complexity of the CNS position control response, it is extremely challenging to identify a model that can account for the CNS dynamics. Even if sinusoidal perturbations are used to attenuate these dynamics, or if the experiments are simplified to one dimension to permit identification of more general model structures, the rigid arm impedance cannot be accurately represented by an LTI model. Valid identification results may only be obtained when, as in Chapter 3, the participant relaxes his arm and thereby completely eliminates the CNS position control response. *However, the energy absorption integrals demonstrate that it is precisely the CNS*

The CNS dynamics are required for active behaviour but make it difficult to identify accurate impedance models

position control that is the source of active behaviour. If the identification experiment is designed to eliminate the CNS *control by relaxing the arm, accurate models can be identified but the active behaviour disappears.*

Although the integral approach is less rigorous, Fig. 4.3 confirms that the every participant's arm generated energy during the rigid grasping trials with underdamped perturbations. These results are intuitive: when the human operator voluntarily moves the master robot in a teleoperation system, he causes a displacement in the direction of his applied force. In other words, he does mechanical work on the robot, which by definition requires him to generate energy.

The integral approach consistently shows the rigid arm is active for underdamped perturbations

The rigid grasping task in this paper consisted of merely resisting disturbance forces to maintain the hand at a particular position. Yet even for this simple task, the human operator was found to inject energy into the system. In many practical teleoperation applications, the human operator is required to complete much more complex movements. The assumption of human operator passivity needs to be carefully re-examined in these contexts.

4.4.4   *Shortage of Passivity*

We calculated the arm's SOP during the rigid grasping task with underdamped perturbations. Since the impedance models for this task were not accurate, SOP was not evaluated from Theorem 3.1. Instead, it was measured directly from the definition of passivity in (3.1) by finding the largest value of λ such that the following inequality held over the course of an entire trial:

$$\int_0^t F(\tau) \cdot \dot{X}(\tau) d\tau \geq \beta - \lambda \int_0^t \dot{X}(\tau) \cdot \dot{X}(\tau) d\tau, \tag{4.3}$$

where the arm's initial energy β at the start of the trial is assumed to be zero. Average values of λ from the four trials for each of the participants are recorded in Table 4.5.

4.5   REFORMULATION OF LLEWELLYN'S CRITERION

Given that human operator passivity should not be assumed *a priori* but rather evaluated on a task-by-task basis, how should teleoperation system design be modified to account for shortage or excess of passivity? This section outlines how Llewellyn's absolute stability criterion—which conventionally assumes human operator

How may Llewllyn's criterion be modified for a human operator with SOP or EOP?

Table 4.5: SOP values for the rigid arm with underdamped perturbations

PARTICIPANT	SOP (λ)
P1	8.6
P2	8.4
P3	6.5
P4	8.4
P5	15.4
P6	10.8

passivity—may be extended to the case of a human operator with SOP or EOP.

Llewellyn's criterion is only valid for motion in one dimension, such that the human arm is modelled by a single-input single-output (SISO) impedance transfer function. Although this thesis identified arm impedance in 2 DOFs for a more complete characterization of arm dynamics, the identification and passivity analysis techniques that were presented may be readily simplified to one-dimensional models. In the 1-DOF case, Definition 3.2 simplifies as follows:

LEMMA 4.1: *For a SISO transfer function with n = 1, Condition 3 in Definition 3.2 simplifies to Re $Z(j\omega) \geq 0, \forall \omega \in \mathbb{R}$. In other words, the Nyquist diagram of a passive transfer function lies entirely in the right half plane (Fig. 4.8a).*
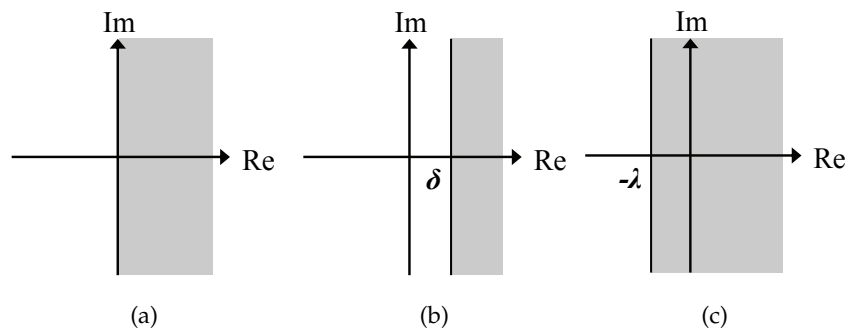
Figure 4.8: Regions of the complex plane containing the Nyquist diagrams of (a) a passive system, (b) an input strictly passive system with EOP of δ, and (c) an input non-passive system with SOP of λ.

Also, the transfer matrix's excess or shortage of passivity can be evaluated through a simplified version of Theorem 3.1:

LEMMA 4.2: *Consider a SISO system with transfer function $Z(s)$, where all poles have negative real parts. The system is input strictly passive with EOP of $\delta > 0$ if and only if $\operatorname{Re} Z(s) \geq \delta$, such that the Nyquist diagram of $Z(s)$ lies to the right of the vertical line at δ (Fig. 4.8b). Similarly, for an input non-passive transfer function with SOP of $\lambda > 0$ the Nyquist diagram is in $\operatorname{Re} Z(s) \geq -\lambda$ (Fig. 4.8c).*

To investigate stability of a teleoperation system, the teleoperator is modelled as a two-port network terminated by the human operator and the environment (Fig. 4.9). The two-port network is *absolutely stable* when the coupled system is stable for any passive but otherwise arbitrary terminations (z_{t1} and z_{t2} in Fig. 4.9a). Absolute stability of the two-port network is equivalent to the driving-point impedance (Z_{a1} in Fig. 4.9b) seen from one port of the two-port network being passive when the termination of the second port is passive.

Definition of absolute stability

(a)

(b)
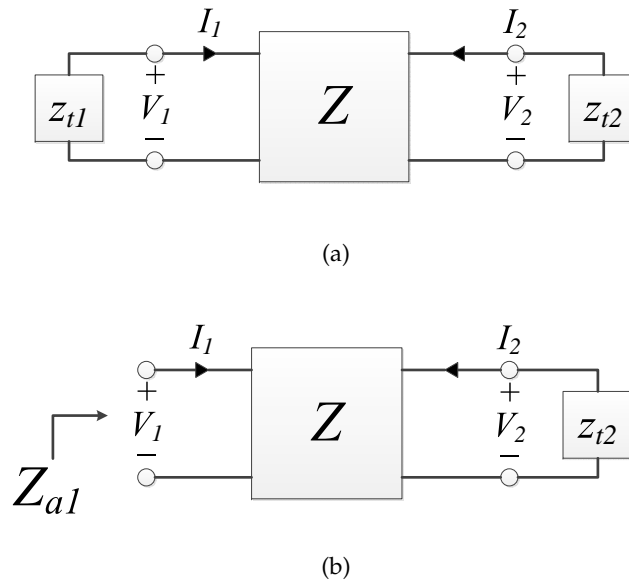
Figure 4.9: (a) A teleoperation system modelled as a two-port network. (b) The driving-point impedance $Z_{a1} = V_1/I_1$ when port 2 is terminated to a passive impedance z_{t2}.

Llewellyn's criterion is used to check absolute stability:

THEOREM 4.1: *[85] Consider a two-port network modelled by its impedance parameters as:*

Llewellyn's criterion

$$\begin{bmatrix} V_1 \\ V_2 \end{bmatrix} = \begin{bmatrix} z_{11} & z_{12} \\ z_{21} & z_{22} \end{bmatrix} \begin{bmatrix} I_1 \\ I_2 \end{bmatrix}.$$

This network is absolutely stable if and only if

1. *z_{11} and z_{22} have no poles in the right half of the complex plane,*

2. *Pure imaginary poles of z_{11} and z_{22} are simple and have positive residues, and*

3. *For all real positive frequencies ω,*

$$\operatorname{Re} z_{11}(j\omega) \geq 0$$
$$\operatorname{Re} z_{22}(j\omega) \geq 0$$
$$2\operatorname{Re} z_{11}(j\omega)\operatorname{Re} z_{22}(j\omega) - \operatorname{Re}\{z_{12}(j\omega)z_{21}(j\omega)\}$$
$$- |z_{12}(j\omega)z_{21}(j\omega)| \geq 0.$$

The two-port network impedance parameters may be replaced by any immittance parameters.

In [2], our research group has shown that Llewellyn's criterion may be extended to the case of a termination with SOP or EOP as follows:

THEOREM 4.2: *Consider a two-port network system modelled as an impedance matrix. Assume that port 2 of the two-port network is terminated to an impedance z_{t2} that satisfies $-a \leq \operatorname{Re} z_{t2}(s) \leq b$, where a and b are real numbers with $b > 0$ and $b > -a$, and that port 1 of the two-port network is terminated to another passive impedance. Then, the necessary and sufficient condition for stability of the coupled system (comprising the two-port network and two terminations) is*

Modified Llewellyn's criterion

1. *z_{11} and z_{22} have no poles in the right half of the complex plane,*

2. *Pure imaginary poles of z_{11} and z_{22} are simple and have positive residues, and*

3. *For all real positive frequencies ω,*

$$\operatorname{Re} z_{11}(j\omega) \geq 0$$
$$\operatorname{Re} z_{22}(j\omega) \geq a$$
$$2\operatorname{Re} z_{11}(j\omega)\operatorname{Re} z_{22}(j\omega) - \operatorname{Re}\{z_{12}(j\omega)z_{21}(j\omega)\}$$
$$- |z_{12}(j\omega)z_{21}(j\omega)| - 2a\operatorname{Re} z_{11}(j\omega) \geq 0.$$

The two-port network impedance parameters may be replaced by any immittance parameters. Note that a will be positive if z_{t2} has SOP and negative if it has EOP.

This theorem may be used to design a teleoperation system that will be stable even if one of its terminations—the human operator—is non-passive. Furthermore, if the human operator shows EOP, this theorem is less conservative than Llewellyn's criterion, allowing the robot controllers to be designed with higher gains to improve the system's *transparency*—the accuracy with which forces and motions of the slave robot match those of the master device. In [99], our group has shown in simulation studies that EOP values as small as $\delta = 0.9$ can yield noticeable improvements in transparency. Since the relaxed arm was found to have much larger EOP of 4.3–7.2 (Table 3.6), Theorem 4.2 can be expected to substantially improve teleoperation system transparency for times when the human operator relaxes his arm to better perceive feedback forces from the environment.

Theorem 4.2 can be used to maintain stability under SOP and improve transparency under EOP

4.6 CONCLUSIONS

Conventional approaches to analyzing the stability of a teleoperation system using passivity-based criteria or Llewellyn's criterion necessarily assume that the human operator behaves passively. The results of this chapter demonstrated that this assumption does not hold for all tasks the human operator may execute and should be explicitly evaluated for the specific task in question using a method similar to the one presented here.

Analysis of the arm's energy absorption integral indicated that non-passive behaviour can be traced to the CNS position control dynamics. Since a severely-impaired patient has little voluntarily movement control and Chapter 3 confirmed that the *relaxed* human arm is passive, it may be reasonable to model the patient's limb by a passive impedance for certain applications in telerehabilitation system design. The therapist, on the other hand, should not be assumed to be passive when she voluntarily manipulates the master device to administer therapy exercises. For 1-DOF telerehabilitation systems, the telerehabilitation system may instead be designed to satisfy the modified version of Llewellyn's criterion presented in Theorem 4.1. Another approach is to introduce passivity observers and controllers into the telerehabilitation system to maintain stability in the presence of non-passive behaviour [100]. This work demonstrates a need for research into novel approaches to teleoperation system design and stability analysis that are capable of relaxing the requirement of human operator passivity.

The patient may be passive, but the therapist is not

A VIRTUAL SENSOR FOR IMPEDANCE MEASUREMENT

The arm impedance measurement techniques previously reported in the literature (see Chapter 2) have relied on a force sensor to measure the human-robot interaction forces. The single exception is the work of Mussa-Ivaldi et al. [63], which only measured the arm's *static* stiffness; they simply *calculated* the static human-robot interaction forces from the joint torques with knowledge of the robot's kinematics. Prior work in quantifying the arm's *dynamic* impedance, however, has required a force transducer to *measure* the changing interaction forces.

Given the cost-containment pressures faced by rehabilitation clinics, the relatively high retail cost of robotic therapy and diagnostic tools has presented a barrier to their widespread clinical use [101]. Commercial multi-DOF force/torque sensors typically retail for several thousand dollars due to their intricate strain-gauge design and precise calibration (e.g., a 6-DOF force/torque sensor from ATI Industrial Automation or JR3, Inc. costs approximately 6,000 USD). Unfortunately, these sensors have not become more affordable over the past decade and no low-cost alternative technology has appeared on the horizon. According to a recent survey of therapists, a complete upper limb rehabilitation robotic system should ideally retail for no more than 6,000 USD [102]. While this target may be unrealistic in the present market for a comprehensive, multi-DOF rehabilitation robotic system, it underscores the importance of reducing the cost of this technology, especially when designing simpler, economical robotic devices for use in the patient's home. Thus, at least for the present, conventional multi-DOF force/torque sensors are not suitable for inclusion in low-cost rehabilitation robotic systems.

This chapter contributes to previous work by developing and evaluating an economical arm impedance measurement technique that does not require a *physical* force sensor. Instead, an accelerometer retailing for less than 15 USD is used to estimate interaction forces through a *virtual* sensor (or "soft sensor") derived from the

A version of this chapter has been published: M. Dyck and M. Tavakoli, "Measuring the dynamic impedance of the human arm without a force sensor," in *IEEE International Conference on Rehabilitation Robotics*, Seattle, WA, 2013.

robot's kinematics and dynamics. The data collection protocols in this chapter are similar to the sinusoidal perturbation experiments in Chapter 3. The mass-spring system was used to develop and validate the virtual sensing technique, and the method was subsequently applied to data collected from the human arm in a relaxed grasping task.

This chapter is organized as follows: Section 5.1 presents relevant mathematical formulae and introduces the experimental apparatus and data collection protocols, data analysis techniques are developed in Section 5.2, results are discussed in Section 5.3, and concluding remarks follow in Section 5.4.

5.1 METHODS AND MATERIALS

As in previous chapters, the arm's endpoint impedance is measured in two Cartesian dimensions. However, the techniques presented in this chapter can be readily extended to robots capable of performing impedance measurement in three or more DOFs.

While robot control literature provides several methods for estimating external disturbance forces in real time (see [103] and [104] for examples), these causal, observer-based techniques suffer from convergence delays. Preliminary experiments with disturbance observers revealed that the magnitude of these delays compromised impedance measurement accuracy. In the context of patient motor recovery assessment, impedance identification may be performed offline, utilizing non-causal analysis approaches for improved estimation accuracy.

5.1.1 *Mathematical Preliminaries*

When a horizontal 2-DOF revolute-joint planar robot is subjected to an externally-applied force $F_{ext} \doteq [f_x \ f_y]^T$ at its end-effector, its movement is described by the following dynamics equation[1] [105]:

$$\mathbf{I}(\Theta)\ddot{\Theta} + \mathbf{C}(\Theta,\dot{\Theta})\dot{\Theta} + F_r(\dot{\Theta}) = \tau_r + \mathbf{J}^T(\Theta)F_{ext} \tag{5.1}$$

where $\mathbf{I}(\Theta)$ is the robot's 2×2 inertia matrix, $\mathbf{C}(\Theta,\dot{\Theta})$ is the 2×2 Coriolis/centrifugal force matrix, F_r is a 2×1 friction force vector, and $\mathbf{J}^T(\Theta)$ is the robot's Jacobian transpose matrix. Vectors $\Theta \doteq [\theta_1 \ \theta_2]^T$ and $\tau_r \doteq [\tau_1 \ \tau_2]^T$ represent joint angles and torques,

---

1 Time arguments of τ_r, F_{ext}, and Θ and its derivatives are omitted to simplify notation.

respectively. With knowledge of robot kinematics and dynamics, isolating F_{ext} in this equation enables the external force to be calculated from records of the robot's motion in lieu of direct measurement by a force sensor:

$$F_{ext} = \left(\mathbf{J}^T(\Theta) \right)^{-1} \left(\tau_r - \mathbf{I}(\Theta)\ddot{\Theta} - \mathbf{C}(\Theta, \dot{\Theta})\dot{\Theta} - F_r(\dot{\Theta}) \right). \qquad (5.2)$$

Estimation of external force through robot kinematics and dynamics

Following the pattern of previous chapters, the human arm impedance was represented by the second-order Cartesian model (3.2):[2]

$$\mathbf{M}\ddot{X} + \mathbf{B}\dot{X} + \mathbf{K}\left(X - X_0\right) = -F_{ext},$$

where

$$\mathbf{M} \doteq \begin{bmatrix} m_{xx} & m_{xy} \\ m_{yx} & m_{yy} \end{bmatrix}, \ \mathbf{B} \doteq \begin{bmatrix} b_{xx} & b_{xy} \\ b_{yx} & b_{yy} \end{bmatrix}, \ \text{and } \mathbf{K} \doteq \begin{bmatrix} k_{xx} & k_{xy} \\ k_{yx} & k_{yy} \end{bmatrix},$$

denote the inertia, damping, and stiffness matrices of the human arm.[3]

The simplified version in (3.9) captures the impedance of the mass-spring system used to develop and validate the virtual sensor technique:

$$\mathbf{M}\ddot{X} + \mathbf{K}\left(X - X_0\right) = -F_{ext},$$

with

$$\mathbf{M} \doteq \begin{bmatrix} m & 0 \\ 0 & m \end{bmatrix}, \ \mathbf{K} \doteq \begin{bmatrix} k_{xx} & k_s \\ k_s & k_{yy} \end{bmatrix}.$$

5.1.2 *Experimental Protocol*

Impedance measurements were performed with the 2-DOF planar robot previously discussed, with the kinematics and dynamics presented in Appendix A. A two-axis accelerometer (ADXL-203, Analog Devices, Norwood, MA, USA) was attached at the robot's end-effector to measure Cartesian accelerations. To compare the impedance measurements from the virtual force sensor with those yielded

---

2 F_h in (3.2) is replaced in this chapter by F_{ext} for notational consistency with (5.1). Time arguments are omitted.

3 In this chapter, Cartesian positions were measured in the coordinate frame shown in Fig. 5.1, which originated at the robot's base. They could equally be expressed in a coordinate frame originating at the subject's shoulder—as was done in the previous chapters—with no loss of generality.

by a conventional force measurement approach, a commercial 6-DOF force/torque sensor (50M31A3-125 DH, JR3 Inc., Woodland, CA, USA) was also mounted on the robot's end-effector.

The impedance measurement technique was first developed and validated by measuring the impedance of the mass-spring system (Appendix D) intended to simulate a human arm with known inertia and stiffness. The technique was then applied to data collected from an actual human arm.

5.1.2.1 *Impedance Measurement for a Mass-Spring System*

The robot's end-effector was connected to an inertial payload and the planar spring array. By changing the number, stiffness, and arrangement of the springs included in the array, five different stiffness fields were obtained. For each of these spring arrangements, five different payloads were attached to the robot, creating a total of 25 unique impedance configurations. Table 5.1 lists the theoretical values of the **K** matrices (comprising k_{xx}, k_{yy}, k_s, and X_0 values calculated from independent measurements of the spring constants) and **M** matrices (comprising m values measured by weighing the payloads).

The mass-spring system was used to develop and validate the virtual sensing technique

Table 5.1: Theoretical impedance values for mass-spring system.

STIFFNESS MATRIX	STIFFNESS (N/m)			X_0 (mm)		INERTIA MATRIX	INERTIA (kg)
	k_{xx}	k_{yy}	k_s	x_0	y_0		m
$\mathbf{K_1}$	421.57	213.35	-18.87	364	-9	$\mathbf{M_1}$	0.539
$\mathbf{K_2}$	476.38	248.71	-16.02	375	-8	$\mathbf{M_2}$	0.786
$\mathbf{K_3}$	239.54	421.29	-12.52	394	53	$\mathbf{M_3}$	1.031
$\mathbf{K_4}$	190.26	406.39	-2.08	390	36	$\mathbf{M_4}$	1.279
$\mathbf{K_5}$	373.81	377.10	73.16	332	-61	$\mathbf{M_5}$	1.527

To measure the impedance of each of the 25 configurations, the robot's end-effector was perturbed about the equilibrium position of the spring array. Each of the robot's two joints was set to track a reference position comprising the sum of ten sinusoids with frequencies from 0 to 2 Hz using the proportional-derivative controller. The bandwidth of this perturbation signal was selected to match the experimental conditions under which the robot dynamic model was identified and validated and to avoid exciting a mechanical resonance in the mass-spring system at 4 to 5 Hz. (Preliminary investigations revealed that the sustained resonant vibrations excited by higher-frequency excitation signals caused the identified impe-

dance to be overestimated.) Each joint moved through an angular range of 10°, causing the robot's end-effector to remain within a circular region of 5 cm diameter. Three trials lasting 50 s each were performed for each of the 25 impedance configurations, yielding 75 trials in total.

5.1.2.2 *Impedance Measurement for the Human Arm*

For arm impedance identification, data was collected from a 23-year-old right-handed male with no history of motor impairment (Participant P1 in the previous chapters). The participant sat in front of the robot and rested his dominant hand on a hemispherical handle connected to the force sensor (Fig. 5.1). The interaction forces in this experiment were sufficiently small to allow the participant to simply rest his hand on the robot's handle without the need to forcibly grip the device and potentially alter the arm's impedance characteristics. The handle was positioned 50 cm anterior to the shoulder in the sagittal plane intersecting the shoulder joint. As in previous experiments, the participant's elbow was supported against gravity by a sling and a belt restrained the participant's torso to prevent translation of the upper body. Measurements were performed in a horizontal plane approximately 10 cm below the shoulder joint.[4] Since Chapter 3 demonstrated that the second-order Cartesian model in (3.2) could accurately capture the dynamics of the relaxed arm, the participant was instructed to relax his arm and avoid *voluntarily* exerting force while the robot perturbed his hand. This mirrored clinical protocols for evaluating muscle tone, as patients are likewise instructed to relax when assessments like the Modified Ashworth Scale (Section 2.3.7) are administered. Five trials were performed as the robot perturbed the hand in exactly the same manner as the mass-spring system.

---

4 In the experiments of previous chapters, the height of the robot was adjusted to ensure perturbations were always delivered in the horizontal plane intersecting the subject's shoulder. This controlled for variations in the arm's impedance with elevation, facilitating unbiased comparison of the impedance matrices obtained for different subjects. The equipment required to securely position the robot at different elevations was not available at the time the experiments in this chapter were performed, so the impedance measured for Participant P1 in this chapter should not be expected to match the values measured for the same subject in a different plane in Chapter 3.
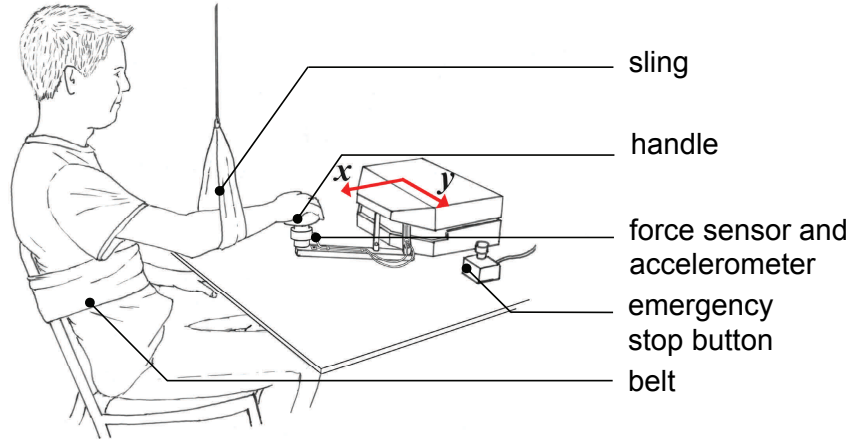
Figure 5.1: Experimental apparatus for arm impedance measurement with a virtual force sensor. The origin of the Cartesian coordinate frame is shown at the robot's base.

5.2 ANALYSIS

During the data collection experiments, the human and the position-controlled robot formed a closed-loop system with the block diagram shown in Fig. 5.2. In this diagram, Z_r and Z_h represent the impedances of the robot and the human (or the mass-spring system) respectively, and C_r is the robot's joint position controller. The endpoint of the arm (or the mass-spring system) was modelled in Cartesian space by (3.2) (or (3.8)) while the robot was modelled in joint space by (5.1). The two domains are related by the robot's forward kinematics T and Jacobian-transpose $\mathbf{J}^T$.

The robot's position controller tracks a joint-domain perturbation signal Θ_r, causing the robot to exert a torque τ_r that moves its joints to position Θ (close to Θ_r). The joint position is translated into a Cartesian end-effector position X through the robot's forward kinematics T, where the motion acts on the impedance Z_h of the human arm's endpoint to generate a reaction force $-F_{ext}$ measured by the force sensor (note that F_{ext} is defined as the force *the human exerts on the robot*). This force is translated into a joint-domain torque through the robot's Jacobian-transpose $\mathbf{J}^T$. This equivalent interaction torque together with the controller's torque output τ_r acts on the robot's admittance Z_r^{-1} to complete the closed-loop system. Since $F_{ext} = -Z_h X$, and both F_{ext} and X are measured, Z_h can be identified directly from closed-loop data according to (3.2).

If F_{ext} is not directly measured by a force sensor, the *only* other way it may be obtained is to use records of the robot's position
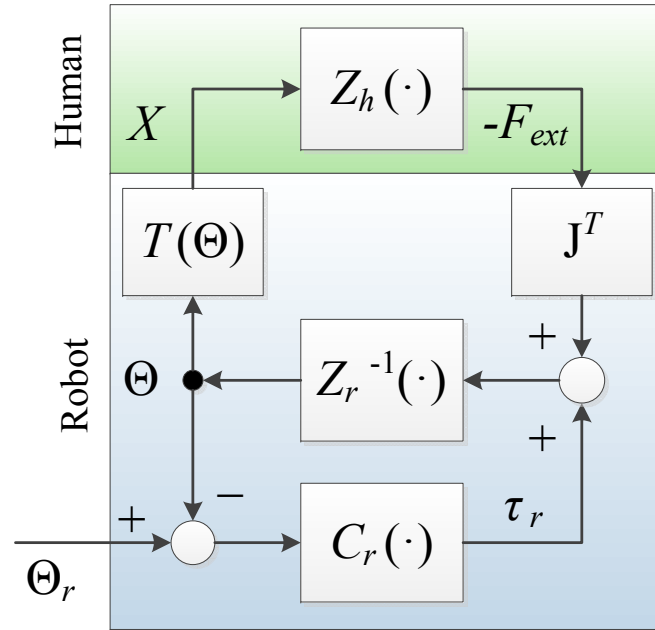
Figure 5.2: Dynamics of the impedance measurement system. The robot and the human (or the mass-spring system) impedances are $Z_r(\cdot)$ and $Z_h(\cdot)$ respectively, and $C_r(\cdot)$ represents the robot's position controller. These blocks are written as operators since they need not necessarily be modelled as LTI. The force sensor measures F_{ext}, the force exerted by the human on the robot, which may also be estimated through the robot's kinematics and dynamics.

Θ and command torque τ_r to work backwards through the robot's dynamics Z_r and calculate F_{ext} from the relation $-\mathbf{J}^T F_{ext} + \tau_r = Z_r(\Theta)$, which is equivalent to (5.2). Therefore, elimination of the force sensor comes at the cost of requiring an accurate model of robot kinematics and dynamics.

Eliminating a physical force sensor requires an accurate robot dynamic model

5.2.1 *Data Preprocessing*

Estimating arm impedance Z_h without direct measurement of F_{ext} is not trivial because the calculation of F_{ext} from (5.2) requires accurate records of $\dot{\Theta}$ and $\ddot{\Theta}$. As previously discussed in Section 3.5.1, finite-differencing and low-pass filtering of encoder data was found to be insufficiently noise-robust for this task. Instead, the accelerometer was introduced to allow direct measurement of acceleration. Furthermore, a Savitzky-Golay filter with $N = 6$ and $W = 151$ was used to remove noise from all measured signals and calculate first

An accelerometer measured accelerations; a Savitzky-Golay filter and Butterworth filter calculated velocities

time derivatives.[5] The filter's two outputs (i.e., the smoothed signal and its derivative) were passed through a zero-phase 5th-order Butterworth low-pass filter (MATLAB function `filtfilt`) with a 4.5 Hz cutoff frequency. As in Section 3.5.1, this yielded a *"smoothing filter"* and a *"differentiation filter"* that were each composed of Savitzky-Golay smoothing or differentiation and Butterworth low-pass filtering operations.

5.2.2 *Identification Methods*

Prior to identifying impedance models, all recorded signals (i.e., Θ from the joint encoders, $\ddot{X}$ from the accelerometer, F_{ext} from the force/torque sensor, and the joint torque τ_r) were passed through the smoothing filter to suppress noise. The Cartesian position trajectory of the robot's end-effector was calculated from encoder data using the robot's forward kinematics. Table 5.2 summarizes the two methods described below that were used to obtain the human-robot interaction force:

METHOD 1: VIRTUAL SENSOR   The interaction force F_{ext} was calculated from (5.2), with $\dot{\Theta}$ obtained from the differentiation filter and $\ddot{\Theta}$ calculated from the accelerometer's reading of $\ddot{X}$ according to

$$\ddot{\Theta} = \left(\mathbf{J}(\Theta)\right)^{-1} \left(\ddot{X} - \dot{\mathbf{J}}(\Theta, \dot{\Theta})\dot{\Theta}\right). \tag{5.3}$$

METHOD 2: PHYSICAL SENSOR F_{ext} was directly measured by the commercial force/torque sensor attached to robot's end-effector.

Table 5.2: Signal origins in each impedance identification method.

SIGNAL	METHOD 1 (VIRTUAL SENSOR)	METHOD 2 (PHYSICAL SENSOR)
X	Forward kinematics	Forward kinematics
$\dot{X}$	Differentiation filter	Differentiation filter
$\ddot{X}$	Accelerometer	Accelerometer
Θ	Joint encoders	Joint encoders
$\dot{\Theta}$	Differentiation filter	(Not used)
$\ddot{\Theta}$	Equation 5.3	(Not used)
τ_r	Recorded from robot controller	(Not used)
F_{ext}	Equation 5.2	Commercial force sensor

---

5 A Savitkzy-Golay filter could also be used to calculate second derivatives, eliminating the need for the accelerometer.

5.2.2.1 *Identification of Mass-Spring System Impedance*

The impedance of the mass-spring system was identified by fitting records of F_{ext}, X, and $\ddot{X}$ to (3.8) via linear least squares to obtain **M**, **K**, and X_0. A segment of typical identification data for the mass-spring system is shown in Fig. 5.3. The first 40 s of each dataset were used for identification, while the final 10 s were used to validate the identification results through the VAF test statistic in (3.10).

5.2.2.2 *Identification of Human Arm Impedance*

A handle with mass $\Lambda = 135$ g was present at the robot's end-effector during data collection for the human arm. To remove the effects of this handle from the identified inertia matrix, the human arm's inertia, damping, and stiffness matrices were identified by applying the least-squares procedure to

Effects of handle inertia must be removed

$$(\mathbf{M} + \Lambda \mathbf{I})\,\ddot{X} + \mathbf{B}\dot{X} + \mathbf{K}\,(X - X_0) = -F_{ext}, \tag{5.4}$$

where **I** is the 2×2 identity matrix. The Cartesian velocity signal $\dot{X}$ was obtained from the differentiation filter. Interaction forces were calculated by applying the same two methods used for the mass-spring system. Again, the data sets were split into identification and validation portions and the VAF was calculated.

5.3 RESULTS

The bottom row of Fig. 5.3 demonstrates that the force estimated by the virtual sensor agreed favourably with that measured by the physical sensor. This enabled the proposed virtual sensor identification approach (Method 1) to yield impedance estimates comparable to those obtained with the physical sensor (Method 2) as discussed below.

The virtual sensor estimated forces accurately
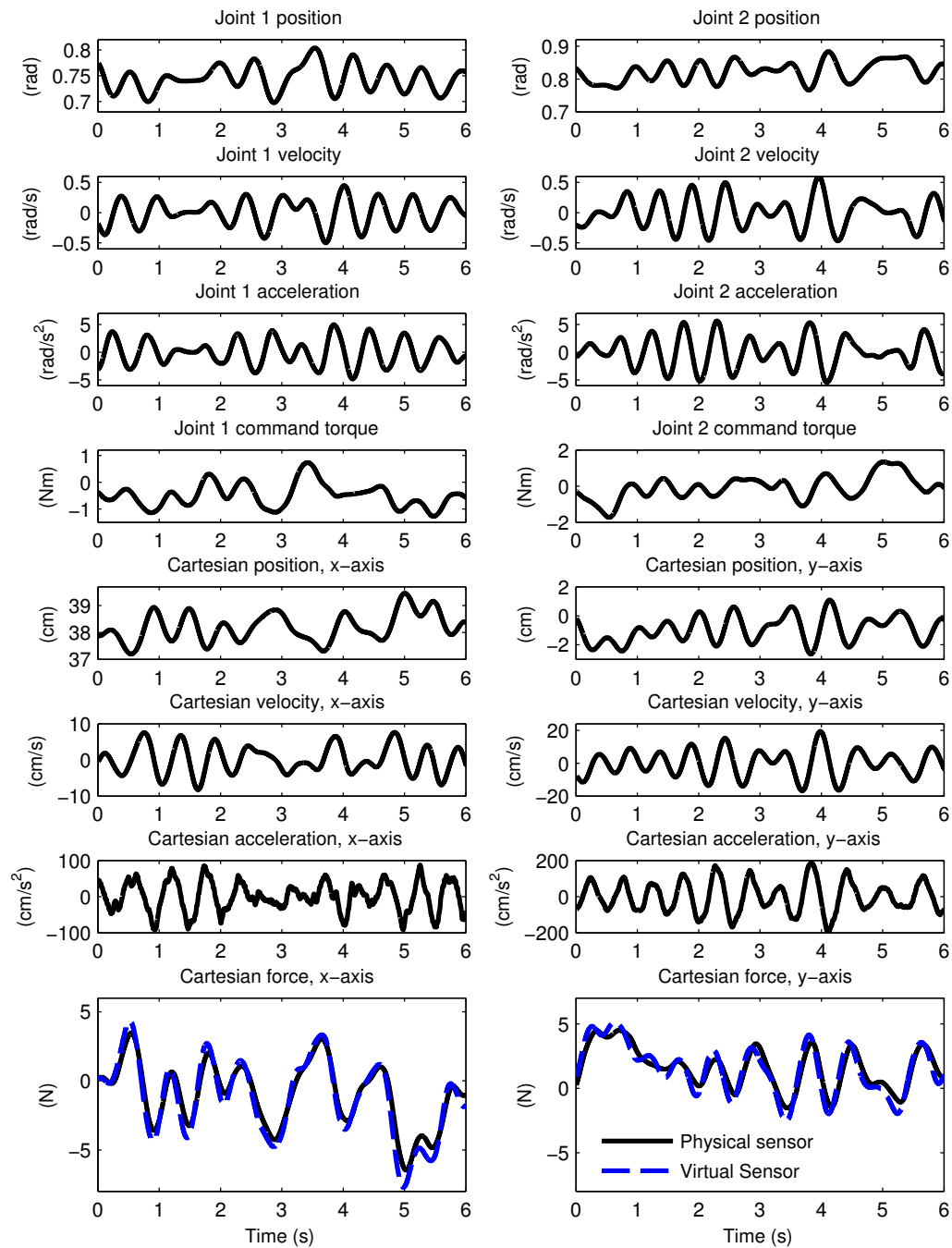
Figure 5.3: A six-second segment of typical noise-filtered identification data for the mass-spring system with $\mathbf{K_5}$ and $\mathbf{M_5}$ as given in Table 5.1. The source of each signal is listed in Table 5.2. In the bottom row, the solid line shows the Cartesian force signal by the physical sensor and the dashed line indicates the corresponding force estimate of the virtual sensor.

5.3.1 *Results for the Mass-Spring System*

Table 5.3 shows the identified mass-spring system parameters obtained by Method 1 and Method 2. To simplify the presentation, each entry represents the average and standard deviation of 15 trials. For instance, the stiffness values for K_1 are the average values obtained for the three trials performed for spring configuration K_1 with each of the five inertial payloads M_1 through M_5. Similarly, the inertia values reported for M_1 are averages of the three trials performed for M_1 under each of the five spring arrangements. Identified equilibrium positions X_0 are omitted from the table for brevity as they were always within 18 mm of theoretical values.
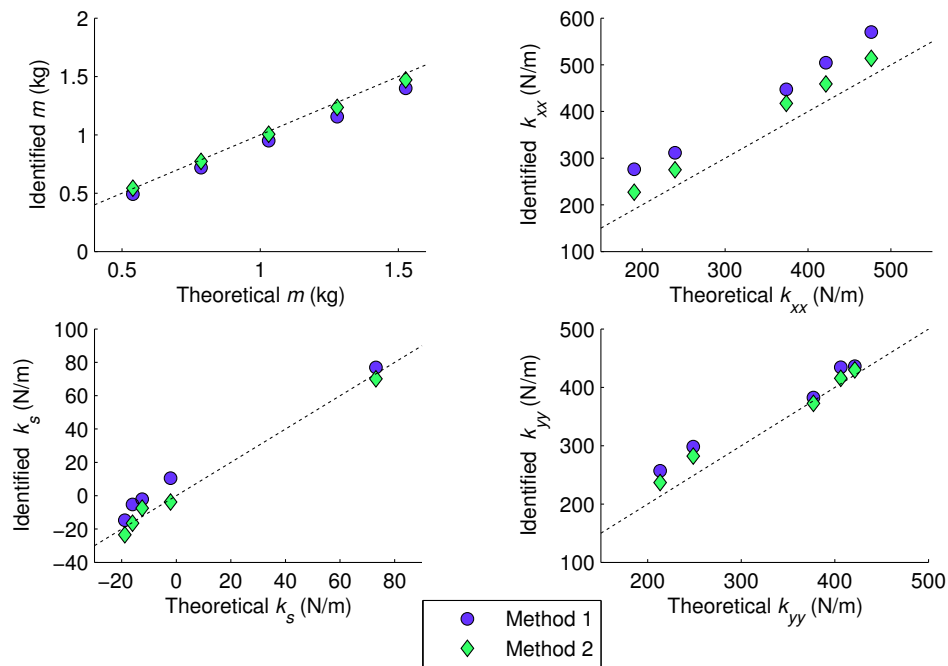
Figure 5.4: Comparison of identified and theoretical impedance parameters for the mass-spring system with sinusoidal perturbations. Data points in perfect agreement with theoretical values would lie on the dotted line.

Fig. 5.4 plots these identified parameters against their theoretical values listed in Table 5.1. This figure shows that Method 1 and Method 2 yielded parameter estimates that were comparable to each other, demonstrating the feasibility of the virtual sensor approach (Method 1) for arm impedance measurement. Furthermore, both techniques produced parameter estimates reasonably close to theoretical values. The errors between the identified and theoretical

Both methods yielded comparable impedance estimates reasonably close to theoretical values

Table 5.3: Impedance identification results for mass-spring system. Entries are averages and standard deviations from 15 trials.

IDENTIFIED STIFFNESS VALUES (N/m)

STIFFNESS MATRIX	Method 1			Method 2		
	k_{xx}	k_{yy}	k_s	k_{xx}	k_{yy}	k_s
K_1	504.43 ± 3.62	257.03 ± 6.85	-14.77 ± 4.36	458.99 ± 3.26	236.74 ± 0.86	-23.49 ± 0.42
K_2	569.98 ± 13.74	298.49 ± 6.34	-5.22 ± 3.14	514.03 ± 3.6	281.98 ± 1.79	-16.51 ± 1.39
K_3	311.49 ± 9.01	436.13 ± 2.58	-2.12 ± 1.64	275.06 ± 1.22	429.85 ± 2.54	-7.44 ± 0.96
K_4	276.37 ± 4.32	434.26 ± 4.25	10.5 ± 2.23	226.94 ± 0.91	415.37 ± 3.2	-3.84 ± 1.39
K_5	447.33 ± 9.49	382.45 ± 4.38	76.96 ± 2.69	417.24 ± 1.92	372.37 ± 1.07	70.11 ± 1.35

IDENTIFIED INERTIA VALUES (kg)

INERTIA MATRIX	Method 1	Method 2
	m	m
M_1	0.491 ± 0.042	0.544 ± 0.015
M_2	0.719 ± 0.042	0.773 ± 0.019
M_3	0.95 ± 0.034	1.005 ± 0.016
M_4	1.156 ± 0.041	1.235 ± 0.019
M_5	1.399 ± 0.036	1.471 ± 0.019

parameters are shown in Table 5.4. Each entry is calculated as the difference between the identified and theoretical values:

$$\text{error} = \text{identified value} - \text{theoretical value.}$$

Table 5.4: Error in identified impedance values for the mass-spring system. Entries are the difference between the identified parameter and the corresponding theoretical values listed in Table 5.1.

| STIFFNESS MATRIX | ERROR IN STIFFNESS VALUES (N/m) | | | | | |
| | Method 1 | | | Method 2 | | |
	k_{xx}	k_{yy}	k_s	k_{xx}	k_{yy}	k_s
$\mathbf{K_1}$	-82.86	-43.68	-4.10	-37.42	-23.39	4.62
$\mathbf{K_2}$	-93.60	-49.78	-10.80	-37.65	-33.27	0.49
$\mathbf{K_3}$	-71.95	-14.84	-10.40	-35.52	-8.56	-5.08
$\mathbf{K_4}$	-86.11	-27.87	-12.58	-36.68	-8.98	1.76
$\mathbf{K_5}$	-73.52	-5.35	-3.80	-43.43	4.73	3.05

| INERTIA MATRIX | ERROR IN INERTIA VALUES (kg) | |
| | Method 1 | Method 2 |
	m	m
$\mathbf{M_1}$	0.048	-0.005
$\mathbf{M_2}$	0.067	0.013
$\mathbf{M_3}$	0.081	0.026
$\mathbf{M_4}$	0.123	0.044
$\mathbf{M_5}$	0.128	0.056

While the agreement between the identified and theoretical inertia values was very strong, the agreement was lower for stiffness values. The discrepancy between measured and theoretical stiffness values is partially due to approximations inherent in obtaining theoretical stiffness values from empirically-determined spring constants. The springs' stiffness values were measured by fixing one end of the spring and having the robot slowly stretch the spring at the opposite end. The spring's extension was calculated from the robot's joint encoder readings and the strain gauge force sensor described in Appendix E was used to measure the force the spring exerted during the calibration procedure. This force-position data was subsequently fit to a linear model to determine the empirical spring constant. This procedure incurred some error, however, as the springs did not show a perfectly linear force-displacement re-

Sources or error in measuring stiffness

lationship for small extensions since the hooks on the end of the springs underwent deflection when the load force was initially applied.

Additional sources of error in measuring stiffness may have arisen from the system modelling approach. A two-dimensional array of ideal linear springs presents a nonlinear stiffness field (see Appendix D), so there is some linearization error incurred in modelling the stiffness by the linear model of (3.8) for small displacements. Furthermore, this model does not consider forces due to friction and damping in the springs, which also contribute to stiffness values being overestimated.

Comparing the two identification methods against each other, the virtual sensor approach yielded stiffness parameters that were slightly higher and inertia values that were slightly lower than those obtained with the physical sensor. The error values listed in Table 5.4 show that the physical sensor's estimates were closer to theoretical values. These discrepancies are the result of the limited accuracy of the robot dynamics model obtained by system identification procedures. For instance, (5.1) does not consider forces arising from bending of the robot's electrical cables, Coulomb friction, and elasticity in the robot's capstan cable drive mechanism. Equation 5.1 may therefore be augmented to include a residual error force F_{err} that accounts for any differences between the estimated robot dynamics obtained through system identification ($\hat{\mathbf{I}}(\Theta)$, $\hat{\mathbf{C}}(\Theta, \dot{\Theta})$, and $\hat{F}_r(\dot{\Theta})$) and their true values:

Parameter discrepancies are due to a residual error force seen by the virtual sensor

$$\hat{\mathbf{I}}(\Theta)\ddot{\Theta} + \hat{\mathbf{C}}(\Theta, \dot{\Theta})\dot{\Theta} + \hat{F}_r(\dot{\Theta}) = \tau_r + \mathbf{J}^T \left(F_{ext} + F_{err} \right). \quad (5.5)$$

While a force sensor can accurately measure F_{ext} directly, calculating the external force through (5.2) actually yields the sum of $F_{ext} + F_{err}$. This error in the estimated force caused Method 1 to slightly underestimate inertia and overestimate stiffness relative to Method 2. Of all the identified parameters, the relative discrepancy between Methods 1 and 2 is the largest for k_{xx}. This indicates that F_{err} contributed larger errors to the x-component of the estimated force than to the y-component—a reasonable finding since elastic forces in the force sensor and accelerometer cables caused the robot to have the highest resistance to motion along the x direction.

While the standard deviations yielded by Method 1 were larger than those obtained by Method 2, they were still very small in comparison to their corresponding mean values. This indicates that the virtual sensor identification method showed excellent intertrial reproducibility. The k values identified for each stiffness matrix did

not change as the inertial payload varied, nor did the identified inertia values change with various spring configurations. Thus, both methods could effectively distinguish impedance contributions from the spring array and the inertial payload.

With Method 2, VAF values for both the x and y components of F_{ext} were consistently over 99%, demonstrating that the identified parameters described the impedance of the mass-spring system exceptionally well. Average VAF values obtained using Method 1 for each of the twenty-five impedance configurations are recorded in Table 5.5. Method 1 always yielded models with VAF values above 83%, with the VAF being well over 92% in the vast majority of cases. This demonstrates that the proposed virtual sensor method also estimated the mass-spring system impedance with good accuracy.

High VAF values show good model fit

Table 5.5: *VAF_x, VAF_y by Method 1.*

STIFFNESS MATRIX	MAX. STIFFNESS DIRECTION	INERTIA MATRIX				
		M_1	M_2	M_3	M_4	M_5
K_1	x	97.5, 93.5	97.5, 93.1	97.5, 92.6	97.4, 92.0	97.2, 92.1
K_2	x	97.4, 95.5	97.7, 95.2	97.7, 94.9	97.5, 93.6	97.5, 94.2
K_3	y	88.7, 96.7	88.2, 96.7	87.6, 96.6	86.8, 96.6	84.9, 96.7
K_4	y	88.9, 97.1	88.2, 97.1	87.8, 97.3	83.5, 96.2	84.8, 96.9
K_5	N/A	97.4, 96.1	97.3, 95.7	97.1, 95.6	97.1, 95.4	96.9, 95.2

The VAF values obtained by Method 1 also provide insight into the design of robotic devices that are well-suited to measuring impedance without a physical force sensor. As seen from Table 5.1 and indicated in Table 5.5, the stiffness matrices K_1 and K_2 had a much higher value in the x direction than the y direction. The opposite was true for K_3 and K_4, while K_5 had $k_{xx} \approx k_{yy}$. The VAF values obtained by Method 1 were always larger for the force component in the direction of greater stiffness. This occurred because the interaction force between the robot and the spring array system was larger in the direction of higher stiffness. When F_{ext} is large, it overshadows any residual error forces contributed by inaccuracies in the robot dynamics ($F_{ext} \gg F_{err}$). Therefore, a robot intended for impedance measurement with a virtual force sensor should be designed to have low impedance (e.g., it can be a back-drivable haptic device) such that the robot's motions are dominated by the externally-applied force rather than its intrinsic dynamics. In this case, any error in the identified dynamic matrices will give rise to force contributions that are small in comparison to the force exerted

The robot should have low impedance to maximize estimation accuracy

by the human arm, enabling a highly accurate identification of the arm's impedance.

5.3.2 *Results for the Human Arm*

Parameter values and standard deviations from the five human participant trials are presented in Table 5.6. As with the mass-spring system, Methods 1 and 2 yielded very close inertia estimates. The viscosity and stiffness estimated by Method 1 were slightly larger but still close to those obtained by Method 2. VAF values are over 90% for both methods, confirming that the simple second-order model in (3.2) accurately captured the arm's dynamics for the relaxed grasping task in this chapter.

Both methods yield comparable values for the human arm

The inertia and viscosity values estimated for the human arm are comparable to those obtained in Chapter 3 (albeit in a different coordinate frame) and to the results of previous studies with similar experimental conditions by Dolan et al. [66] and Tsuji et al. [77]. The stiffness values are notably smaller, however. The high VAF values indicate that this discrepancy cannot be attributed to inaccurate identification. Of course, much of this difference is simply the result of each study collecting data from different participants whose arms have different physical properties. Furthermore, the lower apparent endpoint stiffness may be due to the low-bandwidth, slowly-varying perturbation signals used to identify arm dynamics in this work. As discussed in Appendix A, flexibility in the robot's capstan drive mechanism enabled the robot dynamics model to be accurately identified only over the frequency range of 0 to 2 Hz, and the perturbation signal used to identify the impedance of the human arm was necessarily limited to the frequencies over which the robot dynamics model was valid. Furthermore, the mass-spring system had a mechanical resonance between 4 and 5 Hz, causing excessive vibrations that compromised identification accuracy when the system was excited in this frequency range. In contrast, Dolan et al. and Tsuji et al. both applied rapidly-rising step perturbations to the arm. The effective stiffness they measured may have been higher because these perturbations excited additional high-frequency impedance dynamics in the arm. Another potential contributing factor was that, in this chapter, arm impedance was measured in a horizontal plane approximately 10 cm below the shoulder, whereas in Chapters 3 and 4 and the experiments of Dolan et al. and Tsuji et al. the arm's impedance was measured in the plane intersecting the shoulder. Indeed, Dolan found that lowering the plane of measure-

Reasons for lower stiffness values compared to previous studies

Table 5.6: Impedance identification results for the human arm (Participant P1).

IDENTIFICATION METHOD	INERTIA (kg)		VISCOSITY (Ns/m)		STIFFNESS (N/m)		X_0 (mm)	VAF
	m_{xx}	m_{xy}	b_{xx}	b_{xy}	k_{xx}	k_{xy}	x_v	VAF_x
	m_{yx}	m_{yy}	b_{yx}	b_{yy}	k_{yx}	k_{yy}	y_v	VAF_y
Method 1	1.42 ± 0.20	0.68 ± 0.09	14.26 ± 1.44	1.62 ± 0.72	90.97 ± 5.98	17.05 ± 9.82	383 ± 5	90.9
	0.69 ± 0.11	0.99 ± 0.07	1.08 ± 0.79	6.82 ± 0.75	25.92 ± 4.58	27.22 ± 4.46	15 ± 9	90.2
Method 2	1.45 ± 0.21	0.65 ± 0.09	10.88 ± 1.12	3.09 ± 0.53	72.34 ± 6.99	6.29 ± 10.14	382 ± 5	91.3
	0.68 ± 0.11	1.06 ± 0.07	2.75 ± 0.61	4.01 ± 0.51	16.12 ± 4.05	12.61 ± 3.99	8 ± 28	94.5

ment 14 mm with respect to the shoulder could cause small varia-
tions in the measured endpoint impedance [106]. Since forces from
the arm's stiffness made smaller contributions to F_{ext} in our study,
the discrepancy between Methods 1 and 2 is higher for estimates
of stiffness than for inertia or viscosity.

5.4   CONCLUSIONS AND FUTURE WORK

The results demonstrate that arm impedance can be accurately mea-
sured without a force sensor if the human-robot interaction forces
are calculated using a virtual force sensor incorporating a valid
model of the robot's kinematics and dynamics. Although this tech-
nique necessarily entails a slightly higher estimation error com-
pared to direct force measurement, it is a viable approach to add
impedance measurement functionality to existing robotic devices
without the need for potentially costly force/torque sensors. In a
telerehabilitation scenario for instance, this approach could enable
a rehabilitation therapist to remotely monitor a patient's arm impe-
dance using an economical home-based rehabilitation robot.

*The virtual sensor is
a viable technique
for economical force
sensing*

   This chapter focused on identifying a second-order Cartesian
model of human arm impedance to demonstrate the feasibility of
a virtual sensor approach for arm impedance measurement. The
model was valid only for low frequencies due to bandwidth con-
straints imposed by the robot dynamics model and mechanical res-
onances in the mass-spring system used to validate the virtual sen-
sor technique. Nevertheless, this virtual sensor technique may be
extended to analyze the arm's impedance over a larger frequency
range by applying it to a robot with a dynamic model valid at high
frequencies. As reflexive contributions to arm impedance have been
found to become significant only at frequencies above 5 Hz [94],
this could enable separate analysis of intrinsic and reflexive contri-
butions to limb impedance following a technique similar to [4] or
[107]. The virtual sensor approach could also be extended to other
robotic therapy or assessment tasks that require offline analysis of
force signals. For example, this approach could be used to mea-
sure impedance while the participant voluntarily co-contracts his
muscles, to identify more complex models of neuromusculoskele-
tal system dynamics with the aid of higher-frequency perturbation
signals, to quantify the mechanical work done during a therapy
exercise, or to administer patient strength testing.

*The virtual sensor
has numerous
potential
applications*

6

CONCLUSION

This thesis set out to develop techniques to accurately measure the mechanical impedance of the human arm within a rehabilitation context. Chapter 2 established two motivations for measuring arm impedance: (1) characterizing human-robot interaction for the design of telerehabilitation systems, and (2) overcoming the limited reliability and sensitivity of conventional observation-based clinical evaluations of muscle tone and spasticity.

6.1 IMPEDANCE MEASUREMENT FOR PASSIVITY ANALYSIS

Chapter 3 presented empirical techniques to measure the impedance of the relaxed arm. By deriving closed-form conditions that the impedance model parameters must satisfy for passivity, we showed that the relaxed arm is passive. This conclusion was confirmed by analysis of the arm's time history of energy absorption, and it agrees with the conventional assumption in teleoperation/telerehabilitation research. The chapter extended previous work in relaxed arm passivity analysis to the case of a dynamic, second-order impedance model.

Chapter 4 performed a similar analysis for a rigid grasping task. Integral analysis revealed that the CNS position control response makes the rigid arm active for underdamped perturbations with a 2 N steady-state amplitude. In contrast, the rigid arm behaved passively for sinusoidal perturbations which suppressed the position control dynamics. A one-dimensional analysis of the arm's impedance revealed that the CNS contributes non-LTI dynamics, making it challenging to identify an accurate impedance model for the rigid arm and necessitating that passivity be analyzed through the energy integral approach. This chapter demonstrated a need to revisit the passivity assumption in teleoperation control. One solution is to extend Llewellyn's absolute stability criterion to the case of a non-passive human operator.

6.2 IMPEDANCE MEASUREMENT WITH A VIRTUAL SENSOR

Chapter 5 introduced a virtual force sensor that reproduced impedance measurements obtained by a commercial force sensor with good accuracy for a fraction of the cost. This virtual sensor is a suitable technique to add impedance measurement functionality to economical robots intended for use in the patient's home. The approach could also be easily extended to other technologies that require offline analysis of human-robot interaction forces.

6.3 FUTURE WORK

The findings of this thesis lay a foundation for several future studies:

1. ENHANCED TELEOPERATION SYSTEM DESIGN. In Chapter 4, we discussed how the human operator's EOP can be used to improve transparency in teleoperation system design with a modified version of Llewellyn's criterion. Rather than simply assuming that the human operator impedance is unknown but passive, there is a need to develop new, effective approaches to teleoperation system design that are robust to non-passive operators *and* can take advantage of knowledge of the human operator impedance model to improve performance.

2. IMPEDANCE IDENTIFICATION WITH A CNS MODEL. In Chapter 4, we argued that the CNS position control dynamics play an integral role in the overall impedance characteristics of the rigid arm but cannot be accurately identified by an LTI model. The identification experiments presented in this thesis could be extended to identify nonlinear and/or time-varying models that may be able to capture the rigid arm's impedance more effectively. Such models could be useful in understanding how neural control is relearned over the course of various rehabilitation therapies.

3. EXPLOITING REACTION TIME. Fig. 4.5 indicated that a participant could not consciously respond to a perturbation during the first 100-200 ms after it was applied due to the delay introduced by his reaction time. During this interval, the CNS position control response is essentially "turned off." In another study, this delay was exploited to identify the one-dimensional impedance of a participant's hand during a motion task without the confounding effects of the CNS [97]. By

performing impedance identification on the first 100-200 ms of data immediately after the onset of a perturbation and comparing this impedance to that identified from the data thereafter, one could determine exactly how the the CNS contributions modify the arm's impedance properties.

4. JOINT-DOMAIN PASSIVITY ANALYSIS. Are the passivity characteristics of the arm different in the joint domain compared to the Cartesian domain? The answer to this question influences the design of teleoperated robotic exoskeletons, which require a joint-domain model of the human arm. If an optical tracker recorded the shoulder and elbow joint angles during our identification experiments, or if the arm's Jacobian were used to translate measured Cartesian data into the joint domain, the passivity analysis presented in this thesis could be extended to the joint domain. This could help in identifying which muscle groups tend to be responsible for passive or active behaviour under different tasks. Furthermore, it may facilitate identification of alternative joint-level impedance models that provide additional insight into motor recovery over their Cartesian counterparts. For instance, Galiana et al. [107] proposed a parallel-cascade nonlinear single-joint impedance identification approach that separately quantifies impedance contributions from the joint's intrinsic mechanics and its reflex responses. This model provides clinicians with useful insight into the recovery of reflex responses in stroke survivors.

5. MEASURING IMPEDANCE IN A FORCE CONTROL TASK. In this thesis, participants were required to either completely relax their arms or execute a position control task. These techniques could be extended to identify impedance as participants perform a force control task. The dynamics of this scenario would be similar to those shown in Fig. 4.2a with an additional CNS control loop added to adjust the human's voluntary force F_h^* based on feedback of the human-robot interaction force F_h.

6. INVESTIGATING THE RELATIONSHIP BETWEEN IMPEDANCE AND CLINICAL PATHOLOGIES. Since atypical muscle tone and spasticity both cause the limb to exhibit an abnormal relationship between force and displacement, they are related to the limb's mechanical impedance by definition. However, the precise nature of this relationship remains unclear—indeed, this may be part of the reason why the precise definition of these pathologies remains a topic of debate among clinicians.

A clinical study to thoroughly characterize the limb impedance of individuals with abnormal muscle tone and spasticity holds potential to answer questions such as:

- How are the reflex responses of spastic individuals quantitatively different from those of healthy subjects?

- How does the impedance of spastic or hypertonic individuals compare with that of healthy individuals over different frequency ranges?

- Can robotic impedance measurements be used to accurately define and diagnose the conditions of abnormal tone and spasticity?

Such a study could begin by using the rehabilitation robot to identify the impedance of another robot programmed to exhibit abnormal force-position patterns prior to extending the technique to patients [108].

7. EVALUATION OF IMPEDANCE WIDTH. Colgate and Brown proposed that the performance of a haptic device may be evaluated by its *impedance width*—the range of impedances it is able to present to the user [109]. Could a similar measure be used to assess the motor function of the human arm? The arm's impedance width could be measured by using a robot to identify impedance models for a relaxed and rigid grasping task and analyzing the mathematical distance between the two. Individuals with hypertonia or spasticity would be unable to fully relax their arms while individuals with limp muscles due to flaccid paralysis may be unable to make their arms rigid. In both scenarios, the patients' impedance width would be narrowed compared to that of healthy individuals. Compared to current clinical evaluations of arm impedance, this may prove to be a more comprehensive and insightful measure of motor ability.

BIBLIOGRAPHY

[1] M. Dyck, A. Jazayeri, and M. Tavakoli, "Is the human operator in a teleoperation system passive?" in *IEEE World Haptics Conference*, Daejeon, Korea, 2013, pp. 683–688. (Cited on page 2.)

[2] A. Jazayeri, M. Dyck, and M. Tavakoli, "Stability analysis of teleoperation systems under strictly passive and non-passive operator," in *IEEE World Haptics Conference*, Daejeon, Korea, 2013, pp. 695–700. (Cited on pages 3 and 76.)

[3] M. Dyck and M. Tavakoli, "Measuring the dynamic impedance of the human arm without a force sensor," in *IEEE International Conference on Rehabilitation Robotics*, Seattle, WA, 2013. (Cited on page 3.)

[4] E. de Vlugt, A. C. Schouten, and F. C. T. van der Helm, "Quantification of intrinsic and reflexive properties during multijoint arm posture," *Journal of Neuroscience Methods*, vol. 155, no. 2, pp. 328–349, Sep. 2006. (Cited on pages 3, 21, and 95.)

[5] D. Lawrence, "Stability and transparency in bilateral teleoperation," *IEEE Transactions on Robotics and Automation*, vol. 9, no. 5, pp. 624–637, Oct. 1993. (Cited on page 3.)

[6] N. Hogan, "Controlling impedance at the man/machine interface," in *Proceedings, 1989 International Conference on Robotics and Automation*, Scottsdale, AZ, 1989, pp. 1626–1631. (Cited on pages 3, 17, 23, 27, 46, and 48.)

[7] H. F. M. Van der Loos and D. J. Reinkensmeyer, "Rehabilitation and Health Care Robotics," in *Springer Handbook of Robotics*, B. Siciliano and O. Khatib, Eds. Berlin: Springer, 2008, pp. 1223–1251. (Cited on pages 5, 6, 7, and 14.)

[8] D. Khalili and M. Zomlefer, "An intelligent robotic system for rehabilitation of joints and estimation of body segment parameters," *IEEE Transactions on Biomedical Engineering*, vol. 35, no. 2, pp. 138–146, Feb. 1988. (Cited on page 5.)

[9] M. P. Dijkers, P. C. DeBear, R. F. Erlandson, K. Kristy, D. M. Geer, and A. Nichols, "Patient and staff acceptance of robotic

technology in occupational therapy: A pilot study," *Journal of Rehabilitation Research and Development*, vol. 28, no. 2, pp. 33–44, Mar. 1991. (Cited on page 6.)

[10] H. I. Krebs and N. Hogan, "Therapeutic robotics: A technology push," *Proceedings of the IEEE*, vol. 94, no. 9, pp. 1727–1738, Sep. 2006. (Cited on page 6.)

[11] C. Bosecker, L. Dipietro, B. Volpe, and H. I. Krebs, "Kinematic robot-based evaluation scales and clinical counterparts to measure upper limb motor performance in patients with chronic stroke," *Neurorehabilitation and Neural Repair*, vol. 24, no. 1, pp. 62–9, Jan. 2010. (Cited on pages 6, 9, 12, and 16.)

[12] H. I. Krebs, N. Hogan, M. L. Aisen, and B. T. Volpe, "Robot-aided neurorehabilitation." *IEEE Transactions on Rehabilitation Engineering*, vol. 6, no. 1, pp. 75–87, Mar. 1998. (Cited on pages 6, 12, and 14.)

[13] P. S. Lum, C. G. Burgar, and P. C. Shor, "Evidence for improved muscle activation patterns after retraining of reaching movements with the MIME robotic system in subjects with post-stroke hemiparesis." *IEEE Transactions on Neural Systems and Rehabilitation Engineering*, vol. 12, no. 2, pp. 186–194, Jun. 2004. (Cited on pages 6 and 16.)

[14] L. E. Kahn, P. S. Lum, W. Z. Rymer, and D. J. Reinkensmeyer, "Robot-assisted movement training for the stroke-impaired arm: Does it matter what the robot does?" *Journal of Rehabilitation Research and Development*, vol. 43, no. 5, pp. 619–630, Aug. 2006. (Cited on pages 6 and 15.)

[15] D. J. Reinkensmeyer, L. E. Kahn, M. Averbuch, A. McKenna-Cole, B. D. Schmit, and W. Z. Rymer, "Understanding and treating arm movement impairment after chronic brain injury: Progress with the ARM guide," *Journal of Rehabilitation Research and Development*, vol. 37, no. 6, pp. 653–662, Nov. 2000. (Cited on pages 6, 15, and 16.)

[16] G. Colombo, M. Joerg, R. Schreier, and V. Dietz, "Treadmill training of paraplegic patients using a robotic orthosis," *Journal of Rehabilitation Research and Development*, vol. 37, no. 6, pp. 693–700, Nov. 2000. (Cited on page 6.)

[17] J. Deutsch, J. Latonio, G. Burdea, and R. Boian, "Post-stroke rehabilitation with the Rutgers Ankle System: A case study,"

Presence, vol. 10, no. 4, pp. 416–430, Aug. 2001. (Cited on page 6.)

[18] L. Masia, G. Sandini, and P. G. Morasso, "A novel mechatronic system for measuring end-point stiffness: Mechanical design and preliminary tests," in *IEEE International Conference on Rehabilitation Robotics*, St. Paul, MN, 2011. (Cited on pages 6, 21, and 38.)

[19] F. Wang, M. Shastri, C. L. Jones, V. Gupta, C. Osswald, D. G. Kamper, and N. Sarkar, "Design and control of an actuated thumb exoskeleton for hand rehabilitation following stroke," in *2011 IEEE International Conference on Robotics and Automation*, Shanghai, China, 2011, pp. 3688–3693. (Cited on page 6.)

[20] K. Dautenhahn and I. Werry, "Towards interactive robots in autism therapy: Background, motivation and challenges," *Pragmatics & Cognition*, vol. 12, no. 1, pp. 1–35, Jan. 2004. (Cited on page 6.)

[21] T. Mitsui, T. Shibata, K. Wada, A. Touda, and K. Tanie, "Psychophysiological effects by interaction with mental commit robot," in *Proceedings 2001 IEEE/RSJ International Conference on Intelligent Robots and Systems*, vol. 2, Maui, HI, 2001, pp. 1189–1194. (Cited on page 6.)

[22] R. W. Teasell, N. C. Foley, K. L. Salter, and J. W. Jutai, "A blueprint for transforming stroke rehabilitation care in Canada: The case for change," *Archives of Physical Medicine and Rehabilitation*, vol. 89, no. 3, pp. 575–578, Mar. 2008. (Cited on pages 6 and 7.)

[23] F. Lowry, "Stroke rehabilitation services inadequate, experts say." *Canadian Medical Association Journal*, vol. 182, no. 7, pp. E283–284, Apr. 2010. (Cited on page 6.)

[24] G. B. Prange, M. J. A. Jannink, C. G. M. Groothuis-Oudshoorn, H. J. Hermens, and M. J. IJzerman, "Systematic review of the effect of robot-aided therapy on recovery of the hemiparetic arm after stroke," *Journal of Rehabilitation Research and Development*, vol. 43, no. 2, pp. 171–184, Mar. 2006. (Cited on page 6.)

[25] J. Hidler, D. Nichols, M. Pelliccio, and K. Brady, "Advances in the understanding and treatment of stroke impairment using robotic devices," *Topics in Stroke Rehabilitation*, vol. 12, no. 2, pp. 22–35, Jan. 2005. (Cited on pages 6 and 7.)

[26] J. Mehrholz, T. Platz, J. Kugler, and M. Pohl, "Electromechanical and robot-assisted arm training for improving arm function and activities of daily living after stroke," *Stroke*, vol. 40, pp. e392–393, Mar. 2009. (Cited on page 6.)

[27] J. L. Patton, M. E. Stoykov, M. Kovic, and F. A. Mussa-Ivaldi, "Evaluation of robotic training forces that either enhance or reduce error in chronic hemiparetic stroke survivors," *Experimental Brain Research*, vol. 168, no. 3, pp. 368–383, Jan. 2006. (Cited on page 7.)

[28] M. K. Holden, T. a. Dyar, and L. Dayan-Cimadoro, "Telerehabilitation using a virtual environment improves upper extremity function in patients with stroke," *IEEE Transactions on Neural Systems and Rehabilitation Engineering*, vol. 15, no. 1, pp. 36–42, Mar. 2007. (Cited on page 7.)

[29] C. R. Carignan and H. I. Krebs, "Telerehabilitation robotics: Bright lights, big future?" *Journal of Rehabilitation Research and Development*, vol. 43, no. 5, pp. 695–710, Aug. 2006. (Cited on page 7.)

[30] D. J. Reinkensmeyer, C. T. Pang, J. A. Nessler, and C. C. Painter, "Web-based telerehabilitation for the upper extremity after stroke," *IEEE Transactions on Neural Systems and Rehabilitation Engineering*, vol. 10, no. 2, pp. 102–108, Jun. 2002. (Cited on page 7.)

[31] G. Burdea, V. Popescu, V. Hentz, and K. Colbert, "Virtual reality-based orthopedic telerehabilitation," *IEEE Transactions on Rehabilitation Engineering*, vol. 8, no. 3, pp. 430–432, Sep. 2000. (Cited on page 7.)

[32] C. Carignan and P. Olsson, "Cooperative control of virtual objects over the Internet using force-reflecting master arms," in *Proceedings of the 2004 IEEE International Conference on Robotics and Automation*, New Orleans, LA, 2004, pp. 1221–1226. (Cited on page 8.)

[33] J. Kim, H. Kim, B. K. Tay, M. Muniyandi, M. A. Srinivasan, J. Jordan, J. Mortensen, M. Oliveira, and M. Slater, "Transatlantic touch: A study of haptic collaboration over long distance," *Presence: Teleoperators and Virtual Environments*, vol. 13, no. 3, pp. 328–337, Jun. 2004. (Cited on page 8.)

[34] S. M. McLean, M. Burton, L. Bradley, and C. Littlewood, "Interventions for enhancing adherence with physiotherapy: A systematic review," *Manual Therapy*, vol. 15, no. 6, pp. 514–521, Dec. 2010. (Cited on page 8.)

[35] S. Balasubramanian, R. Wei, R. Herman, and J. He, "Robot-measured performance metrics in stroke rehabilitation," in *ICME International Conference on Complex Medical Engineering*, Tempe, AZ, 2009. (Cited on pages 9, 14, and 15.)

[36] M. Casadio, P. Morasso, A. Noriaki Ide, V. Sanguineti, and P. Giannoni, "Measuring functional recovery of hemiparetic subjects during gentle robot therapy," *Measurement*, vol. 42, no. 8, pp. 1176–1187, Oct. 2009. (Cited on pages 9, 14, 15, and 16.)

[37] J. Sanford, J. Moreland, L. R. Swanson, P. W. Stratford, and C. Gowland, "Reliability of the Fugl-Meyer Assessment for testing motor performance in patients following stroke," *Physical Therapy*, vol. 73, no. 7, pp. 447–54, Jul. 1993. (Cited on page 10.)

[38] P. W. Duncan, L. B. Goldstein, D. Matchar, G. W. Divine, and J. Feussner, "Measurement of motor recovery after stroke: Outcome assessment and sample size requirements," *Stroke*, vol. 23, no. 8, pp. 1084–1089, Aug. 1992. (Cited on page 10.)

[39] T. Platz, C. Pinkowski, F. van Wijck, I.-H. Kim, P. di Bella, and G. Johnson, "Reliability and validity of arm function assessment with standardized guidelines for the Fugl-Meyer Test, Action Research Arm Test and Box and Block Test: A multicentre study." *Clinical Rehabilitation*, vol. 19, no. 4, pp. 404–411, Jun. 2005. (Cited on page 10.)

[40] D. J. Gladstone, C. J. Danells, and S. E. Black, "The Fugl-Meyer Assessment of motor recovery after stroke: A critical review of its measurement properties," *Neurorehabilitation and Neural Repair*, vol. 16, no. 3, pp. 232–240, Sep. 2002. (Cited on page 10.)

[41] S. S. Dittmar and G. E. Gresham, *Functional Assessment and Outcome Measures for the Rehabilitation Professional*. Gaithersburg, MD: Aspen Publishers, 1997. (Cited on pages 10 and 12.)

[42] C. Gowland, P. Stratford, M. Ward, J. Moreland, W. Torresin, S. Van Hullenaar, J. Sanford, S. Barreca, B. Vanspall, and N. Plews, "Measuring physical impairment and disability with the Chedoke-McMaster Stroke Assessment," *Stroke*, vol. 24, no. 1, pp. 58–63, Jan. 1993. (Cited on page 10.)

[43] J. H. Carr, R. B. Shepherd, L. Nordholm, and D. Lynne, "Investigation of a new motor assessment scale for stroke patients," *Physical Therapy*, vol. 65, no. 2, pp. 175–80, Feb. 1985. (Cited on page 11.)

[44] F. Malouin, L. Pichard, C. Bonneau, A. Durand, and D. Corriveau, "Evaluating motor recovery early after stroke: Comparison of the Fugl-Meyer Assessment and the Motor Assessment Scale." *Archives of Physical Medicine and Rehabilitation*, vol. 75, no. 11, pp. 1206–1212, Nov. 1994. (Cited on page 11.)

[45] S. L. Wolf, P. A. Catlin, M. Ellis, A. L. Archer, B. Morgan, and A. Piacentino, "Assessing Wolf motor function test as outcome measure for research in patients after stroke," *Stroke*, vol. 32, no. 7, pp. 1635–1639, Jul. 2001. (Cited on page 11.)

[46] D. M. Morris, G. Uswatte, J. E. Crago, E. W. Cook, and E. Taub, "The reliability of the Wolf Motor Function Test for assessing upper extremity function after stroke," *Archives of Physical Medicine and Rehabilitation*, vol. 82, no. 6, pp. 750–755, Jun. 2001. (Cited on page 11.)

[47] K. McCulloch, E. W. Cook, W. C. Fleming, T. A. Novack, and E. Taub, "A reliable test of upper extremity ADL function [abstract]," *Archives of Physical Medicine and Rehabilitation*, vol. 69, p. 755, 1988. (Cited on page 11.)

[48] B. Kopp, A. Kunkel, H. Flor, T. Platz, U. Rose, K. H. Mauritz, K. Gresser, K. L. McCulloch, and E. Taub, "The Arm Motor Ability Test: Reliability, validity, and sensitivity to change of an instrument for assessing disabilities in activities of daily living," *Archives of Physical Medicine and Rehabilitation*, vol. 78, no. 6, pp. 615–620, Jun. 1997. (Cited on page 11.)

[49] E. Mpofu and T. Oakland, *Assessment in Rehabilitation and Health*. Upper Saddle River, NJ: Pearson, 2010. (Cited on page 12.)

[50] S. Malhotra, a. D. Pandyan, C. R. Day, P. W. Jones, and H. Hermens, "Spasticity, an impairment that is poorly defined and

poorly measured," *Clinical Rehabilitation*, vol. 23, no. 7, pp. 651–658, Jul. 2009. (Cited on page 12.)

[51] P. C. Montgomery and B. H. Connolly, *Clinical Applications for Motor Control*. Thorofare, NJ: SLACK, 2003. (Cited on page 12.)

[52] J. M. Gregson, M. J. Leathley, A. P. Moore, T. L. Smith, A. K. Sharma, and C. L. Watkins, "Reliability of measurements of muscle tone and muscle power in stroke patients," *Age and Ageing*, vol. 29, no. 3, pp. 223–228, May 2000. (Cited on page 12.)

[53] R. W. Bohannon and M. B. Smith, "Interrater reliability of a modified Ashworth scale of muscle spasticity," *Physical Therapy*, vol. 67, no. 2, pp. 206–7, Feb. 1987. (Cited on pages 12 and 13.)

[54] V. M. Pomeroy, D. Dean, L. Sykes, E. B. Faragher, M. Yates, P. J. Tyrrell, S. Moss, and R. C. Tallis, "The unreliability of clinical measures of muscle tone: Implications for stroke therapy," *Age and Ageing*, vol. 29, no. 3, pp. 229–233, May 2000. (Cited on page 12.)

[55] H. I. Krebs, M. L. Aisen, B. T. Volpe, and N. Hogan, "Quantization of continuous arm movements in humans with brain injury," *Proceedings of the National Academy of Sciences of the United States of America*, vol. 96, no. 8, pp. 4645–9, Apr. 1999. (Cited on page 14.)

[56] B. Rohrer, S. Fasoli, H. I. Krebs, B. Volpe, W. R. Frontera, J. Stein, and N. Hogan, "Submovements grow larger, fewer, and more blended during stroke recovery," *Motor Control*, vol. 8, no. 4, pp. 472–483, Oct. 2004. (Cited on page 14.)

[57] J. J. Daly, N. Hogan, E. M. Perepezko, H. I. Krebs, J. M. Rogers, K. S. Goyal, M. E. Dohring, E. Fredrickson, J. Nethery, and R. L. Ruff, "Response to upper-limb robotics and functional neuromuscular stimulation following stroke," *The Journal of Rehabilitation Research and Development*, vol. 42, no. 6, pp. 723–736, Nov. 2005. (Cited on pages 14 and 15.)

[58] M. A. Finley, L. Dipietro, J. Ohlhoff, J. Whitall, H. I. Krebs, and C. T. Bever, "The effect of repeated measurements using an upper extremity robot on healthy adults," *Journal of Applied Biomechanics*, vol. 25, no. 2, pp. 103–110, May 2009. (Cited on page 15.)

[59] R. Colombo, F. Pisano, S. Micera, A. Mazzone, C. Delconte, M. C. Carrozza, P. Dario, and G. Minuco, "Assessing mechanisms of recovery during robot-aided neurorehabilitation of the upper limb," *Neurorehabilitation and Neural Repair*, vol. 22, no. 1, pp. 50–63, Jul. 2011. (Cited on pages 15 and 16.)

[60] M. F. Levin, "Interjoint coordination during pointing movements is disrupted in spastic hemiparesis," *Brain*, vol. 119, no. 1, pp. 281–293, Feb. 1996. (Cited on page 15.)

[61] R. J. van Beers, P. Haggard, and D. M. Wolpert, "The role of execution noise in movement variability," *Journal of Neurophysiology*, vol. 91, no. 2, pp. 1050–1063, Feb. 2004. (Cited on page 15.)

[62] V. Crocher, N. Jarrassé, A. Sahbani, A. Roby-Brami, and G. Morel, "Changing human upper-limb synergies with an exoskeleton using viscous fields," in *IEEE International Conference on Robotics and Automation*, Shanghai, China, 2011, pp. 4657–4663. (Cited on page 15.)

[63] F. A. Mussa-Ivaldi, N. Hogan, and E. Bizzi, "Neural, mechanical, and geometric factors subserving arm posture in humans," *Journal of Neuroscience*, vol. 5, no. 10, pp. 2732–2743, Oct. 1985. (Cited on pages 16, 20, 23, 40, 48, and 78.)

[64] H. Gomi, Y. Koike, and M. Kawato, "Human hand stiffness during discrete point-to-point multi-joint movement," in *Proceedings of the Annual International Conference of the IEEE Engineering in Medicine and Biology Society*, Paris, France, 1992, pp. 1628–1629. (Cited on pages 16, 20, and 29.)

[65] R. Shadmehr, F. A. Mussa-Ivaldi, and E. Bizzi, "Postural force fields of the human arm and their role in generating multi-joint movements," *Journal of Neuroscience*, vol. 13, no. 1, pp. 45–62, Jan. 1993. (Cited on page 16.)

[66] J. Dolan, M. Friedman, and M. Nagurka, "Dynamic and loaded impedance components in the maintenance of human arm posture," *IEEE Transactions on Systems, Man, and Cybernetics*, vol. 23, no. 3, pp. 698–709, May 1993. (Cited on pages 17, 19, 20, 26, 27, 30, 32, 40, 41, 48, and 93.)

[67] F. H. Martini, M. J. Timmons, and R. B. Tallitsch, *Human Anatomy*, 6th ed. Toronto: Pearson, 2008. (Cited on page 18.)

[68] A. M. Acosta, R. F. Kirsch, and E. J. Perreault, "A robotic manipulator for the characterization of two-dimensional dynamic stiffness using stochastic displacement perturbations," *Journal of Neuroscience Methods*, vol. 102, no. 2, pp. 177–86, Oct. 2000. (Cited on pages 18, 19, 20, and 21.)

[69] N. Hogan, "Skeletal muscle impedance in the control of motor actions," *Journal of Mechanics in Medicine and Biology*, vol. 2, no. 3-4, pp. 359–373, Sep. 2002. (Cited on page 18.)

[70] T. Tsuji, K. Goto, M. Moritani, M. Kaneko, and P. Morasso, "Spatial characteristics of human hand impedance in multi-joint arm movements," in *Proceedings of IEEE/RSJ International Conference on Intelligent Robots and Systems*, vol. 1, Munich, Germany, 1994, pp. 423–430. (Cited on page 18.)

[71] E. J. Perreault, R. F. Kirsch, and A. M. Acosta, "Multiple-input, multiple-output system identification for characterization of limb stiffness dynamics," *Biological Cybernetics*, vol. 80, no. 5, pp. 327–337, May 1999. (Cited on pages 19 and 20.)

[72] A. Roy, H. I. Krebs, S. L. Patterson, T. N. Judkins, I. Khanna, L. W. Forrester, R. M. Macko, and N. Hogan, "Measurement of human ankle stiffness using the anklebot," in *Proceedings of the 2007 IEEE 10th Conference on Rehabilitation Robotics*, Noordwijk, The Netherlands, 2007, pp. 356–363. (Cited on page 19.)

[73] E. Burdet, R. Osu, D. W. Franklin, T. E. Milner, and M. Kawato, "The central nervous system stabilizes unstable dynamics by learning optimal impedance," *Nature*, vol. 414, no. 6862, pp. 446–9, Nov. 2001. (Cited on pages 19 and 20.)

[74] A. Z. Hajian and R. D. Howe, "Identification of the mechanical impedance at the human finger tip," *Journal of Biomechanical Engineering*, vol. 119, no. 1, pp. 109–114, Feb. 1997. (Cited on pages 19 and 20.)

[75] J. J. Palazzolo, M. Ferraro, H. I. Krebs, D. Lynch, B. T. Volpe, and N. Hogan, "Stochastic estimation of arm mechanical impedance during robotic stroke rehabilitation," *IEEE Transactions on Neural Systems and Rehabilitation Engineering*, vol. 15, no. 1, pp. 94–103, Mar. 2007. (Cited on pages 19 and 20.)

[76] J. McIntyre, F. A. Mussa-Ivaldi, and E. Bizzi, "The control of stable postures in the multijoint arm," *Experimental Brain Research*, vol. 110, no. 2, pp. 248–264, Jul. 1996. (Cited on page 20.)

[77] T. Tsuji, P. G. Morasso, K. Goto, and K. Ito, "Human hand impedance characteristics during maintained posture," *Biological Cybernetics*, vol. 72, no. 6, pp. 475–485, Jan. 1995. (Cited on pages 20, 27, 41, 62, and 93.)

[78] D. J. Bennett, "Torques generated at the human elbow joint in response to constant position errors imposed during voluntary movements," *Experimental Brain Research*, vol. 95, no. 3, pp. 488–498, Aug. 1993. (Cited on page 20.)

[79] F. Lacquaniti, M. Carrozzo, and N. A. Borghese, "Time-varying mechanical behavior of multijointed arm in man," *Journal of Neurophysiology*, vol. 69, no. 5, pp. 1443–1464, May 1993. (Cited on page 20.)

[80] K. J. Kuchenbecker, J. G. Park, and G. Niemeyer, "Characterizing the human wrist for improved haptic interaction," in *2003 International Mechanical Engineering Congress and Exposition*, vol. 2003, Washington, D.C., 2003, pp. 591–598. (Cited on pages 20 and 38.)

[81] J. E. Speich, L. Shao, and M. Goldfarb, "Modeling the human hand as it interacts with a telemanipulation system," *Mechatronics*, vol. 15, no. 9, pp. 1127–1142, Nov. 2005. (Cited on page 20.)

[82] P. K. Artemiadis, P. T. Katsiaris, M. V. Liarokapis, and K. J. Kyriakopoulos, "Human arm impedance: Characterization and modeling in 3D space," in *IEEE/RSJ International Conference on Intelligent Robots and Systems*, Taipei, Taiwan, 2010, pp. 3103–3108. (Cited on page 21.)

[83] K. Park and P. H. Chang, "Stochastic estimation of human shoulder impedance with robots: An experimental design," in *IEEE International Conference on Rehabilitation Robotics*, vol. 2011, Zurich, Switzerland, 2011. (Cited on pages 21 and 38.)

[84] R. J. Anderson and M. W. Spong, "Asymptotic stability for force reflecting teleoperators with time delay," *The International Journal of Robotics Research*, vol. 11, no. 2, pp. 135–149, Apr. 1992. (Cited on page 23.)

[85] S. Haykin, *Active network theory*.   Reading, MA: Addison-Wesley, 1970. (Cited on pages 23 and 75.)

[86] R. Lozano, B. Maschke, B. Brogliato, and O. Egeland, *Dissipative Systems Analysis and Control: Theory and Applications*. London: Springer-Verlag, 2007. (Cited on page 24.)

[87] B. D. O. Anderson and S. Vongpanitlerd, *Network Analysis and Synthesis*. Englewood Cliffs, NJ: Prentice-Hall, 1973. (Cited on page 25.)

[88] H. K. Khalil, *Nonlinear Systems*, 3rd ed. Upper Saddle River, NJ: Prentice-Hall, 2002. (Cited on page 25.)

[89] H. Marquez and C. Damaren, "Analysis and synthesis of strictly positive real transfer functions," *Journal of the Franklin Institute*, vol. 333, no. 2, pp. 245–256, Mar. 1996. (Cited on page 25.)

[90] J. R. Forbes, "Extensions of Input-Output Stability Theory and the Control of Aerospace Systems," Ph.D. dissertation, University of Toronto, 2011. (Cited on page 25.)

[91] N. Hogan, "The mechanics of multi-joint posture and movement control," *Biological Cybernetics*, vol. 52, no. 5, pp. 315–331, Sep. 1985. (Cited on pages 26 and 47.)

[92] A. Savitzky and M. J. E. Golay, "Smoothing and differentiation of data by simplified least squares procedures," *Analytical Chemistry*, vol. 36, no. 8, pp. 1627–1639, Jul. 1964. (Cited on page 32.)

[93] R. Schafer, "What Is a Savitzky-Golay Filter?" *IEEE Signal Processing Magazine*, vol. 28, no. 4, pp. 111–117, Jul. 2011. (Cited on page 32.)

[94] A. C. Schouten, E. D. Vlugt, and F. C. T. van der Helm, "Design of perturbation signals for the estimation of proprioceptive reflexes," *IEEE Transactions on Biomedical Engineering*, vol. 55, no. 5, pp. 1612–1619, May 2008. (Cited on pages 38 and 95.)

[95] T. Söderström and P. Stoica, *System Identification*. New York: Prentice Hall, 1989. (Cited on pages 38 and 70.)

[96] S. L. Morris, K. J. Dodd, and M. E. Morris, "Outcomes of progressive resistance strength training following stroke: A systematic review," *Clinical Rehabilitation*, vol. 18, no. 1, pp. 27–39, Feb. 2004. (Cited on page 57.)

[97] C. Wagner and R. Howe, "Mechanisms of Performance Enhancement with Force Feedback," in *Joint Eurohaptics Conference and Symposium on Haptic Interfaces for Virtual Environment and Teleoperator Systems*, Pisa, Italy, 2005, pp. 21–29. (Cited on pages 67 and 97.)

[98] L. Ljung, "Experiments with identification of continuous time models," in *IFAC Symposium on System Identification*, Saint-Malo, France, 2009, pp. 1175–1180. (Cited on page 70.)

[99] A. Jazayeri, "Stability of bilateral teleoperation systems: Effect of sampled-data controllers and non-passivity or strict-passivity of terminations," Ph.D. dissertation, University of Alberta, 2013. (Cited on page 77.)

[100] B. Hannaford and J. Ryu, "Time-domain passivity control of haptic interfaces," *IEEE Transactions on Robotics and Automation*, vol. 18, no. 1, pp. 1–10, Feb. 2002. (Cited on page 77.)

[101] M. Lee, M. Rittenhouse, and H. A. Abdullah, "Design Issues for Therapeutic Robot Systems: Results from a Survey of Physiotherapists," *Journal of Intelligent and Robotic Systems*, vol. 42, no. 3, pp. 239–252, Mar. 2005. (Cited on page 78.)

[102] E. C. Lu, R. H. Wang, D. Hebert, J. Boger, M. P. Galea, and A. Mihailidis, "The development of an upper limb stroke rehabilitation robot: Identification of clinical practices and design requirements through a survey of therapists," *Disability and rehabilitation. Assistive technology*, vol. 6, no. 5, pp. 420–431, Jan. 2011. (Cited on page 78.)

[103] A. Radke, "A survey of state and disturbance observers for practitioners," in *Proceedings of the 2006 American Control Conference*, no. 2, Minneapolis, MN, 2006, pp. 5183–5188. (Cited on page 79.)

[104] A. Mohammadi, M. Tavakoli, H. Marquez, and F. Hashemzadeh, "Nonlinear disturbance observer design for robotic manipulators," *Control Engineering Practice*, vol. 21, no. 3, pp. 253–267, Mar. 2013. (Cited on page 79.)

[105] J. J. Craig, *Introduction to Robotics: Mechanics and Control*, 3rd ed. Upper Saddle River, NJ: Prentice Hall, 2005. (Cited on page 79.)

[106] J. Dolan, "An investigation of postural and voluntary human arm impedance control," Ph.D. dissertation, Carnegie Mellon University, 1991. (Cited on page 95.)

[107] L. Galiana, J. Fung, and R. Kearney, "Identification of intrinsic and reflex ankle stiffness components in stroke patients," *Experimental Brain Research*, vol. 165, no. 4, pp. 422–434, Sep. 2005. (Cited on pages 95 and 98.)

[108] A. Melendez-Calderon, D. Piovesan, and F. Mussa-Ivaldi, "Therapist recognition of impaired muscle groups in simulated multi-joint hypertonia," in *IEEE International Conference on Rehabilitation Robotics*, Seattle, WA, 2013. (Cited on page 99.)

[109] J. Colgate and J. Brown, "Factors affecting the Z-Width of a haptic display," in *Proceedings of the 1994 IEEE International Conference on Robotics and Automation*, San Diego, CA, 1994, pp. 3205–3210. (Cited on page 99.)

[110] M. C. Çavuşoğlu, D. Feygin, and F. Tendick, "A critical study of the mechanical and electrical properties of the PHANToM haptic interface and improvements for high performance control," *Presence: Teleoperators and Virtual Environments*, vol. 11, no. 6, pp. 555–568, Dec. 2002. (Cited on page 117.)

[111] Omega Engineering, "Force-Related Measurements," in *Transactions in Measurement and Control*. New York: Putnam, 1998, vol. 3. (Cited on page 141.)

[112] "Strain gauge configuration types," National Instruments, Austin, TX, Tech. Rep., 2006. (Cited on page 142.)

APPENDIX: ROBOT KINEMATICS AND DYNAMICS

All experiments in this thesis were performed with a 2-DOF planar upper-limb rehabilitation robot manufactured by Quanser, Inc. (Markham, ON, Canada). The robot was controlled using QUARC, Quanser's real-time control software that runs in a MATLAB and Simulink environment (The Mathworks, Natick, MA, USA). This software provided low-level access to the robot's sensors (i.e., joint encoder counts, force sensor readings, and accelerometer voltages) and facilitated sending command current to the motors in real time. This Appendix presents the robot's derived kinematics and identified dynamics.

A.1 FORWARD AND INVERSE KINEMATICS

The robot's two motors move the end effector through a capstan drive mechanism (Fig. A.1a). The *forward kinematics* relate the robot's joint angles to its end-effector position measured in the Cartesian coordinate system originating at the robot's base. From Fig. A.1b, it is straightforward to show that the forward kinematics relations are

Forward kinematics relate joint space to Cartesian space

$$x \doteq h_x(\theta_1, \theta_2) = d_1 \cos(\theta_1) + d_2 \sin(\theta_2) \qquad (A.1)$$
$$y \doteq h_y(\theta_1, \theta_2) = d_1 \sin(\theta_1) - d_2 \cos(\theta_2),$$

with link lengths $d_1 = 10''$ and $d_2 = 10.5''$.

The mechanical structure of the robot's links places the following physical limits on its joint angles:

$$-55° \leq \theta_1 \leq 90° \qquad (A.2)$$
$$0° \leq \theta_2 \leq 145°$$
$$\theta_1 - (\theta_2 - 90°) \geq 35°.$$

The first two restrictions prevent the links from colliding with the physical stops at the extremities of the capstan disc. The final restriction ensures that the links do not collide with each other. Combining these restrictions with the forward kinematics in (A.2) yields the robot's reachable Cartesian workspace, shown in Fig. A.2.
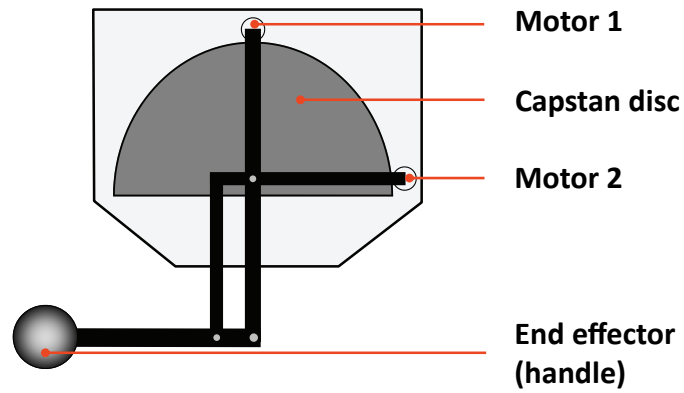
(a)
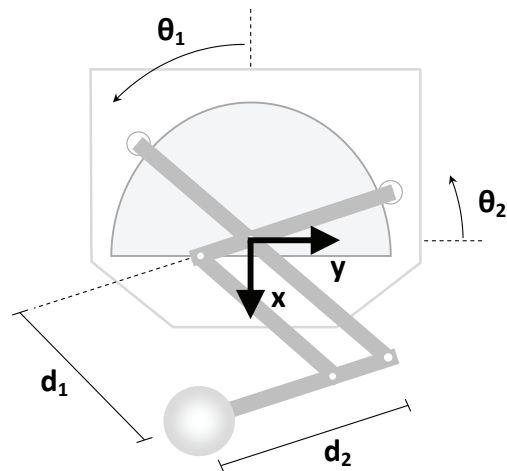
(b)

Figure A.1: The rehabilitation robot in (a) its zero joint angle position and (b) with its links displaced from the zero position. Joint angles θ_1 and θ_2 are measured relative to the dotted lines and are positive in the direction indicated. The Cartesian position of the robot's end effector is measured in the (x, y) coordinate system shown.
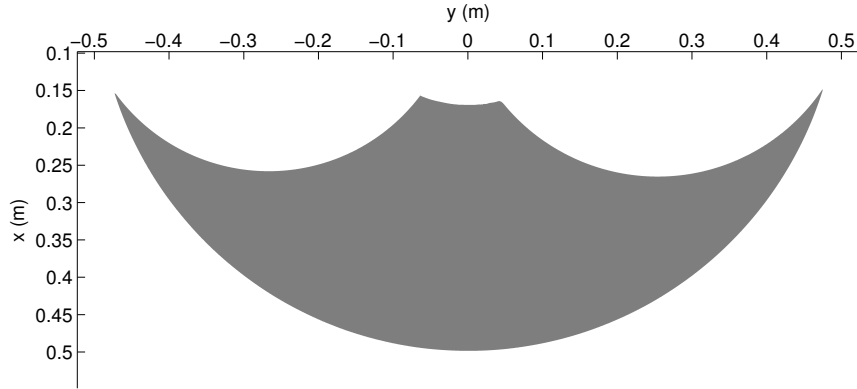
Figure A.2: The robot's reachable Cartesian workspace.

The robot's Jacobian, which translates velocities from the joint domain to the Cartesian domain, is calculated from the forward kinematics as follows:

$$\mathbf{J} \doteq \begin{bmatrix} \dfrac{\partial h_x}{\partial \theta_1} & \dfrac{\partial h_x}{\partial \theta_2} \\[2mm] \dfrac{\partial h_y}{\partial \theta_1} & \dfrac{\partial h_y}{\partial \theta_2} \end{bmatrix} = \begin{bmatrix} -d_1 \sin(\theta_1) + d_2 \cos(\theta_2) \\[1mm] d_1 \cos(\theta_1) + d_2 \sin(\theta_2) \end{bmatrix}. \tag{A.3}$$

The robot's *inverse kinematics* translate a given Cartesian position into equivalent joint angles. A closed-form inverse kinematics solution may be obtained by geometric analysis. Consider the robot positioned as in Fig. A.3. Applying the law of cosines to $\triangle ABC$, and noting that $\overline{AB} = d_1$ and $\overline{BC} = d_2$, we obtain

Inverse kinematics relate Cartesian space to joint space

$$\alpha = \text{acos}\left(\frac{d_1^2 + d_2^2 - \overline{AC}^2}{2d_1 d_2} \right)$$

$$\beta = \text{acos}\left(\frac{\overline{AC}^2 + d_1^2 - d_2^2}{2d_1 \overline{AC}} \right)$$

We can also see that

$$\gamma = \text{atan2}(y, x), \text{ and}$$
$$\overline{AC} = \sqrt{x^2 + y^2},$$

where atan2($\cdot$) denotes the four-quadrant arctangent. Since $\theta_1 = \beta + \gamma$ and $\theta_2 = \theta_1 + \alpha - 90°$, the inverse kinematic relations are:

$$\theta_1 = \text{acos}\left(\frac{x^2 + y^2 + d_1^2 - d_2^2}{2d_1\sqrt{x^2 + y^2}}\right) + \text{atan2}(y, x) \tag{A.4}$$

$$\theta_2 = \theta_1 + \text{acos}\left(\frac{d_1^2 + d_2^2 - x^2 - y^2}{2d_1 d_2}\right) - 90°.$$
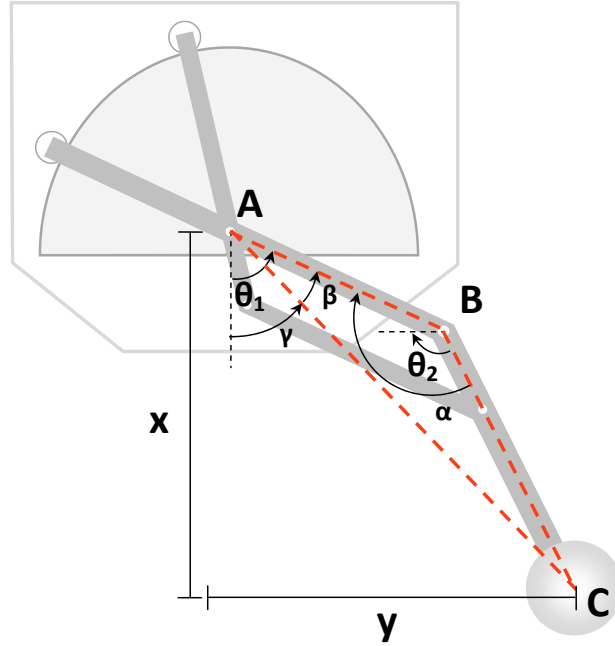
Figure A.3: Solving the robot's inverse kinematics.

A.2   ROBOT DYNAMICS

Recalling Section 5.1.1, a horizontal revolute-joint 2-DOF planar robot moving in free space has the following dynamics:

Dynamics relate motor torque to joint motion

$$\mathbf{I}(\Theta)\ddot{\Theta} + \mathbf{C}(\Theta, \dot{\Theta})\dot{\Theta} + F_r(\dot{\Theta}) = \tau_r \tag{A.5}$$

where $\mathbf{I}(\Theta)$ is the 2×2 inertia matrix, $\mathbf{C}(\Theta, \dot{\Theta})$ is the 2×2 Coriolis/centrifugal force matrix, F_r is a 2×1 friction force vector, and Θ and τ_r are 2×1 vector of joint angles and torques, respectively.

The robot's dynamic matrices are adapted from those derived for the PHANToM™ haptic device in [110]:

$$\mathbf{I}(\Theta) = \begin{bmatrix} \alpha_1 & -\frac{1}{2}\alpha_2 \sin(\theta_1 - \theta_2) \\ -\frac{1}{2}\alpha_2 \sin(\theta_1 - \theta_2) & \alpha_3 \end{bmatrix} \quad \text{(A.6)}$$

$$\mathbf{C}(\Theta, \dot{\Theta}) = \begin{bmatrix} 0 & \frac{1}{2}\alpha_2 \cos(\theta_1 - \theta_2)\dot{\theta}_2 \\ \frac{1}{2}\alpha_2 \cos(\theta_1 - \theta_2)\dot{\theta}_1 & 0 \end{bmatrix}$$

$$F_r(\dot{\Theta}) = \begin{bmatrix} \alpha_4 \dot{\theta}_1 \\ \alpha_5 \dot{\theta}_2 \end{bmatrix}$$

where α_i are constant parameters.

System identification experiments were performed to identify α_1 to α_5. Each of the robot's two joints was set to track a signal comprising ten sinusoids to move the joint through a $40°$ range such that the robot's end effector covered the majority of its workspace. The bandwidth of the perturbation signal was limited to 0 to 2 Hz as higher-frequency excitations were found to compromise identification accuracy, likely due to elasticity in the robot's capstan drive mechanism.

A Savitzky-Golay filter (see Section 3.5) with order $N = 6$ and window size $W = 151$ was used to filter encoder noise from the recorded signals Θ and τ_r and to calculate time-derivatives $\dot{\Theta}$ and $\ddot{\Theta}$. For additional noise suppression, the filtered signals and their derivatives were subsequently passed through a zero-phase 5th-order Butterworth lowpass filter (MATALB function `filtfilt`). The parameters α_i were then identified by applying linear least-squares regression to (A.5).

Six trials were performed, each lasting 50 s in duration. The first 40 s of data from each trial were used to identify parameters by linear least-squares. The identified model was validated against the final 10 s of data by applying the VAF test statistic in (3.10). The following identified parameters consistently yielded VAF values in excess of 99% for τ_1 and 90% for τ_2. Fig. A.4 compares the recorded joint torque with the joint torque predicted by the model for the same trajectory on a separate set of validation data, demonstrating that the model fits the data well.

Table A.1: Identified robot dynamic parameters with standard deviations.

Parameter	Value
α_1	0.06929 ± 0.00003
α_2	0.04217 ± 0.00007
α_3	0.04416 ± 0.00004
α_4	0.06510 ± 0.00176
α_5	0.07389 ± 0.00072
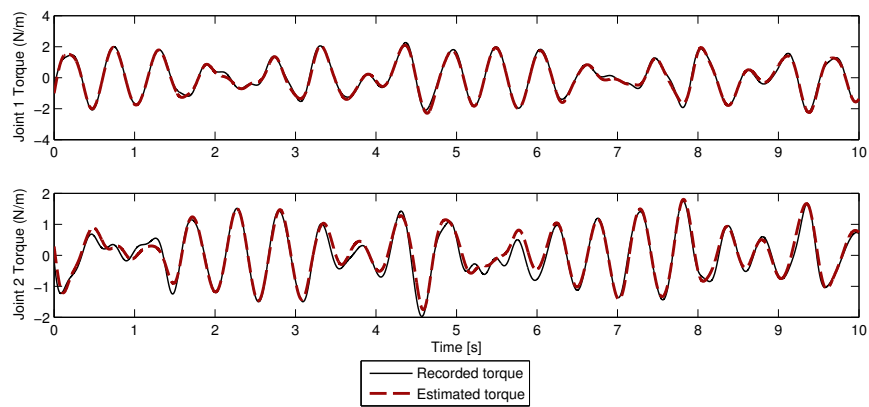
Figure A.4: Validation of robot dynamics identification. Recorded joint torque is compared against the joint torque predicted by the model for the same joint trajectory.

B

APPENDIX: PARTICIPANT INFORMATION LETTER AND CONSENT FORM

This Appendix presents the Participant Information Letter and Consent Form used to obtain informed written consent from the individuals who volunteered to participate in the study.

![University of Alberta logo]

DEPARTMENT OF ELECTRICAL AND COMPUTER ENGINEERING

Electrical and Computer Engineering Research Facility
Edmonton, Alberta, Canada T6G 2V4
Tel: 780.492.3332
Chair: 780.492.3333
Fax: 780.492.1811
www.ece.ualberta.ca

INFORMATION LETTER and CONSENT FORM

Study Title: Measuring the mechanical impedance of the upper limb using a rehabilitation robot

Research Investigator:

Matthew Dyck
M.Sc. Student
Department of Electrical and Computer Engineering
Electrical and Computer Engineering Research Facility
University of Alberta
Edmonton, AB, T6G 2V4

E: matt.dyck@ualberta.ca
T: 780.492.3368
C: ▮▮▮▮▮▮▮

Supervisor:

Dr. Mahdi Tavakoli
Assistant Professor
Department of Electrical and Computer Engineering
Electrical and Computer Engineering Research Facility
University of Alberta
Edmonton, AB, T6G 2V4

E: mahdi.tavakoli@ualberta.ca
T: 780.492.8935

Background

You have been invited to participate in a research study that aims to develop techniques to accurately measure the mechanical impedance (i.e., "stiffness") of the human arm using data collected by a rehabilitation robot. The results of this study will be included in my MSc thesis, shared at scientific conferences, and published in scientific journals. Should you choose to participate in this study, your total time commitment will be under two hours.

This research is a component of a rehabilitation robotics research program in the Telerobotic and Biorobotic Systems Group within the University of Alberta's Department Electrical and Computer Engineering. This research program is a collaboration with Edmonton's Glenrose Rehabilitation Hospital and Quanser, Inc. The work is funded by the National Sciences and Engineering Research Council of Canada and Alberta Innovates – Technology Futures, with in-kind contributions from the Glenrose Rehabilitation Hospital and Quanser, Inc.

Purpose

Individuals who have suffered stroke, spinal cord injury, or other health complications that impair movement often have irregular arm impedance compared to healthy individuals. Current techniques to measure arm impedance rely on a human expert observing a patient's motions and scoring the impedance on an established ranking system. Since these assessments are based on subjective observation, their accuracy and consistency can vary across clinicians. This creates a need for development of sensitive methods for consistent, objective evaluation of impedance to track a patient's recovery and guide the rehabilitation process.

Measuring the mechanical impedance of the upper limb using a rehabilitation robot

This study focuses on developing techniques to measure the arm impedance of healthy individuals using data collected by a robot. We intend to develop measurement techniques that will supplement traditional clinical assessments of human arm stiffness with highly sensitive, reproducible, and accurate quantitative measures. The techniques we develop will eventually be evaluated on individuals with motor impairment in a future project beyond the scope of this study.

Eligibility

To participate in this study, you must not have been diagnosed with neurological or musculoskeletal ailments that could cause your arm to have different biomechanical properties than those of healthy individuals.

Study Procedures

Part One: Background data collection (estimated time: 5 minutes)

All data collection will be completed in the Advanced Controls Laboratory (ECERF W4-050, University of Alberta).

When you arrive at the laboratory, you will be given an opportunity to review this document and ask us questions about the study. If you decide to participate, we will proceed to collect the following background data: your height, weight, dominant hand, gender, and age. This information will be used to check whether the arm impedance measurements we obtain for our participants show any trends with respect to these factors. We will also measure the length of your right forearm and upper arm, which is used in the calculation of your arm's stiffness. For this reason, **please wear short sleeves when you come to the laboratory.**

Part Two: Arm impedance measurements (estimated time: 90 minutes)

To measure your arm's impedance, you will be seated in front of the robot with your right arm resting on a forearm support attached to the robot (Fig. 1). Your arm will be secured to the forearm support with nylon safety straps, and a fabric sling suspended from the ceiling will support the weight of your arm against gravity.

In each measurement trial, the robot will gently jiggle your arm by applying a series of small position perturbations (no larger than 3 cm) or force perturbations (no larger than 8 N) to your hand. Trials will be performed with your hand positioned at different locations. In total, approximately 45 trials will be completed, each lasting from one to two minutes.

Note that slight modifications may be made to the experimental procedure based on what we learn as we analyze the data from our first few participants. For instance, we may ask you to relax your arm in some trials and hold it stiff in others. Sometimes we may ask you keep your arm in one position while the robot jiggles it, and other times we may ask you to move your hand along a path.

In addition to the force and motion data collected by the robot, we will record videos of the robot jiggling your arm using a camera mounted to the ceiling. (This video will not contain any direct facial images and no sound will be recorded.)

Measuring the mechanical impedance of the upper limb using a rehabilitation robot
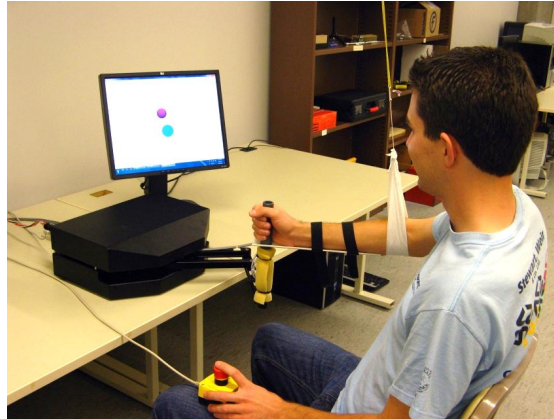
Figure 1: Experiment setup for arm impedance measurement

Benefits

Beyond the opportunity to have hands-on experience with a brand new robotic technology, there are no direct benefits available to you for participating in this study. However, we hope that this study will help the scientific community to better understand how to accurately measure the impedance of the human arm, enabling clinicians to more effectively track patients' motor recovery and design therapy programs that will help maximize motor recovery.

There are no financial costs or benefits involved in participating in this research.

Risk

We have taken every measure possible to ensure your safety and minimize any risks involved in participating in this study. However, you should be aware of the following potential risk factors:

- You may find your arm becomes tired. If this should occur, please let us know so that we can pause the data collection so that you may rest and relax your arm.
- There is always a small chance that the computer used to program the robot could crash during the experiment. This would *not* cause the robot to move in an unsafe manner.
- If appropriate safeguards had not been put in place, the robot would be capable of producing sudden motions or exerting large forces which could potentially injure your arm. However, we have taken multiple precautions to minimize the chance of this occurring:
    1. The robot's control software was programmed to ensure it interacts with humans in a gentle manner. For instance, we have implemented processes to prevent quick movements and have included safety checks to immediately turn off the robot's motors if sudden unexpected motion is detected.

Measuring the mechanical impedance of the upper limb using a rehabilitation robot

2. We have electrically restricted the robot's motors so that the robot cannot apply forces higher than 20 N, which is about the force your arm feels when you pick up a full 2 L carton of milk.
3. The robot is positioned so that your torso is outside of the area it can reach. It is also clamped to the table top to ensure it does not move out of this position.
4. Finally, you will be given an emergency stop button to hold in your left hand. Should you feel any discomfort while interacting with the device, a push of this button will instantly turn off the robot.

Voluntary Participation

Your participation in this study is completely voluntary—you are under no obligation to participate. Should you wish to opt out of the study at any point without penalty, you may do so by verbally informing us. We will not collect any additional data from you if you choose to withdraw after participating in the study. However, we may continue to use any data that we have already collected.

Confidentiality & Anonymity

After we analyze the data collected in this study, the results will be included in my MSc thesis, published in scientific journals, and shared at scientific conferences. These results will be presented in an anonymous manner so that you will not be personally identifiable. If you agree to participate in this study, we will assign you a participant number. All data that is collected—and any results we publish—will be labeled by participant number without reference to your name.

The digital data collected in this study (i.e., force and position measurements and video data) will be stored on password-protected computers in our laboratory. Hard-copy data (i.e., handwritten tables with your height, weight, age, etc.) will be stored in a locked filing cabinet in our laboratory. Only Dr. Mahdi Tavakoli, myself, and the Research Ethics Committee will have access to this raw data. We do not plan to destroy the data collected in this study as we may use it future research projects.

If you would like to receive a copy of the published research papers produced from this study, please mention your interest to us.

Further Information

If you have any further questions regarding this study, please do not hesitate to contact Matthew Dyck (work: 780-492-3368, cell: ▮▮▮▮▮▮▮▮) or Dr. Mahdi Tavakoli (work: 780-492-8935).

The plan for this study has been reviewed for its adherence to ethical guidelines by a Research Ethics Board at the University of Alberta. If you have concerns about this study or questions regarding participant rights and ethical conduct of research, please contact the Research Ethics Office at 780-492-2615. This office has no direct involvement with this project.

Measuring the mechanical impedance of the upper limb using a rehabilitation robot

Consent Statement

I have read this form and the research study has been explained to me. I have been given the opportunity to ask questions and my questions have been answered. If I have additional questions, I have been told whom to contact. I agree to participate in the research study described above. I will receive a copy of this consent form after I sign it.

_____   _____

Participant's Name (printed) and Signature   Date

_____   _____

Name (printed) and Signature of Person Obtaining Consent   Date

APPENDIX: MATLAB CODES FOR IMPEDANCE IDENTIFICATION

The following MATLAB functions were written to identify the second-order two-dimensional Cartesian impedance model from experimental data. The first code was used for sinusoidal perturbations, while the second was used for underdamped perturbations.

C.1   SINUSOIDAL PERTURBATION CODE

```matlab
function [M,B,K,X0,VAF_1,VAF_2] = sinusoidalID(logs)
% SINUSOIDALID Preprocesses arm impedance data collected with sinusoidal
% perturbations and identifies a second—order two—dimensional Cartesian
% impedance model
%    Input:
%        logs        The raw data matrix recorded by the robot. Each row
%                    corresponds to a signal as detailed under "Extract
%                    data" below.
%    Outputs:
%        M           2x2 inertia matrix
%        B           2x2 damping matrix
%        K           2x2 stiffness matrix
%        X0          2x1 equilibrium position vector
%        VAF_1       VAF for x component of force
%        VAF_2       VAF for y component of force

%% Delcare constants

T = 0.001;          % Sampling time [s]
tstart = 12;        % Data start time [s]
tsplit = 52;        % Estimation/validation split time [s]
tstop = 62;         % Data stop time [s]

% Filter parameters
N = 6;              % Order of polynomial fit for Savitzky—Golay filter
W = 101;            % Window length for Savtizky — Golay filter
fc = 5;             % Cutoff frequency for LPF

%% Extract data

time = logs(1,tstart/T:tstop/T)';    % time [s]
x    = logs(2,tstart/T:tstop/T)';       % x and y positions [m]
y    = logs(3,tstart/T:tstop/T)';
```

```matlab
34  ax   = logs(18,tstart/T:tstop/T)';    % x and y accelerometer readings ...
        [m/s^2]
35  ay   = logs(19,tstart/T:tstop/T)';
36  q1   = logs(6,tstart/T:tstop/T)';      % joint angles [rad]
37  q2   = logs(7,tstart/T:tstop/T)';
38  Fx   = logs(10,tstart/T:tstop/T)';     % x and y strain gauge reading [N]
39  Fy   = logs(11,tstart/T:tstop/T)';
40  tau1 = logs(14,tstart/T:tstop/T)';     % command torques [N/m]
41  tau2 = logs(15,tstart/T:tstop/T)';
42
43  %% Implement Savitzky—Golay filter
44
45  [~,g] = sgolay(N,W);         % see: doc sgolay
46  HalfWin  = (W+1)/2 — 1;    % half window for filtering
47  lim = length(x) — (W+1)/2; % last data point that can be processed by an ...
        S—G filter
48
49  %% Apply Savitzky—Golay filter to data
50
51  % Preallocate variables for faster execution speed. Filtered variables
52  % are denoted by a 'T' suffix. A number after a T indicates the order
53  % of the derivative.
54
55  xT    = zeros(lim,1);
56  yT    = zeros(lim,1);
57  axT   = zeros(lim,1);
58  ayT   = zeros(lim,1);
59  tau1T = zeros(lim,1);
60  tau2T = zeros(lim,1);
61  FxT   = zeros(lim,1);
62  FyT   = zeros(lim,1);
63  xT1   = zeros(lim,1);
64  yT1   = zeros(lim,1);
65  xT2   = zeros(lim,1);
66  yT2   = zeros(lim,1);
67  q1T   = zeros(lim,1);
68  q2T   = zeros(lim,1);
69  q1T1  = zeros(lim,1);
70  q2T1  = zeros(lim,1);
71  q1T2  = zeros(lim,1);
72  q2T2  = zeros(lim,1);
73
74  % Convolve data with S—G filter coefficients
75
76  for n = (W+1)/2:lim,
77      % Zero—th derivative (smoothing only)
78      xT(n)    = dot(g(:,1), x(n — HalfWin: n + HalfWin));
79      yT(n)    = dot(g(:,1), y(n — HalfWin: n + HalfWin));
80      q1T(n)   = dot(g(:,1), q1(n — HalfWin: n + HalfWin));
81      q2T(n)   = dot(g(:,1), q2(n — HalfWin: n + HalfWin));
82      axT(n)   = dot(g(:,1), ax(n — HalfWin: n + HalfWin));
83      ayT(n)   = dot(g(:,1), ay(n — HalfWin: n + HalfWin));
84      tau1T(n) = dot(g(:,1), tau1(n — HalfWin: n + HalfWin));
```

```matlab
85      tau2T(n)  = dot(g(:,1), tau2(n — HalfWin: n + HalfWin));
86      FxT(n)    = dot(g(:,1), Fx(n — HalfWin: n + HalfWin));
87      FyT(n)    = dot(g(:,1), Fy(n — HalfWin: n + HalfWin));
88      % 1st differential
89      xT1(n)    = dot(g(:,2), x(n — HalfWin: n + HalfWin));
90      yT1(n)    = dot(g(:,2), y(n — HalfWin: n + HalfWin));
91      q1T1(n)   = dot(g(:,2), q1(n — HalfWin: n + HalfWin));
92      q2T1(n)   = dot(g(:,2), q2(n — HalfWin: n + HalfWin));
93      % 2nd differential
94      xT2(n)    =  2*dot(g(:,3), x(n — HalfWin: n + HalfWin));
95      yT2(n)    =  2*dot(g(:,3), y(n — HalfWin: n + HalfWin));
96      q1T2(n)   =  2*dot(g(:,3), q1(n — HalfWin: n + HalfWin));
97      q2T2(n)   =  2*dot(g(:,3), q2(n — HalfWin: n + HalfWin));
98  end
99
100 % Convert differentials into first and second derivatives
101 xT1 = xT1/T;
102 yT1 = yT1/T;
103 xT2 = xT2/(T*T);
104 yT2 = yT2/(T*T);
105
106 q1T1 = q1T1/T;
107 q2T1 = q2T1/T;
108 q1T2 = q1T2/(T*T);
109 q2T2 = q2T2/(T*T);
110
111 % Remove initial data points which were not processed by the S—G filter
112 n = (W+1)/2+1;
113
114 xT    = xT(n:end);
115 yT    = yT(n:end);
116 q1T   = q1T(n:end);
117 q2T   = q2T(n:end);
118 axT   = axT(n:end);
119 ayT   = ayT(n:end);
120 tau1T = tau1T(n:end);
121 tau2T = tau2T(n:end);
122 FxT   = FxT(n:end);
123 FyT   = FyT(n:end);
124 xT1   = xT1(n:end);
125 yT1   = yT1(n:end);
126 q1T1  = q1T1(n:end);
127 q2T1  = q2T1(n:end);
128 xT2   = xT2(n:end);
129 yT2   = yT2(n:end);
130 q1T2  = q1T2(n:end);
131 q2T2  = q2T2(n:end);
132
133 % Truncate time vector to the same length
134 time = time(n:lim);
135
136 % LPF Savtizky—Golay filtered signals
137 [B,A] = butter(5,fc/500);        % 5th—order Butterworth filter
```

```
138
139  xT    = filtfilt(B,A,xT);         % zero-phase filtering
140  yT    = filtfilt(B,A,yT);
141  q1T   = filtfilt(B,A,q1T);
142  q2T   = filtfilt(B,A,q2T);
143  axT   = filtfilt(B,A,axT);
144  ayT   = filtfilt(B,A,ayT);
145  tau1T = filtfilt(B,A,tau1T);
146  tau2T = filtfilt(B,A,tau2T);
147  FxT   = filtfilt(B,A,FxT);
148  FyT   = filtfilt(B,A,FyT);
149  xT1   = filtfilt(B,A,xT1);
150  yT1   = filtfilt(B,A,yT1);
151  q1T1  = filtfilt(B,A,q1T1);
152  q2T1  = filtfilt(B,A,q2T1);
153  xT2   = filtfilt(B,A,xT2);
154  yT2   = filtfilt(B,A,yT2);
155  q1T2  = filtfilt(B,A,q1T2);
156  q2T2  = filtfilt(B,A,q2T2);
157
158  %% Least-squares regression
159
160  % Form output and regressor matrices
161  Force = -[FxT, FyT];
162  n = length(FxT);
163  R = [xT2 yT2 xT1 yT1 xT yT ones(n,1)];
164
165  % Split matrices in identification and validation sets
166  sp = (tsplit-tstart)/T;
167  Fid = Force(1:sp,:);
168  Rid = R(1:sp,:);
169
170  Fval = Force(sp+1:end,:);
171  Rval = R(sp+1:end,:);
172  timeval = time(sp+1:end,:);
173
174  % Identify model parameters by pseudoinverse
175  P = pinv(Rid)*Fid;
176
177  % Extract impedance matrices
178  M = P(1:2,:)';          % inertia
179  B = P(3:4,:)';          % damping
180  K = P(5:6,:)' ;         % stiffness
181  X0 = -inv(K)*P(7,:)';   % equilibrium position
182
183  %% Validate identification results
184
185  F_est = Rval*P;         % Estimated forces for validation data
186
187  % Calculate VAF values
188  VAF_1 = 100*(1-(var(Fval(:,1)-F_est(:,1))/var(Fval(:,1))));
189  VAF_2 = 100*(1-(var(Fval(:,2)-F_est(:,2))/var(Fval(:,2))));
190
```

```
191  % Plot model validation results
192  figure(1)
193  subplot(2,1,1)
194  plot(timeval,Fval(:,1),timeval,F_est(:,1))
195  title('Validation of model')
196  ylabel('Fx [N]')
197  legend('Measured Force','Model output')
198  subplot(2,1,2)
199  plot([Fval(:,2) F_est(:,2)])
200  ylabel('Fy [N]')
201  xlabel('Time [s]')
```

C.2   UNDERDAMPED PERTURBATION CODE

```
1   function [M,B,K,X0,VAF_1,VAF_2] = underdampedID(logs)
2   % UNDERDAMPEDID Preprocesses arm impedance data collected with underdamped
3   % perturbations and identifies a second—order two—dimensional Cartesian
4   % impedance model
5   %    Input:
6   %        logs        The raw data matrix recorded by the robot. Each row
7   %                    corresponds to a signal as detailed under "Extract
8   %                    data" below.
9   %    Outputs:
10  %        M           2x2 inertia matrix
11  %        B           2x2 damping matrix
12  %        K           2x2 stiffness matrix
13  %        X0          2x1 equilibrium position vector
14  %        VAF_1       VAF for x component of force
15  %        VAF_2       VAF for y component of force
16
17  %% Delcare constants
18
19  T = 0.001;          % Sampling time [s]
20  tstart = 16;        % Data start time [s]
21
22  % Filter parameters
23  N = 6;              % Order of polynomial fit for Savitzky—Golay filter
24  W = 101;            % Window length for Savtizky — Golay filter
25  fc = 5;             % Cutoff frequency for LPF
26
27
28  %% Extract data
29
30  time = logs(1,tstart/T:end)';     % time [s]
31  x    = logs(2,tstart/T:end)';     % x and y positions [m]
32  y    = logs(3,tstart/T:end)';
33  ax   = logs(18,tstart/T:end)';    % x and y accelerometer readings [m/s^2]
34  ay   = logs(19,tstart/T:end)';
35  q1   = logs(6,tstart/T:end)';     % joint angles [rad]
```

```matlab
36   q2   = logs(7,tstart/T:end)';
37   Fx   = logs(10,tstart/T:end)';      % x and y strain gauge reading [N]
38   Fy   = logs(11,tstart/T:end)';
39   tau1 = logs(14,tstart/T:end)';      % command torques [N/m]
40   tau2 = logs(15,tstart/T:end)';
41   xr   = logs(12,tstart/T:end)';      % x and y step reference signals [m]
42   yr   = logs(13,tstart/T:end)';
43
44   xr0 = xr(1);
45   yr0 = yr(1);
46
47   %% Implement Savitzky—Golay filter
48
49   [~,g] = sgolay(N,W);          % see: doc sgolay
50   HalfWin  = (W+1)/2 — 1;       % half window for filtering
51   lim = length(x) — (W+1)/2; % last data point that can be processed by an ...
        S—G filter
52
53   %% Apply Savitzky—Golay filter to data
54
55   % Preallocate variables for faster execution speed. Filtered variables
56   % are denoted by a 'T' suffix. A number after a T indicates the order
57   % of the derivative.
58
59   xT    = zeros(lim,1);
60   yT    = zeros(lim,1);
61   axT   = zeros(lim,1);
62   ayT   = zeros(lim,1);
63   tau1T = zeros(lim,1);
64   tau2T = zeros(lim,1);
65   FxT   = zeros(lim,1);
66   FyT   = zeros(lim,1);
67   xT1   = zeros(lim,1);
68   yT1   = zeros(lim,1);
69   xT2   = zeros(lim,1);
70   yT2   = zeros(lim,1);
71   q1T   = zeros(lim,1);
72   q2T   = zeros(lim,1);
73   q1T1  = zeros(lim,1);
74   q2T1  = zeros(lim,1);
75   q1T2  = zeros(lim,1);
76   q2T2  = zeros(lim,1);
77
78   % Convolve data with S—G filter coefficients
79
80   for n = (W+1)/2:lim,
81       % Zero—th derivative (smoothing only)
82       xT(n)    = dot(g(:,1), x(n — HalfWin: n + HalfWin));
83       yT(n)    = dot(g(:,1), y(n — HalfWin: n + HalfWin));
84       q1T(n)   = dot(g(:,1), q1(n — HalfWin: n + HalfWin));
85       q2T(n)   = dot(g(:,1), q2(n — HalfWin: n + HalfWin));
86       axT(n)   = dot(g(:,1), ax(n — HalfWin: n + HalfWin));
87       ayT(n)   = dot(g(:,1), ay(n — HalfWin: n + HalfWin));
```

```matlab
88      tau1T(n)  = dot(g(:,1), tau1(n — HalfWin: n + HalfWin));
89      tau2T(n)  = dot(g(:,1), tau2(n — HalfWin: n + HalfWin));
90      FxT(n)    = dot(g(:,1), Fx(n — HalfWin: n + HalfWin));
91      FyT(n)    = dot(g(:,1), Fy(n — HalfWin: n + HalfWin));
92      % 1st differential
93      xT1(n)    = dot(g(:,2), x(n — HalfWin: n + HalfWin));
94      yT1(n)    = dot(g(:,2), y(n — HalfWin: n + HalfWin));
95      q1T1(n)   = dot(g(:,2), q1(n — HalfWin: n + HalfWin));
96      q2T1(n)   = dot(g(:,2), q2(n — HalfWin: n + HalfWin));
97      % 2nd differential
98      xT2(n)    =  2*dot(g(:,3), x(n — HalfWin: n + HalfWin));
99      yT2(n)    =  2*dot(g(:,3), y(n — HalfWin: n + HalfWin));
100     q1T2(n)   =  2*dot(g(:,3), q1(n — HalfWin: n + HalfWin));
101     q2T2(n)   =  2*dot(g(:,3), q2(n — HalfWin: n + HalfWin));
102 end
103
104 % Convert differentials into first and second derivatives
105 xT1 = xT1/T;
106 yT1 = yT1/T;
107 xT2 = xT2/(T*T);
108 yT2 = yT2/(T*T);
109
110 q1T1 = q1T1/T;
111 q2T1 = q2T1/T;
112 q1T2 = q1T2/(T*T);
113 q2T2 = q2T2/(T*T);
114
115 % Remove initial data points which were not processed by the S—G filter
116 n = (W+1)/2+1;
117
118 xT    = xT(n:end);
119 yT    = yT(n:end);
120 q1T   = q1T(n:end);
121 q2T   = q2T(n:end);
122 axT   = axT(n:end);
123 ayT   = ayT(n:end);
124 tau1T = tau1T(n:end);
125 tau2T = tau2T(n:end);
126 FxT   = FxT(n:end);
127 FyT   = FyT(n:end);
128 xT1   = xT1(n:end);
129 yT1   = yT1(n:end);
130 q1T1  = q1T1(n:end);
131 q2T1  = q2T1(n:end);
132 xT2   = xT2(n:end);
133 yT2   = yT2(n:end);
134 q1T2  = q1T2(n:end);
135 q2T2  = q2T2(n:end);
136
137 % Truncate remaining vectors to the same length
138 time = time(n:lim);
139 xr   = xr(n:lim);
140 yr   = yr(n:lim);
```

```matlab
141
142  % LPF Savtizky—Golay filtered signals
143  [B,A] = butter(5,fc/500);          % 5th—order Butterworth filter
144
145  xT    = filtfilt(B,A,xT);          % zero—phase filtering
146  yT    = filtfilt(B,A,yT);
147  q1T   = filtfilt(B,A,q1T);
148  q2T   = filtfilt(B,A,q2T);
149  axT   = filtfilt(B,A,axT);
150  ayT   = filtfilt(B,A,ayT);
151  tau1T = filtfilt(B,A,tau1T);
152  tau2T = filtfilt(B,A,tau2T);
153  FxT   = filtfilt(B,A,FxT);
154  FyT   = filtfilt(B,A,FyT);
155  xT1   = filtfilt(B,A,xT1);
156  yT1   = filtfilt(B,A,yT1);
157  q1T1  = filtfilt(B,A,q1T1);
158  q2T1  = filtfilt(B,A,q2T1);
159  xT2   = filtfilt(B,A,xT2);
160  yT2   = filtfilt(B,A,yT2);
161  q1T2  = filtfilt(B,A,q1T2);
162  q2T2  = filtfilt(B,A,q2T2);
163
164  %% Calculate differential signals
165
166  % Calculate r, the magnitude of the command step perturbation signal
167  r = sqrt((xr—xr0).^2+(yr—yr0).^2);
168
169  % Normalize r such that all non—zero values are set to
170  % one.
171  r(r>0) = 1;
172
173
174  %% When does the ninth perturbation start?
175
176  % We want to use the first 8 perturbations for identification and the
177  % remaining 8 perturbations for validation. Therefore, we must identify
178  % the sample that correponds to the beginning of the 9th perturbation.
179
180  diffr = diff(r);          % diffr signal equals 1 when a perturbation
181                            % starts and —1 when a perturbation stops
182
183  diffr(diffr<0) = 0;       % set —1 values of diffr to zero
184  indices = find(diffr);    % return indices of non—zero entries of diffr
185  p9 = indices(9);          % find the 9th index
186
187  %% Separate data into estimation and validation sets
188
189  timee = time(1:p9—1);
190  FxTe  = FxT(1:p9—1);
191  FyTe  = FyT(1:p9—1);
192  xTe   = xT(1:p9—1);
193  yTe   = yT(1:p9—1);
```

```
194  xT1e  = xT1(1:p9−1);
195  yT1e  = yT1(1:p9−1);
196  xT2e  = xT2(1:p9−1);
197  yT2e  = yT2(1:p9−1);
198  re    = r(1:p9−1);
199
200  timev = time(p9:end);
201  FxTv  = FxT(p9:end);
202  FyTv  = FyT(p9:end);
203  xTv   = xT(p9:end);
204  yTv   = yT(p9:end);
205  xT1v  = xT1(p9:end);
206  yT1v  = yT1(p9:end);
207  xT2v  = xT2(p9:end);
208  yT2v  = yT2(p9:end);
209  rv    = r(p9:end);
210
211  %% Remove unwanted data points
212
213  % We only want to use data for perturbations away from the equilibrium
214  % position−−not for movements back to equilibrium or for rest periods at
215  % equilibrium. We therefore discard any samples for which the
216  % corresponding value of r is zero.
217
218  timee(re==0) = [];
219  FxTe(re==0) = [];
220  FyTe(re==0) = [];
221  xTe(re==0) = [];
222  yTe(re==0) = [];
223  xT1e(re==0) = [];
224  yT1e(re==0) = [];
225  xT2e(re==0) = [];
226  yT2e(re==0) = [];
227
228  timev(rv==0) = [];
229  FxTv(rv==0) = [];
230  FyTv(rv==0) = [];
231  xTv(rv==0) = [];
232  yTv(rv==0) = [];
233  xT1v(rv==0) = [];
234  yT1v(rv==0) = [];
235  xT2v(rv==0) = [];
236  yT2v(rv==0) = [];
237
238  %% Least−squares regression
239
240  % Form output and regressor matrices
241  Fe = −[FxTe, FyTe];
242  n = length(FxTe);
243  Re = [xT2e yT2e xT1e yT1e xTe yTe ones(n,1)];
244
245  % Identify model parameters by pseudoinverse
246  P = pinv(Re)*Fe;
```

```matlab
247
248 % Extract impedance matrices
249 M = P(1:2,:)';              % inertia
250 B = P(3:4,:)';              % damping
251 K = P(5:6,:)' ;             % stiffness
252 X0 = -inv(K)*P(7,:)';       % equilibrium position
253
254 %% Validate identification results
255
256 n = length(FxTv);
257 Rv = [xT2v yT2v xT1v yT1v xTv yTv ones(n,1)];
258
259 FxTest = -Rv*P(:,1);        % Estimated forces for validation data
260 FyTest = -Rv*P(:,2);
261
262 % Calculate VAF values
263 VAF_1 = 100*(1-var(FxTv-FxTest)/var(FxTv));
264 VAF_2 = 100*(1-var(FyTv-FyTest)/var(FyTv));
265
266 % Plot model validation results
267 figure
268 subplot(2,1,1)
269 plot([FxTv FxTest])
270 title('Validation of model')
271 ylabel('Fx [N]')
272 legend('Measured Force','Model output')
273 subplot(2,1,2)
274 plot([FyTv FyTest])
275 ylabel('Fy [N]')
276 xlabel('Time [s]')
```

D

APPENDIX: DESIGN OF SPRING ARRAY

The impedance identification techniques presented in this thesis were validated against known inertial and stiffness fields from end-effector payloads and a two-dimensional spring array. This Appendix details the design of the spring array and the calculation of its theoretical stiffness fields.

D.1 SPRING ARRAY CONSTRUCTION

The spring array consisted of a $15.5'' \times 15.5''$ plywood frame suspended above a $21'' \times 31''$ plywood base by four posts made of $\frac{1}{2}''$ threaded rod (Fig. D.1). The rods allowed the frame's height to be adjusted for various force sensors that were connected to the robot's end effector. Eight screw eyes were affixed to the corners and sides of the frame to provide attachment points for extension springs. The frame was designed to be sufficiently large such that the springs would always remain in tension as the robot perturbed the system. An aluminium disc with eight holes spaced at $45°$ intervals on a circle 2.25 cm in diameter was affixed to the robot's end effector to allow the springs to be connected to the robot (Fig. D.2).

D.2 CALCULATION OF STIFFNESS FIELD

Different stiffness fields were obtained by varying the number, stiffness, and locations of the springs in the array. For each combination of springs, the theoretical stiffness was calculated as follows.

Consider an array of n linear springs connected to the robot's end effector. Let the ith spring have stiffness k_i and relaxed length ℓ_i, and let it be attached to the spring array frame at location $R_i \doteq [x_i \; y_i]^T$. Then, the total external force $F_{ext} \doteq [f_x \; f_y]^T$ applied to the robot's end effector when it is at position $R \doteq [x \; y]^T$ is

$$
\begin{aligned}
F_{ext}(R) &= -\sum_{i=1}^{n} k_i \left(|R - R_i| - \ell_i \right) \frac{R - R_i}{|R - R_i|} \\
&= -\sum_{i=1}^{n} k_i \left(1 - \frac{\ell_i}{\sqrt{(x - x_i)^2 + (y - y_i)^2}} \right) \begin{bmatrix} x - x_i \\ y - y_i \end{bmatrix}
\end{aligned}
\tag{D.1}
$$

135
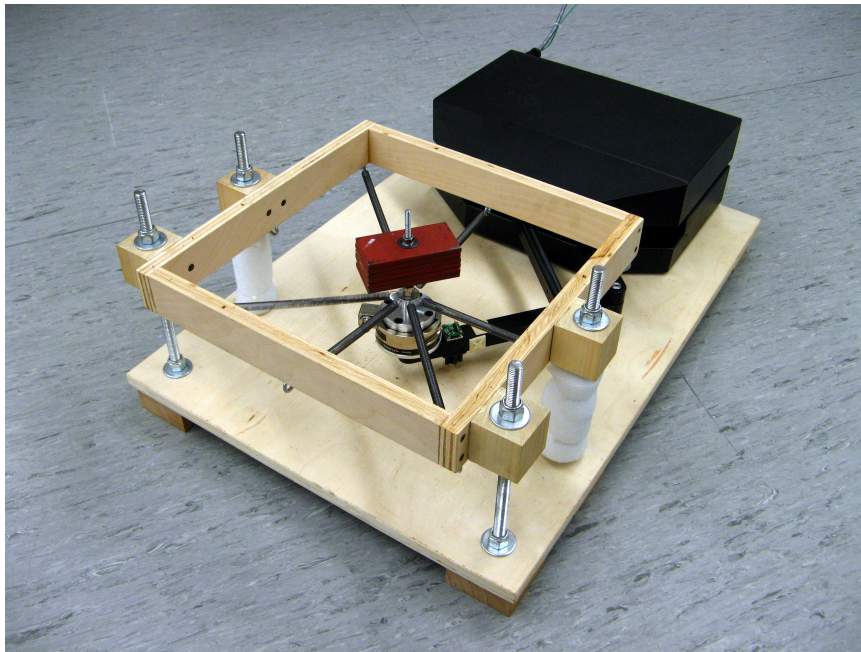
Figure D.1: Photograph of robot connected to the spring array.
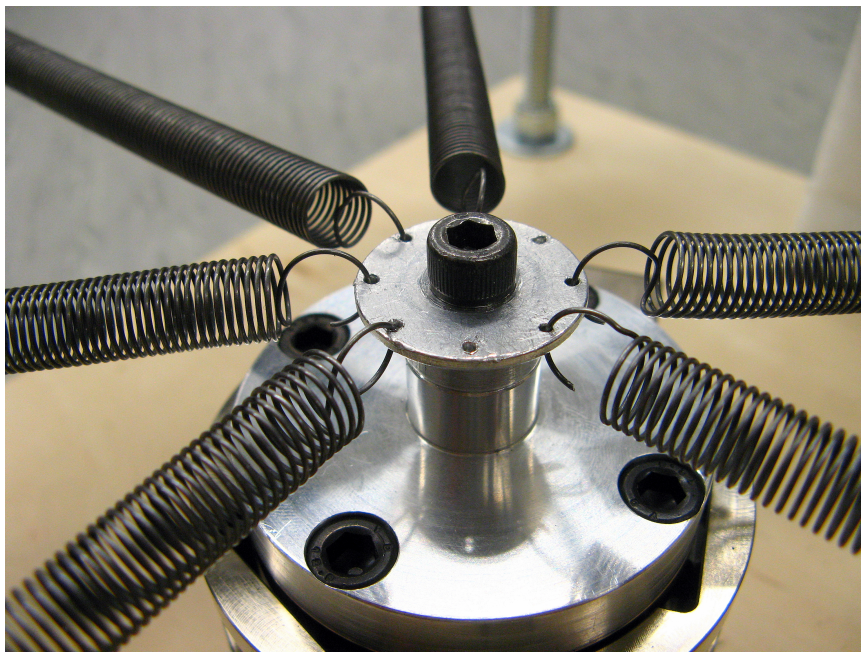
Figure D.2: Close-up photograph of disc used to connect springs to the robot's end effector.

This is a nonlinear function of x and y. For small displacements about the equilibrium position of the spring array, (D.1) may be expanded as a Taylor series about the equilibrium position R_0 of the spring array:

$$F_{ext}(R) = F_{ext}(R_0) + \nabla F \begin{bmatrix} \delta x \\ \delta y \end{bmatrix} + \dots \tag{D.2}$$

where $\delta x \doteq x - x_0$ and $\delta y \doteq y - y_0$. Since the spring array exerts no net force on the robot at its equilibrium position, $F_{ext}(R_0)$ is zero. Hence, for small displacements, $F_{ext}(\delta R) = \mathbf{K}\,\delta R$, where $\mathbf{K}$ is given by the gradient of $F_{ext}(R)$:

$$\mathbf{K} = \begin{bmatrix} \dfrac{\partial f_x}{\partial x} & \dfrac{\partial f_x}{\partial y} \\ \dfrac{\partial f_x}{\partial y} & \dfrac{\partial f_y}{\partial y} \end{bmatrix}. \tag{D.3}$$

For each spring configuration, the theoretical value of $\mathbf{K}$ was calculated in MATLAB by evaluating (D.1) in a region about the equilibrium point of the spring configuration and numerically calculating the gradient of F_{ext} at the equilibrium point. The code is provided on the following page.

The stiffness is approximately linear for small perturbations

```matlab
1  function [K,X] = fxystiffness(kp,lp)
2  % FXYSTIFFNESS  Calculate stiffness matrix and equilibrium position
3  %                    for a given configuration of springs in the spring array.
4  %
5  %    K = fxystiffness(kp,lp) computes the stiffness matrix at the
6  %    equilibrium point of a spring array defined by vectors kp and lp.
7  %
8  %    kp = [k1 k2 k3 k4 k5 k6 k7 k8]' is a vector of spring constants (N/m)
9  %    lp = [l1 l2 l3 l4 l5 l6 l7 l8]' is a corresponding vector of relaxed
10 %                                      spring lengths (m)
11 %
12 %    The labelling convention and coordinate system is shown below:
13 %
14 %                        d1
15 %                   |———————|
16 %
17 %              k1          k2          k3
18 %         ——        +——————————————+
19 %          |        |                |
20 %     d2   |        |                |
21 %          |        |                |
22 %         —— k8     |        + origin | k4     Robot's Cartesian coordinates:
23 %          |        |                |         |———> +y
24 %          |        |                |         |
25 %          |        |                |         |
26 %         +————————————————+         v
27 %              k7          k6          k5     +x
28 %
29 % If fewer than eight springs are connected, set the spring constant
30 % for any ommitted springs to zero in kp. Leave the corresponding
31 % lengths in lp as arbitrary non—zero values to avoid a division by zero
32 % error.
33 %
34 % Assumptions:
35 %    Springs are always in tension
36 %    Springs are linear (F = —kx) throughout the workspace
37 %    The frame is perfectly rectangular
38
39 %% Declare constants
40
41 d1 = 0.183; d2 = 0.175;  % frame dimensions [m] (see diagram above)
42 h = 0.00015;             % grid spacing [m]
43 ri = [—d2 —d1;           % vector of attachement points (x,y) for k1 — k8
44        —d2  0;
45        —d2  d1;
46         0   d1;
47        d2   d1;
48        d2   0;
49        d2  —d1;
50         0  —d1;];
51
52 %% Calculate spring force
```

```matlab
53
54   % The meshgrid command is used to generate a grid of points (r values) for
55   % calculating the spring force. Note that the grid is only generated over
56   % a small portion of the frame's area to ensure springs are always in
57   % tension. The meshgrid command produces a dy matrix whose values increase
58   % from left to right and a dx matrix whose values increase from top to
59   % bottom to parallel the coordinate system defined in the diagram above.
60   [dy,dx] = meshgrid(-d1/3:h:d1/3,-d2/3:h:d2/3);
61
62   % Cycle through all points in the grid and calculate the total force the
63   % spring array applies at each point.
64
65   [limx,limy] = size(dx);
66   Fx = zeros(limx,limy);       % initialize x-component of force
67   Fy = zeros(limx,limy);       % initialize y-component of force
68
69   for i = 1:limx               % for each position along the x axis
70       for j = 1:limy           % for each position along the y axis
71           for k = 1:8          % for each spring
72               % Calculate r - ri
73               p = [dx(i,j)-  ri(k,1) ;
74                    dy(i,j) - ri(k,2)];
75               % Add force contribution from the current (i.e. k^th) spring
76               % to Fx and Fy
77               Fx(i,j) = Fx(i,j) - kp(k)*(1-lp(k)/norm(p))*p(1);
78               Fy(i,j) = Fy(i,j) - kp(k)*(1-lp(k)/norm(p))*p(2);
79           end
80       end
81   end
82
83   %% Calculate stiffness fields
84
85   % The stiffnes matrix elements are obtained from the gradients of Fx and
86   % Fy. A negative sign is added since F = -k*x.
87   [kxy,kxx] = gradient(-Fx,h);
88   [kyy,kyx] = gradient(-Fy,h);
89
90   F = sqrt(Fx.^2+Fy.^2);   % total force magnitude
91
92   % Find the equilibrium location where force is a minimum. First, use the
93   % min function to search the columns of F, then use min again to search
94   % the resulting row vector (yminF) and find the minimum value (minF).
95   % xminI and yminI are the indices of the equilibrium point; xminL and
96   % yminL are the cooresponding Cartesian coordinates.
97   [yminF, xminI] = min(F);
98   [minF, yminI] = min(yminF);
99   xminI = xminI(yminI);
100  xminL = dx(xminI,yminI);
101  yminL = dy(xminI,yminI);
102
103  % So the equilibrium position is...
104  X = [xminL yminL];
105
```

```
106  % The stiffness matrix is given by the values of the stiffness elements
107  % at the equilibrium point.
108  Kxx = kxx(xminI,yminI);
109  Kxy = kxy(xminI,yminI);
110  Kyx = kyx(xminI,yminI);
111  Kyy = kyy(xminI,yminI);
112
113  % So the stiffness matrix is...
114  K  = [ Kxx Kxy;
115         Kyx Kyy];
```

APPENDIX: DESIGN OF STRAIN GAUGE SENSOR

A strain gauge sensor was designed, fabricated, and calibrated to measure human-robot interaction forces. This 2-DOF sensor was initially conceived as an inexpensive alternative to a commercial load cell. (Refer to Chapter 5 for a discussion of economic drawbacks of using commercial load cells with rehabilitation robots.)

The sensor used a bending beam sensing element. While this design facilitates straightforward and inexpensive fabrication, it functions as a *torque sensor* rather than a *force sensor*—the sensor's voltage output scales both with the applied force and the lever arm length between the strain gauges and the point where the force is applied. The sensor was used during preliminary experiments with the spring array, where the point of application of spring forces was constant and could be accounted for in the sensor calibration. However, the sensor was not suitable for measuring forces during human subject trials. The subject's hand applied forces with an unknown distribution over the length of a handle attached to the cantilever beam, rendering it impossible to properly account for the distance between the strain gauges and the point of force application.

The lever arm length between the strain gauges and applied force must be known for proper calibration

All measured force signals reported in this thesis were therefore recorded with a commercial 6-DOF load cell capable of distinguishing between forces and torques. However, the design of the strain gauge sensor is included here as a reference for future sensor development research.

E.1 OPERATION PRINCIPLE

A bonded resistance strain gauge consists of a resistive wire filament (approximately 0.025 mm thick [111]) directly bonded to the strained surface by a thin layer of epoxy resin. When the surface is deflected from the strain caused by an applied force, the filament is stretched (compressed), causing its resistance to increase (decrease). This change in resistance is proportional to the force exerted on the surface.

Force causes resistance change

The Wheatstone bridge circuit provides an effective means of sensing this resistive change. Fig. E.1 shows a Wheatstone bridge configuration to measure the bending strain in a cantilever beam. If

The Wheastone bridge senses resistance change

no strain is applied to the gauges, the bridge is perfectly balanced and V_{out} in Fig. E.1b is zero. When a force is applied to a cantilever beam as shown in Fig. E.1a, gauges 1 and 3 are stretched causing an increased resistance, while gauges 2 and 4 are compressed and their resistance decreases. This creates an imbalance in the bridge, such that V_{out} becomes positive.

A full-bridge circuit comprises four identical strain gauges. In partial-bridge circuits, some of these strain gauges may be replaced by resistors of the equal resistance. However, the full bridge provides the advantages of higher sensitivity, compensation against temperature drift, and rejection of axial strain [112].
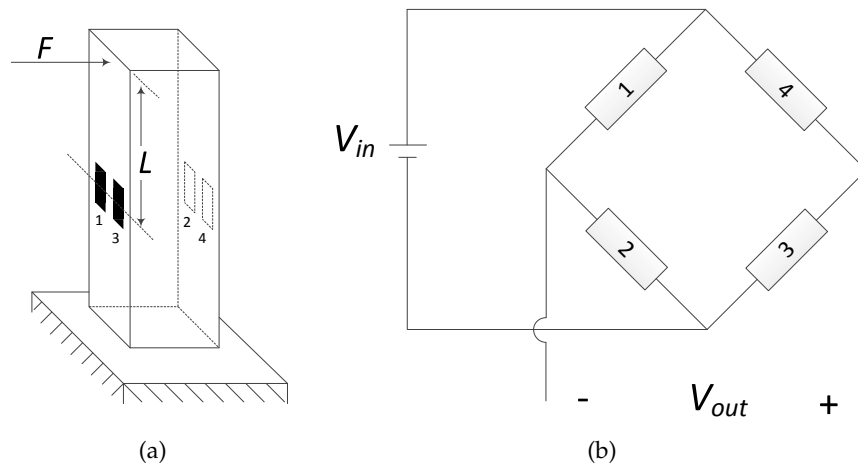
Figure E.1: A single DOF bending-beam load cell based on the Wheatstone bridge. (a) Positions of four strain gauges to measure bending force applied to the cantilever beam. (b) The corresponding full Wheatstone bridge circuit.

In the configuration of Fig. E.1, V_{out} is linearly proportional to the bending strain ϵ_B. The bending strain at a given point in the beam is related to the applied force by the equation

$$\epsilon_B = \frac{M_B}{ZE} = \frac{F \times L}{ZE},$$ (E.1)

where Z is the beam's section modulus (a property of the beam's cross section), E is Young's Modulus of Elasticity (a property of the beam's material), and $M_B = F \times L$ is the bending moment. Hence, if the lever arm length L between the strain gauges and the point of application of the force is known, the gauges may be used to measure F directly. If this distance is unknown, one can only isolate the total bending moment, M_B.

Strain is proportional to both F and L

E.2   FABRICATION

The cantilever beam was made from a $5\,1/2''$ length of hollow $3/4''$ square uncoated aluminium tubing (Fig. E.2). Square aluminum plugs $5/8''$ long with female threads along their central axes were inserted in each end to allow the sensor to be connected to the robot and the spring array. Each of these plugs was held in place with eight screws spaced along the perimeter of the aluminium tubing. Eight bonded-resistance strain gauges (SGD-7/350-LY13, Omega Engineering Inc., Stamford, CT) were affixed at the center of the beam in two full Wheatstone bridge configurations—one bridge for sensing force along each orthogonal axis.[1]
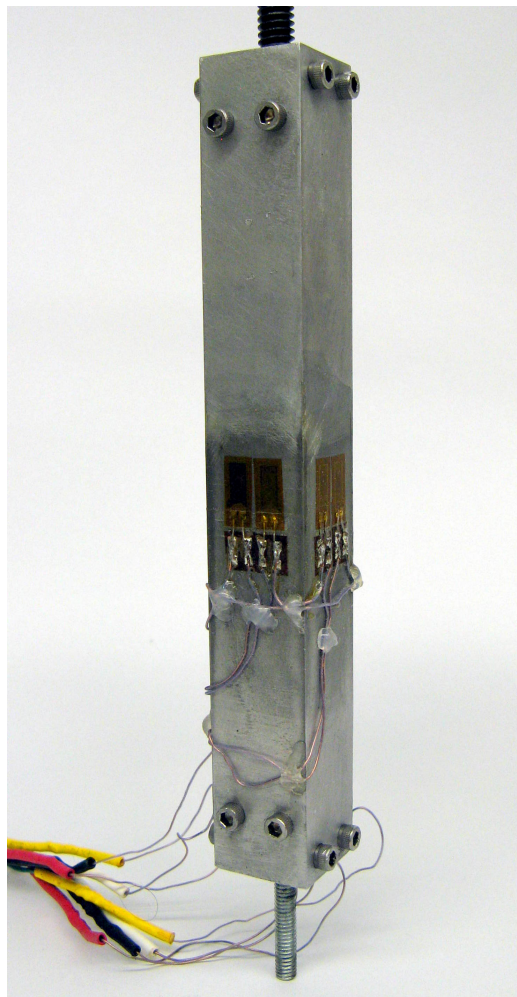
Figure E.2: Photograph of cantilever beam with strain gauge sensors.

---

[1] A video detailing the strain gauge mounting procedures is available at http://youtu.be/s4Bq8MvwbyU.

E.3   SIGNAL ACQUISITION

Fig. E.3 shows the block diagram of the sensor's signal acquisition system. A DC power supply equipped with an LM7805 voltage regulator chip provided the 5 V DC signal to power the two Wheatstone bridge circuits. The millivolt outputs from each of the bridges were transmitted through a shielded cable to commercial strain gauge preamplifiers (OM5-WBS-1-C, Omega Engineering Inc.) and amplified to a [0,5] V range. To enhance the sensor's resolution by exploiting the full [-10,10] V input range of the 12-bit analog-to-digital converters on the robot's data acquisition card, the preamplifier outputs were passed through a second amplifier and DC level shifter circuit. Finally, the amplified signals were low-pass filtered ($f_c = 48.2$ Hz) for anti-aliasing and noise suppression. The signals were then read by the robot's analog data acquisition card (Stroke Rehab USB, Quanser Inc.).
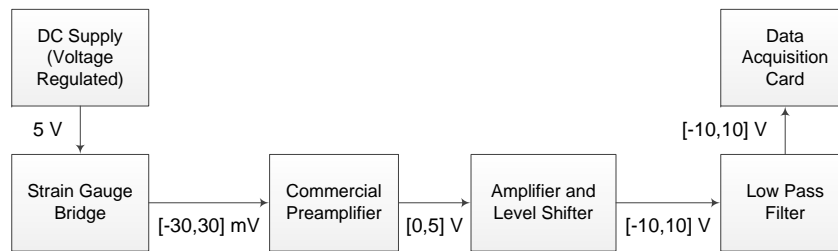
Figure E.3: Block diagram for each DOF of the strain gauge signal acquisition system.

Fig. E.4 shows the circuit topology for the amplifier, level shifter, and low-pass filter used to process signals from the sensor's *x*-axis. An op-amp summing amplifier is used to remove DC offset and amplify the input signal. Two Sallen-Key filters are cascaded to produce a 4th-order active low-pass filter. The op-amp supply voltages are provided by voltage regulator chips with passive *RC* filters ($f_c = 10$ Hz) for ripple suppression. The voltage regulators ensured that the circuit's gain did not vary with fluctuations in supply voltage.

E.4   CALIBRATION

The sensor was calibrated by affixing it to an immovable base and using masses to apply a known force to its free end. Calibration forces ranged from -50 N to 50 N, exceeding the typical range of forces encountered in impedance measurement experiments.
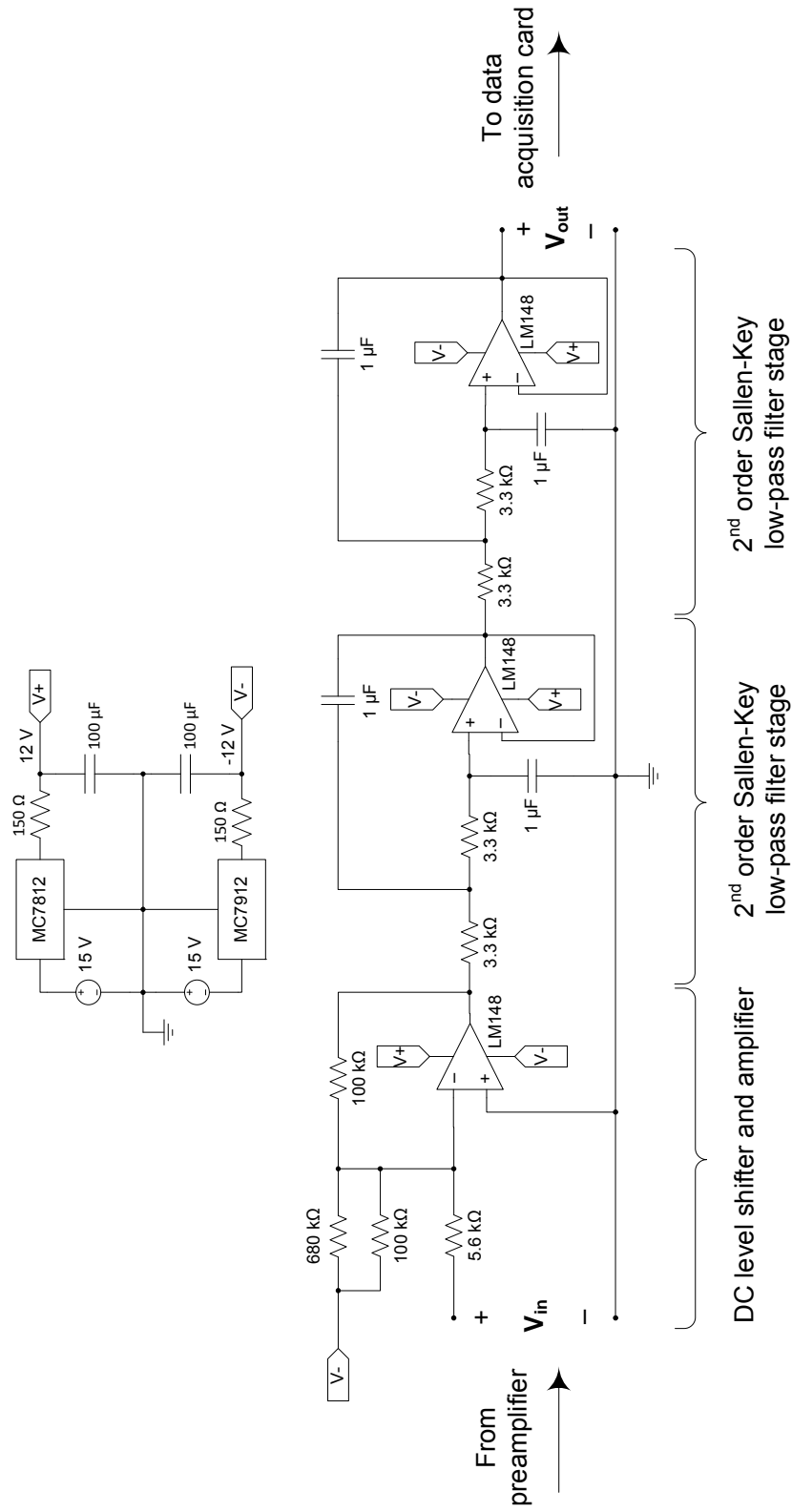
Figure E.4: Circuit diagrams of the amplifier, DC level shifter, and filter for the sensor's x-axis. The y-axis circuitry is identical except for the parallel 680 kΩ and 100 kΩ parallel resistor combination, which was tuned to zero the y-axis DC offset.

Fig. E.5 shows the force-voltage relation for the sensor's two axes. The equations of the best-fit lines with standard errors are

$$F_x = (-8.56 \pm 0.03)V_x + (0.54 \pm 0.06), \ R^2 = 0.9996, \qquad \text{(E.2)}$$
$$F_y = (-8.15 \pm 0.06)V_y + (2.3 \pm 0.1), \ R^2 = 0.9989.$$

The R^2 values near unity demonstrate that force-voltage relation is highly linear over its operating range. For each experiment, the slopes of these best-fit lines were used to convert voltage measurements to force. However, the y-intercepts of these lines were tuned on an experiment-by-experiment basis to account for changing force zero offsets that may be introduced by different hardware attached to the sensor.
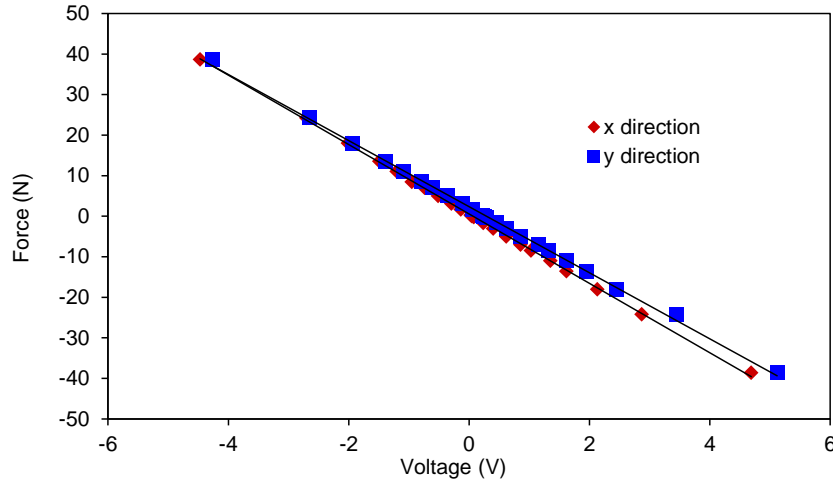
Figure E.5: Calibration of the strain gauge sensor.

Equation (E.1) shows that the sensor's output depends on the distance L between the strain gauges and the point of application of the applied force. During the calibration experiment, the spring array attachment disc (Fig. D.2) was connected to the sensor and the masses were suspended from this disc. This configuration had a lever arm of $L_0 = 6.88$ cm. If the force is applied at a different location, the force calculated by (E.2) must be scaled by the appropriate distance L:

The calibration equations must be scaled for different lever arms

$$F_{actual} = \frac{L_0}{L} F_{calculated} \qquad \text{(E.3)}$$

Each axis had a root mean square (RMS) noise of 0.01 N. Crosstalk between the sensor's two axes was sufficiently small to be neglected:

when the force on one axis was increased from 0 to 20 N, the force on the orthogonal axis changed by less than 0.5 N.

E.5 COORDINATE CONVERSION

The sensor measured forces in the (x_s, y_s) coordinate system shown in Fig. E.6. The following relation converted the measurements in the sensor coordinate frame to the Cartesian world coordinate frame originating at the robot's base:

$$\begin{bmatrix} F_x \\ F_y \end{bmatrix} = \begin{bmatrix} \sin(\theta_2) & \cos(\theta_2) \\ -\cos(\theta_2) & \sin(\theta_2) \end{bmatrix} \begin{bmatrix} F_{x_s} \\ F_{y_s} \end{bmatrix}. \tag{E.4}$$
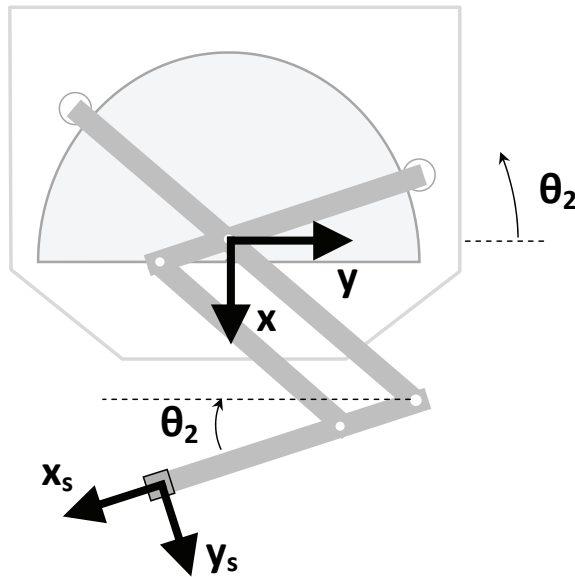
Figure E.6: Conversion of strain gauge sensor coordinates (x_s, y_s) to robot world coordinates (x, y).